ATOMISTIC APPROACHES FOR THE ANALYSIS, DESIGN, AND SIMULATION OF NANOSENSORS AND NANOCATALYSTS

A Dissertation

by

NARENDRA KUMAR

Submitted to the Office of Graduate and Professional Studies of
Texas A&M University
in partial fulfillment of the requirements for the degree of

DOCTOR OF PHILOSOPHY

Chair of Committee,	Jorge Seminario
Committee Members,	Perla Balbuena
	Yue Kuo
	Raymundo Arroyave
Head of Department,	Nazmul Karim

May 2016

Major Subject: Chemical Engineering

ABSTRACT

Using ideas of materials genome initiative, it is possible to create new materials with tailored properties for applications in nanoelectronics, sensing, and catalysis among other fields. The contamination of groundwater due to accidental leakage of radioactive wastes poses a grave danger to the environment and human life and hence trace characterization of these radioactive materials is of paramount importance in nuclear forensics and reprocessing. The presence of uranium and plutonium complexes in contaminated soil and water around nuclear processing facilities especially after a nuclear accident would provide us with critical information to guide a proper and timely response. We examine the applicability of graphene-based nanosensor for detection of these radionuclides based on *ab initio* density functional theory and Green's function theory. Changes in the molecular electrostatic potential due to presence of a foreign moiety near graphene can be transduced and amplified into current-voltage characteristics at nanoscale. By comparing the change in current due to presence of U or Pu complexes near a graphene-based sensor, we should be able to detect trace amounts of these radionuclides.

The DNA origami has emerged as a new and promising method to create nanostructures with precise atomistic tailored geometries. In addition, these origamis can be functionalized or impregnated with specialized single stranded DNA/RNA chains (known as aptamers) in order to convert them into biosensors. Thrombin is an enzyme directly involved in formation of blood clot which is a major cause of heart attack. We

perform molecular dynamics simulations to determine the relative energetics associated with the capture of thrombin by a novel biosensor assembly consisting of two aptamers attached to a rectangular DNA origami.

In addition to developing nanosensors, we also apply multi-scale computational approach to develop nanocatalysts and describe catalytic reactions happening at the surface to design more efficient catalysts. Molybdenum disulfide, (MoS_2) being a very versatile material for several applications, is an industrial catalyst for hydrotreating processes in petroleum refineries. We perform MD simulations on a typical middle distillate fraction of crude oil containing thiophene and dibenzothiophene molecules in order to determine their relative positions with respect to the catalytic surface previous to possible reactions that are then studied with DFT. Furthermore, we analyze MoS_2-graphene and MoS_2-boron nitride clusters as possible hydrodesulfurization catalysts.

ACKNOWLEDGEMENTS

I would like to thank my committee chair, Dr. Jorge M. Seminario, and my committee members, Dr. Perla Balbuena, Dr. Yue Kuo, and Dr. Raymundo Arroyave, for their guidance and support throughout the course of this research.

Thanks also go to my friends and colleagues and the department faculty and staff for making my time at Texas A&M University a great experience. I also want to extend my gratitude to the Texas A&M supercomputing center for providing me excellent facilities. Special thanks to Pink Floyd for creating heavenly songs and keep me motivated throughout my journey.

Finally, thanks to my mother and father for their encouragement and affection.

NOMENCLATURE

ABE	Anion binding exosite
AO	Atomic orbital
CPCM	Conductor-like polarizable continuum model
CUS	Coordinately unsaturated sites
DDS	Direct desulfurization
DFT	Density functional theory
DOS	Density of states
ECP	Effective core potential
G	Graphene
GO	Graphene oxide
HDS	Hydrodesulfurization
HOMO	Highest occupied molecular orbital
HYD	Hydrogenation
I-V	Current-voltage
LUMO	Lowest unoccupied molecular orbital
MD	Molecular dynamics
MEP	Molecular electrostatic potential
NBO	Natural bond order
NEGF	Non-equilibrium Greens function
NPA	Natural population analysis

RECP	Relativistic effective core potential
RGO	Reduced graphene oxide
RMSD	Root mean square displacement
SCF	Self-consistent cycle
ssDNA	Single-stranded deoxyribonucleic acid
TBA	Thrombin binding aptamer
ZPE	Zero-point error

TABLE OF CONTENTS

Page

LIST OF FIGURES

Page

LIST OF TABLES

Page

CHAPTER I

INTRODUCTION AND LITERATURE REVIEW

With current advancement in computational resources, both in hardware and software, it is possible to develop nanodevices and nanomaterials with desired characteristics and functions using computational tools. Density functional theory provides an efficient way to solve electronic structure problem of large clusters at reasonable computational cost while molecular dynamics are used to investigate dynamic properties of millions of atoms up to few nanoseconds. A combination of these powerful tools can enable us to develop nanosensors for various applications like detection of radioactive materials in nuclear wastewater, biosensing etc., as well as developing new catalysts for improving yield of desired products during a chemical reaction.

1.1 Graphene-based Nanosensor for Detection of Fissile Materials

Although there has been constant decline in number of nuclear power plants in operation worldwide in recent years, 11% of our electricity is still met through nuclear energy. In countries where petroleum and coal reserves are insufficient to meet the ever-growing demands of population, new nuclear power plants are being constructed or planned. The nuclear energy is advocated as economical and emission-free source of energy but the potential hazards and unforeseen disasters (recent accident in Fukushima, Japan) have always played on the minds of think tanks and researchers globally. As a

consequence, design and fabrication of electronic molecular devices as sensors for radionuclides using theoretical and experimental studies is of paramount importance in the nuclear community.

The presence of uranium and plutonium complexes in contaminated soil and water around nuclear processing facilities especially after a nuclear accident can provide us with critical information to guide a proper and timely response. Uranium and plutonium are known to be major constituents dissolved in nuclear waste water in the form of chlorides, nitrates, carbonates and sulfates.[1-3] Uranium in aqueous solution is predominantly present in the form of UO_2^{2+} complexes[1] while plutonium exhibits four different oxidation states, III, IV, V and VI; the last two as the dioxo-species PuO_2^{+} and PuO_2^{2+}.[4] DFT has been heavily used to study the structural properties of these complexes as can be seen from literature.[2,5-9] The ground state of the plutonyl ion (PuO_2^{2+}) has been determined as ^3H_g while that of uranyl (UO_2^{2+}) is found to be $^1\Sigma_g^+$.[10] The actinyls UO_2^{2+}, PuO_2^{2+} and NpO_2^{+} form pentagonal bipyramidal complexes with the surrounding water molecules[5], with five water molecules strongly bound in equatorial plane. A six-coordination complex is also reported to be equally favorable for UO_2^{2+} in aqueous solution based on solvation free energy.[7] When counter-ions (CO_3^{2-}, OH^- and NO_3^-) are present, one or two water molecules in the first shell are replaced by the counter-ions preserving five-fold symmetry. The structure and stability of nitrate and sulfate complexes of uranyl and plutonyl have been reported in literature.[2] In addition, electronic and spectroscopic properties for silicate, phosphate, and arsenate complexes

of uranyl complexes $H_2UO_2SiO_4(H_2O)_3$, $HUO_2PO_4(H_2O)_3$, and $HUO_2AsO_4(H_2O)_3$ and carbonate complexes for plutonyl of the types PuO_2CO_3 and the hydrated forms, $PuO_2CO_3(H_2O)_n$ (n = 1, 2) have been studied in great detail.[8,9] The maximal number of chloride ions in the first coordination sphere of Pu(III) and Pu(IV) ions was found to be eight using DFT calculations.[11]

There have been few studies also on aquo-chloro complexes of UO_2^{2+} and U^{4+} ions in aqueous solution both experimentally[12-13] and theoretically.[14] Using EXAFS spectroscopy, formation of $UO_2(H_2O)_5^{2+}$, $UO_2(H_2O)_4Cl^+$, $UO_2(H_2O)_3Cl_2$ and $UO_2(H_2O)Cl_3^-$ complexes were observed as concentration of chloride ions increases. For U(IV) ions, $U(H_2O)_9^{4+}$, $U(H_2O)_8Cl^{3+}$, $U(H_2O)_{6-7}Cl_2^{2+}$, and $U(H_2O)_5Cl_3^+$ complexes were found to occur.[13] The structure and energetics of aquo-chloro complexes of UO_2^{2+} were investigated using density functional theory and Car-Parinello MD.[14] Based on their calculations, they found that mono-chloride ($UO_2(H_2O)_4Cl^+$) is five-coordinated, while trichloride complex ($UO_2(H_2O)Cl_3^-$) is four-coordinated. The dichloride ($UO_2(H_2O)_nCl_2$) complex can exist both as four-coordinated or five-coordinated.

A lot of effort has been invested on studying the structure and dynamics of uranyl-nitrate complexes as they are the most probable species present in the extraction process of uranium in the PUREX process.[15-16] However, there is a lack of understanding in terms of relative stability of these species and their dissociation in aqueous phase. Using Car-Parinello molecular dynamics, Wipff et al.[15] showed that mononitrate-hydrate complex of uranyl binds in a bidentate mode in vacuum with three water molecules in the first shell thus having a coordination number of 5. In aqueous

phase, they showed that nitrate preferred to bind in monodentate fashion with four water molecules in the first shell thus preserving CN of 5. They also claimed that due to low complexation constant between uranyl and nitrates, mononitrate may be the most dominant conformer present in aqueous phase. Classical MD studies done on uranyl-nitrate association in aqueous solution also indicated that nitrates prefer to bind in monodentate fashion with a small quantity of bidentates.[16] However, their study indicates that uranyls are present predominantly in divalent ionic form hydrated by five water molecules. Classical MD simulations were also performed to study the structure of aquo, hydroxyl and carbonate complexes of UO_2^{2+} ion in bulk water and near hydrated quartz surface.[1] Their results indicate that uranyl ions exist in pentagonal bipyramidal symmetry with hydroxide and carbonates ions replacing water molecules in first shell. Carbonates were found to bind in bidentate fashion to the uranyl ion. It is worth mentioning that these classical force fields ignore strong polarization and charge transfer effects present in uranyl complexes. Pu(VI) being a triplet with an electronic configuration of $[Rn]5f^2 7s^0$ has more diffuse f-orbitals available for binding with ligands unlike U(VI) which is a singlet with a noble gas electronic configuration.

The aquo and nitrate complexes of Pu^{4+} in addition to the aquo-chloro complexes of PuO_2^{2+} have been reported using DFT and scalar relativistic effective core potentials (RECP) in vacuum as well as with polarizable continuum solvation model.[17] Apart from actinyl complexes, the solvation of Pu^{3+} ion in water was investigated using relativistic DFT to determine binding energies and optimized geometries for different coordination numbers of water molecules.[3] Based on the binding energy of $Pu(H_2O)_n^{3+}$ clusters

(n=6,8,9,10,12), $Pu(H_2O)_9^{3+}$ had the largest binding energy. Based on total energy, $Pu(H_2O)_8 \cdot (H_2O)^{3+}$ was found to be more stable than $Pu(H_2O)_9^{3+}$ the difference in energy being 0.34 eV.[3] The actinides (U^{3+}, Pu^{3+} and Pu^{4+}) show a higher coordination number of 9–10 with water molecules.[18-19] A significant amount of research has been dedicated to study the hydration of Th(IV) ion. The first coordination sphere of the Th(IV) ion calculated using B3LYP hybrid functional and relativistic large core effective core potential shows a coordination number of 9 in vacuum.[20] The aqueous phase binding energy was calculated at the optimized geometry in vacuum by adding solvent effects using polarized continuum model. The optimized structure along with ESP charges were then used to obtain second shell of water molecules using hydrated ion concept. In a follow up paper, solvation effects was included in geometry optimization and the coordination number calculated using B3LYP and large core ECP was reported to be 9–10.[21] The bond lengths were similar to the corresponding experimental values for $Th(H_2O)_9^{4+}$ complex. Ab-initio calculations on Th/water complex were also reported using relativistic Douglas-Kroll-Hess Hamiltonian and ANO-RCC basis-set. Based on calculated binding energy, their results indicate that $Th(H_2O)_8.(H_2O)_2^{4+}$ is most stable while $Th(H_2O)_{10}^{4+}$ is least stable in vacuum.[22] The hydration structure of $ThCl_4$ and $ThBr_4$ in aqueous solution have also been reported using Car-Parinello molecular dynamics as well as classical molecular dynamics using polarizable force field.[23] However, unlike Th(IV) ion, there is a dearth of literature on similar hydration structures for the Pu(IV) ion due to its greater complexity for theoretical treatment as an open-shell ground state.

In a very promising work, Romanchuk et al.[24] showed experimentally that graphene oxide (GO) has a higher sorption capacity for U(VI) and Pu(IV) ions from waste solutions in the presence of common ions such as Na^{+}, Ca^{2+}, NO_3^{-}, Cl^{-}, carbonates, and sulfates over a wide range of pH. Therefore graphene oxide (GO) is expected to be more effective in removal of radionuclides compared to traditional bentonite clays and activated carbon.[25] However, there are only few studies done to study interaction of these complexes with GO. GO is known to contain a variety of oxygen-containing functional groups on its edge and on its basal plane. Though the molecular formula can exhibit several variations, common functional groups present are epoxy, carbonyl, hydroxyl and carboxylic groups.[26-27] The binding of hydrated uranyl cation with oxygen containing functional groups of GO was investigated by Wu et al.[28]. They also studied in a recent paper interaction of plutonium and neptunium with GO,[29] but they did not consider the effect of counter-ions present in the system. Their study however show that PuO_2^{2+} and NpO_2^{2+} in cation form can covalently bond to oxygen containing functional groups. Sun et al. synthesized GO-supported polyaniline composites for sorption of U(VI), Eu(III), Sr(II) and Cs(I) from aqueous solution.[30] In acidic conditions, polyaniline-GO composite has a higher affinity for heavy metal ions due to presence of large number of amine and imine functional groups. However, nitrogen-containing functional groups have a stronger chemical affinity than oxygen-containing functional groups towards radionuclides. Radionuclides can be extracted from oxygen-containing functional groups more easily than nitrogen-containing functional groups due to irreversible adsorption.[30] This is however in contrast to the works done by Wu et al.

where they showed than uranyl has a stronger binding with the graphene modified by hydroxyl and carboxyl groups than by graphene functionalized by -$CONH_2$ and -$CONMe_2$ groups.[28] It should also be noted that the sorption experiments were shown to depend on pH of the solution. More work needs to be done to clarify the binding nature of these radionuclides with GO.

In order to design a fissile nanosensor, the first step is to identify the major radionuclides and their form present in soils and groundwater around contaminated sites and production facilities and obtain their optimized structure. Once we identify the common complexes present in nuclear waste water, we can obtain their optimized structure using a density functional and an appropriate basis-set. Due to their interesting electronic properties[31-32], graphene has found huge interest in the academic community in several applications. Functionalized form of graphene can be utilized as FRET biosensors[33], transparent conductive films[31], environmental pollution management[34], nuclear waste disposal[24], tunable optical devices[35], molecular devices[36] among several other applications. However, covalent functionalization can also lead to loss of those properties which make graphene so fascinating. The plasmons (sea of π-electrons on the graphene surface) of graphene nanosheets are highly sensitive and likely to be affected by the electrostatic field of a single foreign molecule which is reflected in their electrical and optical responses.

Our nanosensor consists of a pristine graphene molecule or a form of GO molecule with a carbonyl group in some cases, with two gold contacts attached to its two ends. The two contacts are further connected to an external voltage source and the

current flowing through the circuit is measured. If any foreign moiety (uranium and plutonium complexes) approaches the sensing molecule, it causes a strong change in the molecular electrostatic potential of the graphene sensor. The change in electrostatic potential can be amplified into a current-voltage characteristic, which is the working principle behind graphene-based nanosensors.[37-38]

The theoretical current-voltage characteristics are obtained using a combined DFT-Green's function approach[39] developed originally to analyze current-voltage characteristics in single molecule experiments[40-41].

1.2 DNA Origami-based Biosensor for Detection of Enzymes and Proteins

The DNA origami has emerged as a new and promising method to self-assemble DNA into desired two- and three-dimensional shapes. The programmed folding of long DNA strands into custom shapes has great potential in nanotechnology applications such as nanobiosensors. The field of DNA nanoconstructs by bending long DNA strands was first conceived by Ned Seeman at NYU some three decades ago. However, programmed folding of DNA strands (hereafter referred as DNA origami) was first reported by Paul Rothemund in 2006 only. The DNA origami can act as a vehicle for docking of protein- or enzyme-specific aptamers, which are single stranded DNA chains with binding sites for specific proteins; and therefore, this origami structure can be used as a biosensor.

Our biosensor essentially consists of a DNA origami as substrate to which sensing molecules or probes are tethered at appropriate locations. The probes in our study are single stranded nucleic acid chains known as aptamers which are known to

have higher specificity and affinity towards molecular targets like protein, enzymes and other small organic molecules. The detection of these targets is usually based on Fluorescence Resonance Energy Transfer (FRET) where few nucleotides of the aptamer (probes) are modified by using a fluorophore. The energy transfer is distance-dependent and shows detectable changes in presence of the target molecules. The electrochemical response of the biosensor can also be adopted as a mode of sensing. The temperature-dependent current–voltage characteristic of a DNA origami solution trapped between electrodes has been already reported in literature using a four-probe station.[42-43] The authors observed high impedance below 240 K and an exponential behavior with respect to the inverse of temperature at near room temperature.

Our work focuses mainly on detection of thrombin, a proteinase (enzyme) involved in blood coagulation. The presence of thrombin indicates the existence of blood clot. Our simulations not only shows a remarkable selectivity of the nanobiosensor assembly for thrombin, but also can be extended to detect biotoxins such as ricin by simply choosing proper aptamers.

1.3 Computational Design of HDS Catalysts

Catalyst design from first principles is a challenge that is becoming reality with current advances in computational software and hardware. Over the last decade, significant effort has been made to elucidate the reaction mechanisms and to identify reaction intermediates using both periodic and finite cluster approaches via density functional theory. The hydrodesulphurization (HDS) is one the most important processes

in a refinery to remove sulfur containing compounds from petroleum fractions. Stricter legislations now require removing even the most refractory sulfur compounds such as alkyl dibenzothiophenes. Although hydrodesulfurization processes have been investigated for several decades, considerable research is underway to understand these catalytic mechanisms and to develop new chemistries that may be able to improve efficiency and reduce costs needed for more efficient processes and more active catalysts.

In this work we focus on the removal of thiophene and dibezothiophene (DBT) over both, unpromoted and Ni-promoted MoS_2 catalyst using a finite cluster approach. Efforts have been made to analyze HDS reactions over both pristine MoS_2 as well as under industrial conditions.

CHAPTER II

A BRIEF OVERVIEW OF DENSITY FUNCTIONAL THEORY AND THEORY OF ELECTRON TRANSPORT*

For a molecular system of N-electrons and M-nuclei, the time-independent Schrödinger equation for a non-relativistic system is

$$\hat{\mathrm{H}}(\{R_i\};\{r_i\})\Psi(\{r_i\}) = E(\{R_i\})\Psi(\{r_i\}) \tag{2.1}$$

where $\hat{\mathrm{H}}$ is the total energy operator defined as

$$\hat{\mathrm{H}} = -\sum_{i=1}^{N}\frac{\hbar^2}{2m}\nabla_i^2 - \sum_{A=1}^{M}\frac{\hbar^2}{2m}\nabla_A^2 - \sum_{i=1}^{N}\sum_{A=1}^{M}\frac{Z_A e^2}{r_{iA}} + \sum_{A=1}^{M}\sum_{B>A}^{M}\frac{Z_A Z_B e^2}{R_{AB}} + \sum_{i=1}^{N}\sum_{j>i}^{N}\frac{e^2}{r_{ij}} \tag{2.2}$$

and $\Psi(\{r_i\}) = \Psi(\overrightarrow{r_1}, \overrightarrow{r_2}, \overrightarrow{r_3} \ldots\ldots, \overrightarrow{r_N})$ is in 3N-dimensional space assuming spin is implicitly included. The above equation can be solved analytically for hydrogen-like atoms or ions having single electron and the solution is found to be of the form

$$\Psi_{nlm}(\vec{r}) = \Psi_{nlm}(r,\theta,\varphi) = R_{nl}(r)Y_l^m(\theta,\varphi) \tag{2.3}$$

For a system of two or more electrons, no analytical solution can be obtained in closed form as in the case of hydrogen. Using the Born-Oppenheimer approximation of decoupling the electronic and nuclear motion due to huge mass of nuclei compared to that of electron, one can partition the wavefunction into electronic and nuclear components.

* Reproduced in part with permission from N. Kumar and J.M. Seminario, Design and Applications of Nanomaterials for Sensors, Springer Netherlands. Copyright 2014 Springer

$$\hat{\mathrm{H}} = \hat{\mathrm{H}}_{elec} + \hat{\mathrm{H}}_{nuc} \tag{2.4}$$

where

$$\hat{\mathrm{H}}_{elec} = -\sum_{i=1}^{N} \frac{\hbar^2}{2m} \nabla_i^2 - \sum_{i=1}^{N} \sum_{A=1}^{M} \frac{Z_A e^2}{r_{iA}} + \sum_{i=1}^{N} \sum_{j>i}^{N} \frac{e^2}{r_{ij}} \tag{2.5}$$

or,

$$\hat{\mathrm{H}} = \hat{T} + \hat{V}_{ext} + \hat{V}_{ee} \tag{2.4}$$

where

$$\hat{T} = -\sum_{i=1}^{N} \frac{\hbar^2}{2m} \nabla_i^2 \text{ =kinetic energy of electrons}$$

$$\hat{V}_{ext} = -\sum_{i=1}^{N} \sum_{A=1}^{M} \frac{Z_A e^2}{r_{iA}} \text{= nuclei-electron interaction energy}$$

$$\hat{V}_{ee} = \sum_{i=1}^{N} \sum_{j>i}^{N} \frac{e^2}{r_{ij}} \text{=electron-electron interaction energy}$$

Variational principle: According to this principle, any trial wavefunction for the ground state always yields an upper bound to the exact energy *E*,

$$E \leq \left\langle \Psi^t \middle| \hat{\mathrm{H}} \middle| \Psi^t \right\rangle \tag{2.5}$$

and

$$\Psi^t = \sum_i C_i u_i \tag{2.6}$$

This allows us to choose a basis-set of functions $\{u_i\}$ such that a linear combination of them will tend to exact energy. Thus the problem reduces to finding the coefficients of linear combination which minimizes equation (2.5).

2.1 Standard ab-initio Methods

Mean field approximation: Wavefunction is a product of single-electron wavefuntions and there is no correlation between motions of two electrons. In other words, each single electron sees a smeared out cloud of other electrons and moves in an average potential due to other electrons present.

$$\Psi(\{r_i\}) = \phi_1(\vec{r_1})\phi_2(\vec{r_2})\phi_3(\vec{r_3}) \dots \dots \phi_N(\vec{r_N}) \tag{2.7}$$

This reduces the 3N-dimensional problem to N 3-dimensional problem. For each electron, we can then write[44],

$$\left[-\frac{\hbar^2}{2m}\nabla^2 - \sum_{A=1}^{M}\frac{Z_A e^2}{r_{iA}} + \sum_{i\neq j}^{N} e^2 \int \frac{\left|\phi_j(r_j)\right|^2}{r_{ij}} d^3 r_j\right]\phi_i(\vec{r_i}) = E'\phi_i(\vec{r_i}) \tag{2.8}$$

The above set of equations is called Hartree equation. However, as per Pauli's exclusion principle that an orbital can have only two electrons of opposite spin and electrons are indistinguishable. This principle puts a restriction on the wavefunction that it has to be anti-symmetric with respect to the exchange of electrons and therefore, it has to be in the form of a Slater determinant,

$$\Psi(\vec{r_1}, \vec{r_2}, \vec{r_3} \dots \dots, \vec{r_N}) = \frac{1}{\sqrt{N!}}\begin{bmatrix} \phi_1\left(\vec{r_1}\right) & \cdots & \phi_N\left(\vec{r_1}\right) \\ \vdots & \ddots & \vdots \\ \phi_1\left(\vec{r_N}\right) & \cdots & \phi_N\left(\vec{r_N}\right) \end{bmatrix} \tag{2.9}$$

Substituting the above wavefunction in Equation 2.5, results in the Hartree-Fock equations[44]

$$\left[-\frac{\hbar^2}{2m}\nabla^2 - \sum_{A=1}^{M}\frac{Z_A e^2}{r_{iA}}\right]\phi_i(\vec{r_i}) + \sum_{j=1}^{N} e^2 \int \frac{\left|\phi_j(r_j)\right|^2 \phi_i(r_i)}{r_{ij}} d^3 r_j + \sum_{j=1}^{N} e^2 \int \frac{\phi_j^*(r_j)\phi_i(r_j)\phi_j(r_i)}{r_{ij}} d^3 r_j = E'\phi_i(\vec{r_i}) \tag{2.10}$$

The second integral is the exchange energy which arises due to in distinguishability of electrons. Both Hartree and Hartree-Fock equations are iterative in nature. To solve the wavefunction for one electron, we need wavefunction of other electrons in the system i.e. they are self-consistent in nature and the procedure is called SCF.

2.2 Density Functional Theory

Density functional theory (DFT) solves the Schrödinger equation through an exact procedure that bypasses the calculation of the wavefunction[45]. DFT method uses the electron density instead of wavefunction to obtain the energy eigenvalues and is based on the Hohenberg-Kohn theorems (1964).

Theorem 1: Ground state wavefunction $\Psi_o(\overrightarrow{r_1}, \overrightarrow{r_2}, \overrightarrow{r_3} \dots \dots, \overrightarrow{r_N})$ is a functional of ground state electron density $\rho_o(\vec{r})$ where

$$\rho_o(\vec{r}) = N \int d^3\overrightarrow{r_2}\, d^3\overrightarrow{r_3} \dots d^3\overrightarrow{r_N} \left|\Psi_o(\overrightarrow{r_1}, \overrightarrow{r_2}, \overrightarrow{r_3} \dots \dots, \overrightarrow{r_N})\right|^2 \tag{2.11}$$

In matrix form, $\rho_o(\vec{r}) = N\langle\Psi|\delta(\vec{r} - \overrightarrow{r_i})|\Psi\rangle$

Theorem 2: Ground state energy is also a functional of electron density,

$$E = E_v[\rho] \tag{2.12}$$

Using variational principle, we can then write $E_v[\rho^t] \geq E$

The electronic part of Schrodinger equation for ground state can then be written as

$$E[\rho] = \hat{T}[\rho] + \hat{V}_{ext}[\rho] + \hat{V}_{ee}[\rho] \tag{2.13}$$

The classical electron-electron repulsion ($\hat{V}_H$) can be extracted out of $\hat{V}_{ee}[\rho]$ and the remainder is called exchange-correlation energy (E_{XC}).

$$\hat{V}_{ee}[\rho] = \hat{V}_H[\rho] + V_{XC}[\rho] \tag{2.14}$$

This results in the Kohn-Sham equations (1965) as shown[44],

$$\left[-\frac{\hbar^2}{2m}\nabla^2 + V_{ext}(r) + V_H(r) + V_{XC}(r)\right]\phi_i(\vec{r}) = \varepsilon_i\phi_i(\vec{r}) \tag{2.15}$$

with $\rho_o(\vec{r}) = N\sum_{i=1}^{N}|\phi_i|^2$.

The idea is to use a set of molecular orbitals with a sole purpose of representing the electron density of non-interacting electrons that have the same density as the real system.

2.3 Basis-sets

A basis-set is a set of vectors (generally non-orthogonal one-particle functions) which span a space used to build molecular orbitals (MO). These MOs are a linear combination of atomic orbitals (LCAO); thus the MOs are also one-particle functions. From Schrodinger equation,

$$\hat{\mathrm{H}}\Phi = E\Phi$$

and $\Phi = \sum_m \phi_m u_m$ where ϕ_m are the coefficients and $\{u_m\}$ are the basis functions. Substituting in above equation yields:

$$\hat{\mathrm{H}} \sum_m \phi_m u_m = E \sum_m \phi_m u_m \tag{2.16}$$

Multiplying by u_n^* on both sides and integrating over $\vec{r}$ gives:

$$\sum_m H_{nm}\, \phi_m = E \sum_m S_{nm}\, \phi_m \tag{2.17}$$

$$H_{nm} = \int d\vec{r} u_n^*(\vec{r}) \hat{\mathrm{H}} u_m(\vec{r})\,;\; S_{nm} = \int d\vec{r} u_n^*(\vec{r}) u_m(\vec{r}) \tag{2.18}$$

In matrix form, this can be written as:

$$[H]\{\Phi\} = E[S]\{\Phi\} \tag{2.19}$$

[H] is the Hamiltonian matrix and [S] is the overlap matrix. If the basis-functions $\{u_m\}$ are orthonormal, then [S] becomes an identity matrix.

There are different types of basis-sets available. The smallest basis-set is called minimal basis set where each AO is represented by only one basis function called Slater type orbital (STO).

$$\phi_{abc}^{STO}(x, y, z) = N x^a y^b z^c e^{-\zeta r} \tag{2.20}$$

Atomic orbitals (AOs) in most quantum mechanics programs are represented by atom-centered Gaussians or Gaussian type orbitals (GTOs) because the simplicity to solve the four-center integrals compared to the direct use of hydrogenic functions or even Slater type orbitals.

$$\phi_{abc}^{GTO}(x,y,z) = Nx^a y^b z^c e^{-\zeta r^2} \tag{2.21}$$

For example, one STO is constructed with three Gaussian functions, also called primitives, in the STO-3G basis set. Well, the nomenclature relates to the fit the three Gaussians to get the Slater orbital. Then we have double-zeta and triple-zeta basis sets where each valence AO is represented by two and three basis-functions respectively and the core electrons mostly by just one. Typical of this type are the common split-valence basis sets. A double split-valence basis set (also named double-ζ) is represented as *c*-*mn*G (also referred to as Pople basis-sets[46]) where *c* is the number of primitive (Gaussian) functions to represent the core orbitals and the valence orbitals are split in two groups: one with *m* primitives representing the inner valence and another with *n* Gaussians for the outer valence orbitals (for example, the 6-31G). These rules were followed at the earlier days of quantum chemistry but several deviations were made in order to provide the best basis sets, especially when second row or higher atoms are involved. For instance, the triple-ζ basis set 6-311G for silicon does not follow exactly such distribution of Gaussian primitives. Often polarization functions (denoted by *) and diffuse functions (denoted by +) are added to these basis-sets to make them more flexible and therefore to obtain more accurate results.

2.4 Electron Transport Using Greens Function

To account for semi-infinite metallic contacts attached to the molecule, Schrödinger equation is modified as

$$E[I]\Psi = [H]\Psi + [\Sigma]\Psi + \{s\} \tag{2.22}$$

where $[\Sigma]$ and $\{s\}$ represent outflow and inflow of electrons from contacts respectively.[47-48] .The wavefunction Ψ for the modified Schrödinger equation can be written as

$$\Psi = G^R\{s\} \tag{2.23}$$

where G^R is called the retarded Greens function for the molecule including the effect of contacts and is defined as

$$G^R = [EI - \Sigma - H]^{-1} \tag{2.24}$$

In this approach, sometimes called non-equilibrium Green function[47-48], the Green function G for the whole system in matrix form has infinite dimensions but can be partitioned into a set of finite matrices[49],

$$G(E) = \begin{bmatrix} g_1^{-1} & -\tau_1 & 0 \\ -\tau_1^\dagger & E1 - H_C & -\tau_2^\dagger \\ 0 & -\tau_2 & g_2^{-1} \end{bmatrix}^{-1} = \begin{bmatrix} G_1 & G_{1M} & G_{12} \\ G_{M1} & G_M & G_{M2} \\ G_{21} & G_{2M} & G_2 \end{bmatrix} \tag{2.25}$$

The submatrices G and g in above matrix represent Green functions when interactions among subsystems are included or excluded, respectively. H_C is the Hamiltonian of the isolated molecule and E is the electron energy. G_M is the retarded Green function G^R in above equation. The self-energy term Σ accounting for the interaction between the molecule and the contacts are calculated as

$$\Sigma = \Sigma_1 + \Sigma_2 \tag{2.26}$$

where $\Sigma_i = \tau_i^\dagger g_i \tau_i$.

The Hamiltonian matrix H_C is obtained using DFT calculations where few metallic atoms are added to each end of the molecule of interest. This helps us to

describe molecular electronic structure as well as the coupling between the molecule and the contacts more accurately. From the matrix form of the Schrodinger Equation,

$$[H_{KS}]\Psi = \varepsilon[S]\Psi$$

and making

$$[H] \rightarrow [S]^{-1}[H_{KS}]$$

The calculated Kohn-Sham Hamiltonian in the atomic basis set can be partitioned in submatrices, where the subscripts 1 and *2* refer to the contacts and *M* to the molecule[49].

$$[H_{KS}] = \begin{bmatrix} H_{11} & H_{1M} & H_{12} \\ H_{M1} & H_{MM} & H_{M2} \\ H_{21} & H_{2M} & H_{22} \end{bmatrix} \tag{2.27}$$

The overlap matrix [*S*] can be also partitioned in similar fashion. The Hamiltonian and the overlap matrices for the extended molecule are recalculated at each bias field in order to account for the reorganization of the molecular electronic structure due to the external field as well as charge transfer between molecule and contacts. H_{MM} is assigned to H_C and H_{iM} and H_{Mi} are assigned to τ_i and $\tau_i^{\dagger}$ respectively. This simplifies the expressions for calculating self-energy terms as

$$\Sigma_i = H_{Mi} g_i H_{iM} \tag{2.28}$$

The Green function for nano-contacts (clusters of *n* Au atoms), g_i, can be approximated as a diagonal matrix *n*×*n* with each element being a diagonal matrix proportional to their local, *s*, *p*, and d_{t2e} and d_{eg} density of states over all atoms representing the nano-contacts.

$$g_i(E) = \begin{bmatrix} g_i^1 & \cdots & 0 \\ \vdots & \ddots & \vdots \\ 0 & \cdots & g_i^n \end{bmatrix} \tag{2.29}$$

The DOS and its *s*, *p* and *d* contributions for the gold clusters are obtained from the electronic structure of optimized geometry and its converged electronic structure. Thus, the Green function for each atom of the metallic contact is given by[49]

$$g_i^k(E) = \begin{bmatrix} D_i s^k(E) & 0 & 0 & 0 \\ 0 & D_i p^k(E) & 0 & 0 \\ 0 & 0 & D_i d^k_{t_{2g}}(E) & 0 \\ 0 & 0 & 0 & D_i d^k_{e_g}(E) \end{bmatrix} \tag{2.30}$$

The rate at which electrons are released from the contacts is given by Γ where Σ is the self-energy matrix and $\Sigma^\dagger$ is its adjoint.

$$\Gamma = i[\Sigma - \Sigma^\dagger] \tag{2.31}$$

where

$$G^A = [G^R]^\dagger \tag{2.32}$$

The current flowing through the molecule depends on number of electrons flowing through the channel given by[47]

$$N = Trace(\{\Psi\}\{\Psi\}^\dagger) = \frac{Trace[G^n]}{2\pi} \tag{2.33}$$

where

$$G^n = G^R \Sigma^{in} G^A \tag{2.34}$$

and

$$\Sigma^{in} = \Gamma_1 f_1 + \Gamma_2 f_2 \tag{2.35}$$

The spectral function *A* of the system contact-molecule-contact is given by

$$A = G^R \Gamma G^A \tag{2.36}$$

The trace of matrix *A* gives the density of state (DOS). The current through a terminal '*p*' is given by

$$I_p = \frac{q}{h} Trace\left[\Gamma_p A f_p - \Gamma_p G^n\right] \tag{2.37}$$

This further can be modified for current from contact 1 to

$$I_1(E) = \frac{q}{h} Trace[\Gamma_1 G^R \Gamma_2 G^A]\big(f_1(E) - f_2(E)\big) \tag{2.38}$$

The terms $f_1(E)$ and $f_2(E)$ are the Fermi functions for the two contacts. Hence, conductance of the junction can be calculated as

$$G(E) = \frac{q^2}{h} T(E) \tag{2.39}$$

where $T(E) = Trace[\Gamma_1 G^R \Gamma_2 G^A]$ is called the Transmission function. The total current is obtained by integrating equation (2.38) over energy states,

$$I(V) = \frac{2e}{h} \int_{-\infty}^{+\infty} dE\, T(E,V)\,[f_1(E,V_1) - f_2(E,V_2)] \tag{2.40}$$

The applied voltage shifts the Fermi level in the metal contacts by E_{f1} and E_{f2} up and down and the chemical potential of the molecule (μ)shifts in between which defines the limits for electron transport[49-50].

$$E_{f1} = \mu - \frac{1}{2} eV \tag{2.41a}$$

and

$$E_{f2} = \mu + \frac{1}{2}eV \tag{2.41b}$$

CHAPTER III

SPECIATION OF ACTINIDE SALTS IN NUCLEAR WASTE WATER*

We use density functional theory calculations to study how actinides are dressed in nuclear waste water in order to determine the equilibrium structure of common uranium, plutonium and thorium salts. We report all structures and energetics of these complexes both in vacuum as well as in solution. This information is essential to design an effective fissile nanosensor for detecting these radionuclide complexes. Both UO_2^{2+} and PuO_2^{2+} ions show coordination number of 4-5 with counterions (e.g. chlorides, nitrates) replacing one or two water molecules from coordination shell. On the other hand, Pu(IV) forms a 8-coordinated first shell when completely solvated as well as in the presence of counterions with counterions replacing water molecules in the first shell.

3.1 Introduction

The ageing nuclear reactors, accidental leakage of nuclear waste and unseen nuclear disasters are always a threat to our safety and our environment. One of the first measures to avoid a colossal loss due to these unwelcome events is to develop very efficient and sensitive nuclear sensor devices in order to catch in the very early stages any potential threat. In this regard, several efforts have been in progress to develop the basic science of nanosensors, which eventually will be able to detect atomistic quantities

* Reproduced in part with permission from N. Kumar and J.M. Seminario, J. Phys. Chem. A, Vol 9, Issue 4, Pages 689-703. Copyright 2014 American Chemical Society

of fissile materials[24,37,51-53] based on the extraordinary properties of new materials such as graphene compounds.[54-55]

The first and foremost information needed to design a nanosensor for detection of radionuclides in nuclear waste water is to know in what form actinides atoms are present when solvated in water. Density functional theory calculations can be used to identify the complexes actinides form with common ions present in contaminated soil and water near production facilities. Actinides tend to form strong complexes with anions like chlorides, nitrates, carbonates and sulfates. Ab-initio DFT calculations using relativistic effective core potentials are convenient and widely used tools to study these complexes; a summary of which has been presented in detail in Chapter I. The uranyl (UO_2^{2+}) and plutonyl (PuO_2^{2+}) ions form pentagonal bipyramidal geometries with five water molecules in the equatorial plane when completely solvated in water. When complexed with counter-ions such as CO_3^{2-}, OH^- and NO_3^-, the five-fold symmetry is retained with counter-ions replacing one or two water molecules in the first coordination shell. Moreover, PuO_2^{2+} forms stronger complexes with these anions compared to the UO_2^{2+} cation.[2] Their affinity also varies with type of counter-ions considering the fact that sulfate ions bound more strongly than nitrate ions.[2] A lot of work has been done in speciation of radionuclide complexes in water using both static ab-initio as well as Car-Parrinello methods. Most of these works make use of effective core potentials. Car-Parrinello molecular dynamics (CPMD) calculations performed on uranyl nitrate complex showed that mononitrate-hydrate complex may be the most predominant species present in aqueous phase.[56] Similarly, CPMD calculations for uranyl chloride

complexes showed that monochloride-hydrates may be the most probable species present.[57] Classical molecular dynamics using polarizable force field as well as CPMD calculations done for Th(IV) chlorides and bromides indicate that Th(IV) is more likely to occur as completely hydrated structure in water.[58] Unlike Th(IV) ion, Pu(IV) ion has much higher affinity to attract counter-ions due to open-shell ground state [37].

In this chapter, we calculate relative stabilities of several salts of UO_2^{2+}, PuO_2^{2+}, Th(IV) and Pu(IV) ions and their speciation both in vacuum and in aqueous phase represented by a conductor-like polarizable continuum model using ab-initio density functional theory. The coordination numbers and optimized structures of these complexes are critical information for electrochemical response experiments because the actinides are more likely to be present in complex forms rather than the bare ions in aqueous solution. Their relative stabilities will then determine their likelihood of detection. The stable structures thus obtained will be subsequently used in later chapters to examine the applicability of graphene-based nanosensor for detection of these species based on changes in electrical conductance as outlined in previous chapter. An understanding of solvation chemistry of these ions is thus essential to make headway progress in development of nanosensors for detection of these species.

3.2 Methodology

All density functional theory[59-60] calculations are performed with the hybrid functional B3PW91 which uses Becke exchange[61] with some component of Hartree-Fock[62-64] and the correlation functional of Perdew-Wang.[65-69] B3PW91 functional has

been used successfully in a variety of applications involving nanomaterials,[70-76] nanobiomaterials,[77-78] as well as nanosensors,[36,79-81] and energetic materials,[82-85] among others. Stuttgart effective core potential and associated basis set (ECP60MWB_SEG) are used for plutonium and uranium[86-87], with ECP parameters based on a quasi-relativistic level of theory.[86-87] For other atoms present in the system, the 6–31G(d) basis set[88] is used unless mentioned otherwise. The ECP parameters for U and Pu have been derived from atomic wavefunctions obtained using a quasi-relativistic level of theory.[87,89] All of the DFT calculations are performed using GAUSSIAN-09[90] program with convergence threshold for self-consistent cycle (SCF) set as 10^{-6} for density matrix and 10^{-8} for root-mean- square and maximum density matrix error respectively. Geometry optimizations are carried out with the Berny method[91-92] and the structures are checked to be local minima by running frequency calculations. The zero-point vibrational corrections are obtained for all optimized structures from the frequency calculations. In addition we also calculate dispersion corrections using the D3 version of Grimme's empirical dispersion[93]. The uncorrected binding energy (ΔE_u) is calculated as the difference in total energy of complex and total energy sum of its constituent molecules without any correction. The binding energy of each complex is then corrected by adding the zero-point energy correction (ΔZPE) and dispersion corrections (ΔD) to the uncorrected binding energy. In order to study bulk solvent effects, we also performed geometry optimizations as well as frequency calculations in solution using the Gaussian 09 implementation of the conductor like polarizable continuum model (CPCM)[94-95]. The CPCM model assumes spheres with scaled UFF radii centered on the atoms and places

the solute inside the cavity formed by overlap of those spheres. By default, the GAUSSIAN-09 program assumes the molecular surface representing the solute-solvent boundary as van der Waals surface. The dielectric constant inside the cavity is same as that of vacuum while outside the cavity, the dielectric constant of the solvent is used.

3.3 Quantum Chemistry Results

In order to have some level of confidence in chosen level of theory, atomic ionization potentials are calculated for which precise experimental information are available. The ionization potentials provide a rigorous validation test as both open and closed shell calculations are required. The first and second ionization potentials of thorium, uranium and plutonium were calculated at HF, MP2, CCSD(T) and B3PW91 procedures using several basis-sets as listed in Tables 3.1–3.3. The frozen core option resulted in excessive mixing of frozen core and valence orbitals in case of ANO-RCC basis-set[96-97] for MP2 and CCSD(T) calculations due to some valence MOs having considerable contribution from the core AOs and therefore we had to include all electrons. As it can be seen ANO-RCC basis-set using Douglas-Kroll-Hess 2nd order scalar relativistic calculation performs better than the rest among basis-sets listed in the Tables 3.1–3.3. However, ANO-RCC requires enormous computational resources due to presence of large number of basis functions. Stuttgart effective core potential and associated basis-sets on the other hand provide comparable accuracy at reasonable computational resource.

Thorium, in open shell configuration, shows a strong multi-reference character. B3PW91 functional results in correct ground state of thorium atom which is a triplet ($[Rn]6d^27s^2$), while the HF method yield a different triplet $[Rn]5f^27s^2$ for all three effective core potentials listed in Table 3.1. Moreover, both MWB60 and MWB60-ANO effective core potential and associated basis-sets yield a quintet for thorium atom ($[Rn]5f^17s^17p^2$) at HF level which is lower in energy than the triplet ($[Rn]5f^27s^2$) with energy difference of 11.03 and 28.03 kcal/mol, respectively. Similarly, the B3PW91 functional identifies the correct ground state of Th^{1+} ion, which is a quartet ($[Rn]6d^27s^1$), while the HF yields a different quartet $[Rn]5f^27s^1$. In addition, HF results in a doublet ($[Rn]5f^17s^2$) with lower energy than the quartet $[Rn]5f^27s^1$. In the case of Th^{2+} ion, only ANO-RCC basis-set yields the correct ground state $[Rn]5f^16d^1$, while all other basis-sets give a different triplet $[Rn]5f^17s^1$ at both HF and B3PW91 levels with only one exception: the ECP60MWB basis-set yields a singlet ($[Rn]7s^2$), which has lower energy than the triplet ($[Rn]5f^17s^1$) with energy differences of 18.82 and 11.42 kcal/mol at MP2 and CCSD(T) levels, respectively. The first and second ionization potential of thorium using B3PW91 functional is calculated to be 6.01 and 12.06 eV respectively. These are in good agreement with the experimental values[98] of 6.307 and 11.9 eV, respectively.

Table 3.1. Comparisons of the First and Second Ionization Energies (eV) of Thorium at Several Levels of Theory[a]

basis-set	IP I HF	IP I MP2	IP I CCSD(T)	IP I B3PW91	IP II HF	IP II MP2	IP II CCSD(T)	IP II B3PW91
ECP60MWB (8s7p6d4f)	1.90[d]	1.50[e]	5.56[e]	6.08	10.8[d]	11.32[e]	11.56[e]	12.07

Table 3.1 Continued[a]

basis-set	IP I HF	IP I MP2	IP I CCSD(T)	IP I B3PW91	IP II HF	IP II MP2	IP II CCSD(T)	IP II B3PW91
ECP60MWB (8s7p6d4f)	1.90[d]	1.50[e]	5.56[e]	6.08	10.8[d]	11.32[e]	11.56[e]	12.07
ECP60MWB_ANO (6s6p5d4f3g)	1.80[d]	2.26[f]	3.46[f]	6.13	10.73[d]	12.21[f]	12.06[f]	11.96
ECP60MWB_SEG (10s9p5d4f3g)	1.52[f]	2.70[f]	3.11[g]	6.01	10.89[f]	12.10[f]	12.07[g]	12.06
ANO-RCC[b] (13s11p10d8f6g3h)	7.04	6.62		6.04	7.42	9.17		11.93
Experiment[c]				6.307				11.9

[a]Ground state electronic structures reported in literature[89] are $Th(^3F_2)$ = $[Rn]6d^27s^2$, $Th^+(^4F_{3/2})$ = $[Rn]6d^27s^1$, $Th^{2+}(^1G_4)$ = $[Rn]5f^16d^1$. IP I = E(cation) – E(neutral); IP II = E(dication) – E(cation).

[b]ANO-RCC uses Douglas-Kroll-Hess 2nd order scalar relativistic calculation.

[c] Experimental values[98]

[d] neutral = quintet; cation = doublet; dication = triplet

[e] neutral = triplet; cation = doublet; dication = singlet

[f] neutral = triplet; cation = doublet; dication = triplet

[g] neutral = singlet; cation = doublet; dication = triplet

Resembling thorium, we observed several single determinant wavefunctions close in energy to the one of the ground state determinant for uranium, depending on level of theory and basis-set employed. We believe that the main electronic configuration (slater determinant) has a mixing of other determinants simply due to closeness in energies (eigenvalues) with the excited determinants (eigenfunctions). As long as a level of theory yields correct energies, we can conclude that the leading configuration represents quite well the real wavefunction, which are bypassed anyway by DFT when using the electronic density. Only ANO-RCC basis-set at HF results in correct ground

state of uranium atom which is a quintet ([Rn]$5f^3 6d^1 7s^2$) while all other methods/basis-sets yield a different quintet state. This is the reason for negative or very low ionization energy as listed in Table 3.2. B3PW91 functional yields the [Rn]$5f^4 7s^2$ quintet for all basis-sets used. ECP60MWB and ECP60MWB-ANO basis-sets yield a triplet excited state [Rn]$5f^1 6d^3 7s^2$ at HF level, which is lower in energy than the corresponding quintet state [Rn]$5f^2 6d^2 7s^2$.

Table 3.2. Comparisons of the First and Second Ionization Energies (eV) of Uranium at Several Levels of Theory[a]

basis-set	IP I HF	IP I MP2	IP I CCSD(T)	IP I B3PW91	IP II HF	IP II MP2	IP II CCSD(T)	IP II B3PW91
LANL2DZ (3s3p2d2f)	2.48	3.42	3.57	5.27[e]	13.04	13.46	13.11	10.41[e]
ECP60MWB (8s7p6d4f)	-0.28[d]	1.71[d]	2.19	5.55[e]	12.45	13.84	13.43	11.53[e]
ECP60MWB_ANO (6s6p5d4f3g)	3.88	3.61[d]	4.20	5.60[e]	13.32	12.48	13.34	11.53[e]
ECP60MWB_SEG (10s9p5d4f3g)	3.22	3.34	3.82	4.93[e]	12.52	12.68	12.76	11.53[e]
ANO-RCC[b] (12s10p9d7f5g3h)	5.27	5.57		5.68	12.26	12.54		11.42
Experiment[c]				6.194				10.6

[a]Ground state electronic structures indicated in literature[89] are $U(^5L_6)$ = [Rn]$5f^3 6d^1 7s^2$, $U^+(^4I_{9/2})$ = [Rn]$5f^3 7s^2$, $U^{2+}(^5I_4)$ =[Rn]$5f^4$. IP I = E(cation) – E(neutral); IP II = E(dication) – E(cation).

[b]ANO-RCC uses Douglas-Kroll-Hess 2nd order scalar relativistic calculation.

[c]Experimental values[98]

[d] neutral = triplet; cation = quartet; dication = quintet

[e] neutral = quintet; cation = sextet; dication = quintet

For U^{1+} ion, all the listed basis-sets, including LANL2DZ, result in the correct quartet ground state $[Rn]5f^3 7s^2$ at the HF level; however, the B3PW91 functional yields a sextet $[Rn]5f^4 7s^1$ with a lower energy than the one corresponding quartet $[Rn]5f^3 7s^2$; with an energy difference between 6.6 and 10.9 kcal/mol, using different ECP basis-sets. U^{2+} ion was always found to be quintet $[Rn]5f^4$ as reported in earlier published work.[89] The first and second ionization potentials of uranium using B3PW91 functional are calculated to be 5.27 and 11.19 eV, respectively. The experimental values for IP I and IP II are 6.19 and 10.6 eV respectively.

The ground state of plutonium atom is calculated to be a septet $[Rn]5f^6 7s^2$, while that of singly ionized ion Pu^{1+} is found to be an octet $[Rn]5f^6 7s^1$ at both HF as well as B3PW91 level of theory, matching earlier published results[89]. The first ionization potential of plutonium using B3PW91/ECP60MWB_SEG (Table 3.3) is estimated as 5.72 eV (expt. value 6.03 eV); however, it falls perfectly in the range 5.69–5.74 eV obtained with the same basis-set but with state-averaged CASSCF with subsequent multi-reference averaged coupled-pair functional calculations.[87,89]

Table 3.3. Comparisons of the First Ionization Energy (IP I eV) of Plutonium at Several Levels of Theory[a]

basis-set	HF	MP2	CCSD(T)	B3PW91
LANL2DZ (3s3p2d2f)	3.76	4.91	4.83	4.85
ECP60MWB (8s7p6d4f)	4.78	5.69	5.75	5.71
ECP60MWB_ANO (6s6p5d4f3g)	4.77	5.84	5.82	5.72

Table 3.3 Continued.

basis-set	HF	MP2	CCSD(T)	B3PW91
ECP60MWB_SEG (10s9p5d4f3g)	4.77	5.84	5.82	5.67
ANO-RCC[b] (12s10p9d8f5g3h)	4.73	5.93		5.68
Experiment[c]				6.026

[a] Ground state electronic structures indicated in literature[89] matches with our calculated results: $Pu(^7F_0)$ = $[Rn]5f^67s^2$, $Pu^+(^8F_{1/2})$ = $[Rn]f^6s^1$. IP I = E(cation) – E(neutral); IP II = E(dication) – E(cation).

[b] ANO-RCC uses Douglas-Kroll-Hess 2nd order scalar relativistic calculation.

[c] Experimental value[98]

The values thus obtained clearly indicate that B3PW91 functional performs better than Hartree-Fock, second-order Møller-Plesset perturbation theory (MP2) as well as CCSD(T) using the same basis-set, with ANO-RCC being an exception. Even though the focus of the paper is on large molecules and complexes, it is instructive to verify the quality of level of theory when applied to the individual isolated ion components of those molecules and complexes. The ions, when they are part of the complex, carry several of their intrinsic properties to the complex and therefore a precise reproduction of their individual behavior can be traced back to the properties of the individual ions. On the other hand, ionization potentials are the only available precise experimental information for those ions. Our calculations showed that our methods work pretty well when compared to such precise experimental information. With some exceptions, it is our experience that a suitable level of theory could be tested with properties that are different to those we want to evaluate; since we assume it is good, therefore, it should

properly work with any related properties such as energetics. As a matter of fact and simply for practical purposes, most levels of theory are tested against standard heats of formation of a data base of precise experimental results. Thus we fill that these comparisons add some sort of validity to our calculations. Therefore, we selected B3PW91 functional along with ECP60MWB_SEG basis-set for uranium and plutonium to perform further calculations. Other commonly used functionals for lanthanides and actinides are B3LYP and PBE.[17]

In order to validate our level of theory and basis-set for higher oxidation states, our rule is to calculate higher spin states until we find three consecutive ones in which the energy always increases. As already mentioned in our earlier work[37], uranium exists predominantly in the form of uranyl (VI) complexes in solution, while plutonium can exist as Pu^{3+}, Pu^{4+}, PuO^{+}, and PuO_2^{2+}. For plutonium, it is known that the complexation strength increases in the order: Pu(IV) > Pu(VI) > Pu(III) > Pu(V). Therefore, we considered two or more spin states for each of the bare ions (UO_2^{2+}, PuO_2^{2+}, Pu^{4+} and Th^{4+}) to find lowest energy spin-state. The ground state multiplicity for UO_2^{2+} and Th^{4+} were found to be singlet, while PuO_2^{2+} was a triplet and Pu^{4+} a quintet.[37] As already discussed, these actinides tend to form strong bound complexes with common counter-ions present in nuclear waste water. We also showed in our earlier work[37] that the lowest energy spin state of their complexes is same as that of the bare ion. We performed geometry optimizations for several uranium (VI) and plutonium (IV, VI) complexes both in vacuum as well as in solution using the CPCM solvation model. The bond lengths thus obtained were compared to experimental data whenever available as shown in Table

3.4. From these comparisons, we conclude that adding a solvation model improves the estimation of structural parameters, which get closer to experimental values in most cases. We find that DFT usually over-predicts actinide–water bond by <0.05 Å compared to experimental values. The higher difference in actinide–chloride bond may be a result of using a smaller basis-set 6-31G(d).

Table 3.4. Bond Lengths (Å) of UO_2^{2+}, PuO_2^{2+} and Pu^{4+} Complexes Calculated at B3PW91/SDD Level of Theory and Comparison with Experimental Values

complex	parameters	in vacuum	in solution	expt.[13,99-101]
$UO_2(H_2O)_5^{2+}$	U=O	1.74	1.74	1.78
	$U–O_w$	2.47	2.45	2.41
$PuO_2(H_2O)_5^{2+}$	Pu=O	1.70	1.70	1.74
	$Pu–O_w$	2.44	2.42	2.41
$UO_2(NO_3)_2(H_2O)_2$	U=O	1.76	1.76	1.76±0.01
	$U–O_w$	2.53	2.51	2.49±0.02
	$U–O_n$	2.46	2.47	2.45±0.01
$PuO_2(NO_3)_2(H_2O)_2$	Pu=O	1.72	1.72	1.73
	$Pu–O_w$	2.51	2.50	2.43
	$Pu–O_n$	2.45	2.46	2.50
$PuO_2Cl_1(H_2O)_4$	Pu=O	1.76	1.77	1.75
	$Pu–O_w$	2.62	2.59	2.43
	Pu–Cl	2.81	2.98	2.75
$PuO_2Cl_2(H_2O)_3$	Pu=O	1.71	1.72	1.75
	$Pu–O_w$	2.52	2.50	2.49
	Pu–Cl	2.65	2.66	2.70
$Pu(H_2O)_8^{2+}$	$Pu–O_w$	2.41		2.39
$Pu(NO_3)_4(H_2O)_3$	$Pu–O_{w/n}$	2.39–2.51	2.45	2.46
$UO_2Cl_1(H_2O)_4^{1+}$	U=O	1.75	1.75	1.76
	$U–O_w$	2.53	2.49	2.41
	U–Cl	2.57	2.63	2.71

Table 3.4 Continued.

complex	parameters	in vacuum	in solution	expt.[13,99-101]
	U=O	1.75	1.76	1.76
$UO_2Cl_2(H_2O)_3$	$U–O_w$	2.54	2.52	2.50
	U–Cl	2.67	2.68	2.73

3.3.1 Structure of first coordination shell of solvated Th^{4+} and Pu^{4+} ions

We performed ab-initio density functional theory calculations using the B3PW91 functional and relativistic small core potential with associated basis-set for thorium and plutonium and the 6-311++G(d,p) basis-set for O,H atoms to study the hydration of Th^{4+} and Pu^{4+} ions. The bond lengths as well as both corrected and uncorrected binding energy are listed in Table 3.5. The binding energy was calculated as the difference between energy of optimized $Th(H_2O)_n^{4+}$ and the energy sum of the constituents, and hence, includes the relaxation energy. The corrected binding energy was calculated by including both zero-point vibrational and dispersion corrections. The bond lengths calculated in vacuum are higher by 0.07 Å than those from experiment, 2.45–2.49 Å.[99-101]

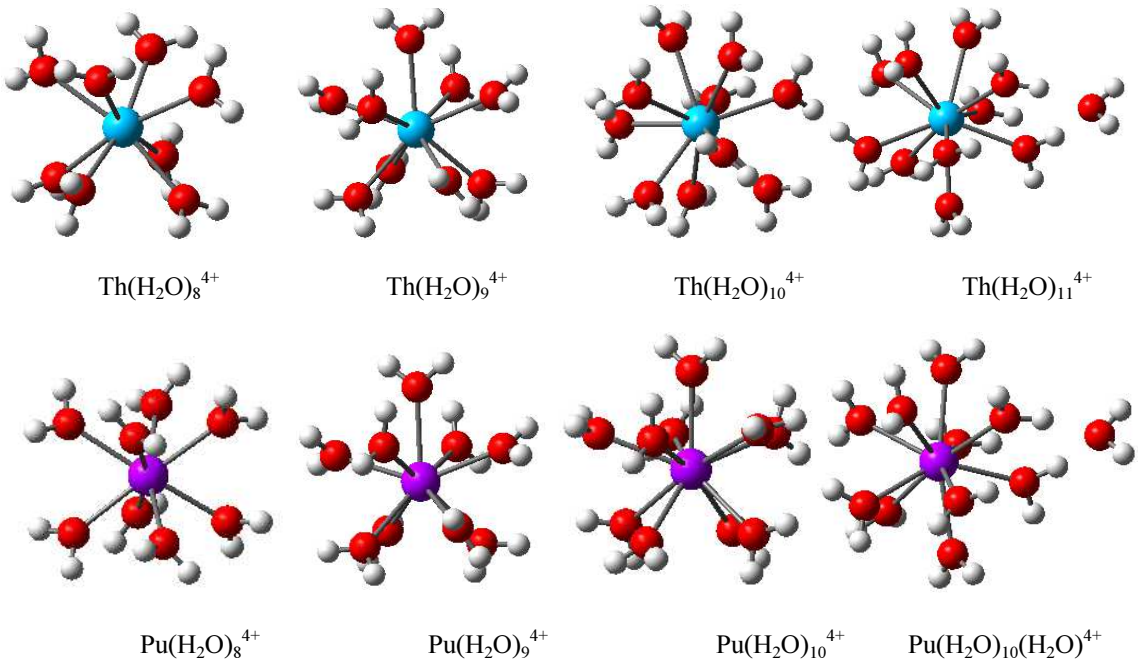

Figure 3.1 Optimized structures of Th(IV) and Pu(IV) hydrates using B3PW91 functional. Th (cyan), O (red), Pu (magenta), and H (white)

Table 3.5. Bond Lengths and Binding Energies[a] of Th(IV) and Pu(IV) Hydrates using B3PW91 Functional in vacuum (Experimental Values Are Given in Parentheses)

complex	M–O_w(Å)	E	ΔE_u	ΔZPE	ΔD	ΔE_c	ΔG[b]
$Th(H_2O)_8^{4+}$ [c]	2.49	-1017.83890	-766.6	19.3	-17.9	-765.2	-676.8
$Th(H_2O)_9^{4+}$	2.52 (2.45)	-1094.33458	-808.9	22.2	-22.9	-809.6	-706.9
$Th(H_2O)_{10}^{4+}$	2.57	-1170.80231	-833.7	25.0	-28.7	-837.4	-719.4
$Th(H_2O)_{11}^{4+}$	2.56 (2.46) 4.43 (4.66)	-1247.29433	-873.7	27.6	-30.9	-877.1	-746.7
$Pu(H_2O)_8^{4+}$ [d]	2.41 (2.39)	-1163.97989	-852.1	19.8	-25.9	-858.2	-762.1
$Pu(H_2O)_9^{4+}$	2.44	-1240.46946	-890.6	22.8	-32.1	-900.0	-787.0
$Pu(H_2O)_{10}^{4+}$	2.49	-1316.93531	-914.2	25.1	-38.8	-927.9	-799.1
$Pu(H_2O)_{11}^{4+}$	2.48, 4.37	-1393.43015	-956.0	27.7	-41.0	-969.3	-828.1

[a] Uncorrected binding energy $\Delta E_u = E(Th(H_2O)_n^{4+}) - E(Th^{4+}) - n \times E(H_2O)$. ΔZPE and ΔD are zero-point energy and dispersion corrections respectively obtained using similar expression as ΔE_u. Corrected binding energy $\Delta E_c = \Delta E_u + \Delta ZPE + \Delta D$. E is expressed in Ha and all others in kcal/mol. [b] $\Delta G = G(Th(H_2O)_n^{4+}) - G(Th^{4+}) - n \times G(H_2O)$. [c] Reported bond length using CPMD for $Th(H_2O)n^{4+}$ complex are Th–O_w = 2.46 Å, 2.49 Å, and 2.48 Å for n=8, 9, and 10 respectively.[23] [d] Reported bond length for $Pu(H_2O)_8^{4+}$ are 2.42 Å and 2.43 Å in gas phase using B3LYP and PBE functional.[17]

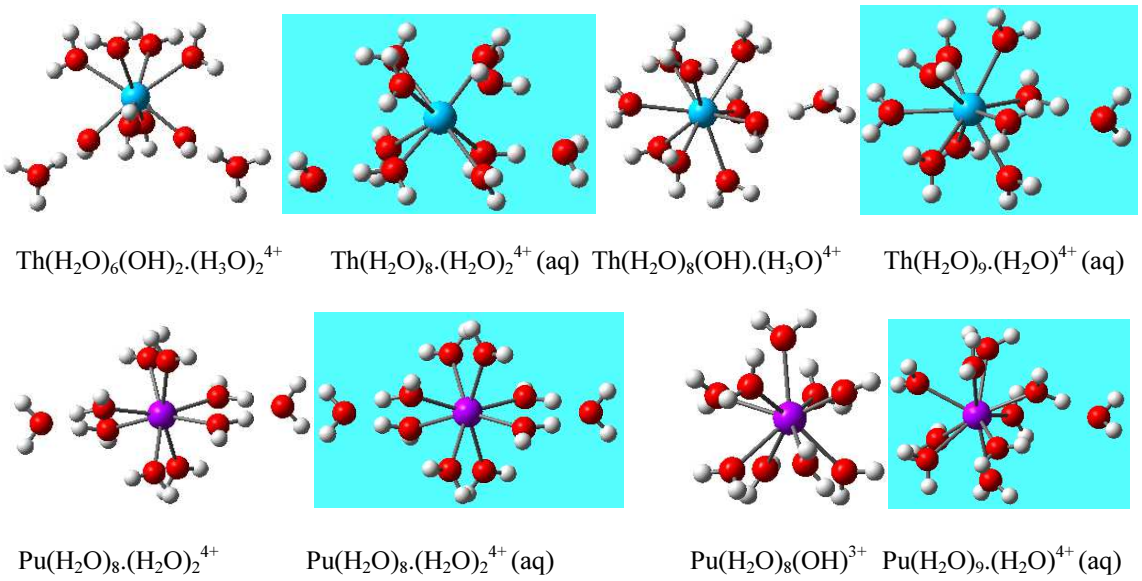

Figure 3.2 Effect of bulk solvent (CPCM) on coordination number of Th(IV) and Pu(IV) ions. Th (cyan), O (red), Pu (magenta), H (white), and CPCM calculated structures (blue background).

Our results indicate a coordination number of 8 being more stable than 9 or 10 for Th^{4+} ions if continuum water (light blue background in Figure 3.2) is used as inferred from Table 3.6. In vacuum, we observe hydrolysis effects leading to formation of $Th(H_2O)_6(OH)_2^{2+}$ and $Th(H_2O)_7(OH)^{3+}$ along with hydronium ions compared to stable 10 coordinated structure $Th(H_2O)_{10}^{4+}$. Previous study on the first hydration shell of Th^{4+} at B3LYP level using relativistic large core effective core potential,[20-21] indicated $Th(H_2O)_{10}^{4+}$ being most stable while $Th(H_2O)_8.(H_2O)_2^{4+}$ least stable and an energy difference of 0.23 kcal/mol between $Th(H_2O)_{10}^{4+}$ and $Th(H_2O)_9(H_2O)^{4+}$ complexes.[21] Spezia et al.[23] used EXAFS and classical molecular dynamics with polarizable force field to show that CN = 9 being most probable coordination number for Th(IV) ion at diluted conditions. A coordination number of 8–10 were reported for $Th(H_2O)_n^{4+}$

experimentally.[99-101] Our results match well with ab-initio results at MP2 level of theory as well as results obtained by molecular dynamics using polarizable force-field done previously to study coordination of Th(IV) ion in aqueous solvent.[22] It was shown that the first hydration shell consists of 8.25 ± 0.2 water molecules[22]. Our results are also in agreement with results obtained using AMOEBA force field where the (8+2)-coordination was again shown to have lowest binding energy among (9+1)-coordinated and 10-coordinated structures.[19] Yang et al.[20] reported 9-coordinated structure having lowest binding energy in solution phase while (8+2)-coordinated structure having lowest binding energy in gas phase. Spezia et al.[102] studied coordination of Th(IV) ion in water using single-sweep method coupled with Car-Parinello molecular dynamics and found that the 9-coordinated structure is the most stable among (8+1) and 10-coordinated structures based on change in free energy. Based on free energy calculations, we found that the free energy of (8+2)-coordinated structure is lower than (9+1)-coordinated structure by 4.3 kcal/mol and 11.2 kcal/mol lower than 10-coordinated structure. For aqueous thorium perchlorate solution, Johansson et al.[70] also found coordination number of 8.0±0.5 with Th–O_w bond distance of 2.485±0.010 Å using x-ray scattering experiments and also reported that first shell coordination number was not affected with perchlorate concentration, indicating that perchlorate do not form inner sphere complexes[70]. The difference in binding energy between (8+2)-coordinated structure and (9+1)-coordinated structure is 3 kcal/mol in solution, which is reduced to 1.7 kcal/mol considering ZPE and dispersion corrections.

In case of Pu^{4+} ion, $Pu(H_2O)_8.(H_2O)_2^{4+}$ is similarly found to be more stable than $Pu(H_2O)_9.(H_2O)^{4+}$ or $Pu(H_2O)_{10}^{4+}$ complexes when solvation effects are considered. The eight-coordinated complex has 2.3 kcal/mol lower binding energy than the nine-coordinated complex and 5.67 kcal/mol lower binding energy than the ten-coordinated complex (Table 3.6). Molecules in blue background indicate calculations done using the conductor-like polarizable continuum model.[94-95] In vacuum, we observed formation of hydrolysis products $Pu(H_2O)_8(OH)^{3+}$ and H_3O^+ which repel each other till they are infinitely separated. The energy shown for $Pu(H_2O)_9.(H_2O)^{4+}$ is the sum of energy of hydrolysis products. The solvation effects are critical in these cases as they suppress formation of hydrolysis products.

Table 3.6. Effect of Bulk Solvent on Total Energy of Th/Pu (IV) Hydrates using CPCM Technique with the B3PW91 Functional[a,b]

Complex	E	ΔE_u	ΔZPE	ΔD	ΔE_c	ΔG
		in vacuum				
$Th(H_2O)_6(OH)_2.(H_3O)_2^{4+}$	-1170.84066	-857.7(-820.1)[d]	21.6	-20.7	-856.9	-750.0
$Th(H_2O)_8(OH).(H_3O)^{4+}$	-1170.82880	-850.3 (-815.3)[d]	23.3	-24.0	-851.1	-739.3
$Th(H_2O)_{10}^{4+}$	-1170.80230	-833.7 (-804.7)[d]	25.0	-28.7	-837.4	-719.4
$Pu(H_2O)_8(H_2O)_2^{4+}$	-1316.98298	-944.1	25.2	-30.4	-949.3	-829.0
$Pu(H_2O)_8(OH).(H_3O)^{4+}$ [c]	-1317.23577	-1102.8	22.1	-30.2	-1110.8	-1002.2
$Pu(H_2O)_{10}^{4+}$	-1316.93531	-914.2	25.1	-38.8	-927.9	-799.1
		in solution				
$Th(H_2O)_8(H_2O)_2^{4+}$	-1171.80672	-7.0 (12.3)[e]	23.3	-22.5	-6.1	106.3
$Th(H_2O)_9(H_2O)^{4+}$	-1171.80196	-4.0 (0.2)[e]	25.2	-25.6	-4.4	110.5
$Th(H_2O)_{10}^{4+}$	-1171.78943	3.9 (0.0)[e]	24.6	-29.3	-0.8	117.5
$Pu(H_2O)_8(H_2O)_2^{4+}$	-1317.95372	-109.2	25.7	-30.7	-114.2	6.5

Table 3.6 Continued

Complex	E	ΔE_u	ΔZPE	ΔD	ΔE_c	ΔG
$Pu(H_2O)_9(H_2O)^{4+}$	-1317.9414	-101.5	24.1	-34.5	-111.9	12.3
$Pu(H_2O)_{10}^{4+}$	-1317.93232	-95.8	26.7	-39.4	-108.5	21.2

[a] E is expressed in Ha and all others in kcal/mol. See footnotes of Table 5 for nomenclature.

[b] The cavity surface area and cavity volume for $Th(H_2O)_n\cdot(H_2O)_{10-n}^{4+}$ are 315.409 Å^2 and 317.416 Å^3 while that for $Th(H_2O)_n\cdot(H_2O)_{10-n}^{4+}$ are 301.939 Å^2 and 306.984 Å^3 respectively.

[c] Total energy of hydrolysis products $Pu(H_2O)_8(OH)^{3+}$ and H_3O^+.

[d] Values reported in parenthesis are from B3LYP calculations published by Yang et al.[20]

[e] Values in parentheses are relative energies from B3LYP calculations using CPCM published by Tsushima et al.[21]

3.3.2 Solvation of U(VI) and Pu(IV/VI) nitrate-complexes

Based on molecular dynamics studies, Ye et al.[16] showed that divalent uranyl ions hydrated by five water molecules in equatorial plane are predominant form in aqueous solution. They also showed that nitrates associate with uranyl cation in monodentate fashion replacing one water molecule each, thus preserving five-fold co-ordination. Other form of nitrate complexes $UO_2(NO_3)^+$, $UO_2(NO_3)_2$, and $UO_2(NO_3)_3^-$ existed in small fractions which increased with nitric acid concentration. On the contrary Bühl et al.[15] showed using CPMD calculations that $UO_2(NO_3)_2$ complex with nitrates bonded in bidentate fashion are more stable in aqueous phase. They also observed formation of $UO_2(NO_3)^+$ complex with five coordination in a monodentate binding mode.[103] Therefore, the role of solvent is critical in studying solvation of these complexes. In a recent experimental work, structure of plutonyl di-nitrate complex

$Pu(NO_3)_2(H_2O)_2 \cdot H_2O$ was studied both in crystalline form and in solution using vis-NIR and Raman spectroscopy.[104] The solution electronic spectrum revealed mono-nitrate complex domination with negligible di-nitrate complex. We carried out DFT calculations on these complexes, both in vacuum and solution phase using CPCM models. Among di-nitrate complexes, $UO_2(NO_3)_2(H_2O)_2 \cdot H_2O$ complex has lower binding energy than $UO_2(NO_3)_2(H_2O)_3$ and shows a coordination number of 6 with two nitrates in bidentate mode (Table 3.7). We also studied in detail $UO_2(NO_3)_2(H_2O)_5$ and $PuO_2(NO_3)_2(H_2O)_5$ clusters in order to compare stability of different conformers. As shown in Table 8, $UO_2(NO_3)_2$ complex with nitrates in mono-dentate mode is more stable both in vacuum and solution phase than hydrated mono-nitrate complex as well as completely solvated $UO_2(H_2O)_5^{2+}$ ions with counter-ions far from the central ion (Table 3.8). In vacuum, O–H bonds break forming HNO_3 molecules and OH^- ions bound to the UO_2^{2+} ion in case of mono-nitrate and completely solvated nitrate complexes (Figure 3.3). The difference in binding energy between non-dissociated uranyl-nitrate complex and hydrated mono-nitrate complex is 8.2 kcal/mol (nitrate in bidentate mode) and 9.4 kcal/mol (nitrate in monodentate mode). The difference in binding energy between non-dissociated and completely solvated uranyl-nitrate complexes is 19.6 kcal/mol. Thus nitrate prefers to bind in bidentate mode in case of uranyl mono-nitrate complex in vacuum though the difference in binding energy between monodentate and bidentate is 1.2 kcal/mol only. If we consider the effect of bulk solvents, we do not observe formation of hydroxides though the O–H bond length in water increases up to 1.05 Å. In solution, the difference in energy between non-dissociated and hydrated mono-nitrate

complexes reduced to 5.4 kcal/mol for bidentate and 3.0 kcal/mol for monodentate respectively. This means that monodentate mode is preferred than bidentate mode for mono-nitrate complex in solution phase; however, based on free energy changes, both are equally probable. If we ignore corrections to binding energy, the difference between monodentate and bidentate mono-nitrate complex is only 0.2 kcal/mol. The difference in binding energy between non-dissociated and completely solvated uranyl-nitrate complexes is 15.8 kcal/mol.We repeat the calculations for PuO_2^{2+} ions as well. Similar behavior is observed for nitrate complexes of PuO_2^{2+}. $PuO_2(NO_3)_2$ complex with nitrates in mono-dentate mode are more stable in vacuum as well as solution than hydrated mono-nitrate as well as completely solvated $PuO_2(H_2O)_5^{2+}$ ions with counter-ions far from the central ion. The energy difference between non-dissociated and hydrated mono-nitrate complex is 9.2 kcal/mol for bidentate and 9.8 kcal/mol for monodentate complexes; these energies are reduced to 6.5 kcal/mol and 6.6 kcal/mol, respectively, using the solvation model. This means that both monodentate and bidentate are equally favored for the mono-nitrate complex in solution phase; however based on free energy changes, bidentate is preferred over monodentate. The difference in binding energy between non-dissociated and completely solvated plutonyl-nitrate complex is 20.1 kcal/mol in vacuum and 15.7 kcal/mol in solution. We observe that including both ZPE and dispersion corrections alter the binding energy by less than ~2 kcal/mol in above cases.

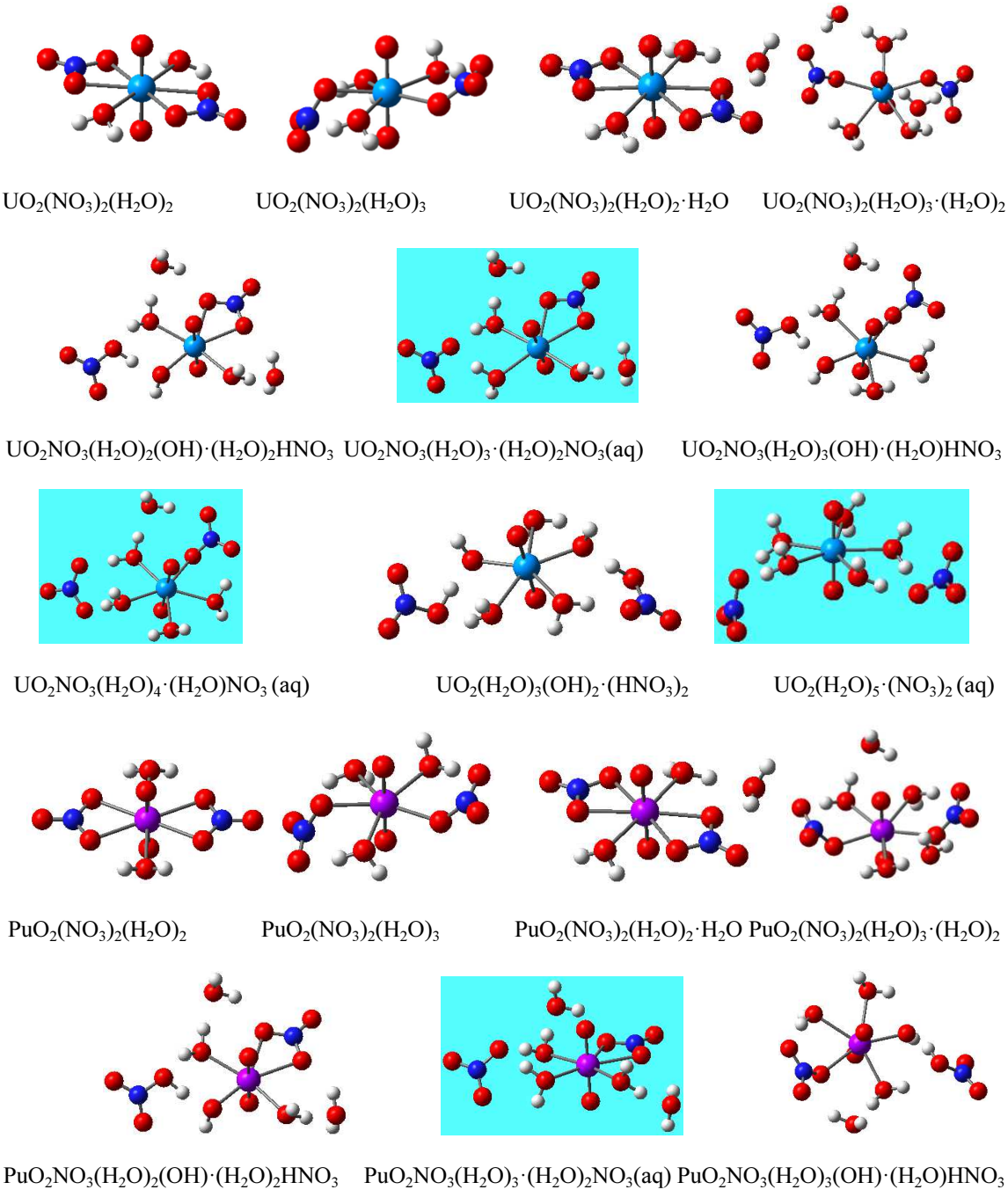

Figure 3.3. Optimized structures of hydrated UO_2^{2+} and PuO_2^{2+} nitrate complexes using B3PW91 functional. U (blue), O (red), Pu (magenta), N (dark blue), H (white), and CPCM calculated structures (blue background).

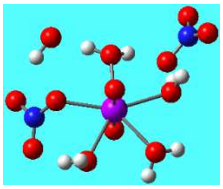

$PuO_2NO_3(H_2O)_4 \cdot (H_2O)NO_3$ (aq)

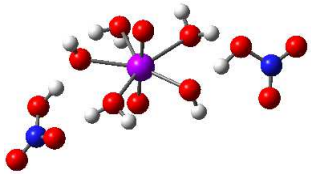

$PuO_2(H_2O)_3(OH)_2 \cdot (HNO_3)_2$

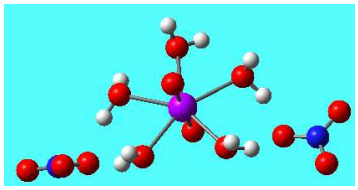

$PuO_2(H_2O)_5 \cdot (NO_3)_2$ (aq)

Figure 3.3 Continued.

Table 3.7. Bond Lengths and Total Energy of Hydrated UO_2^{2+} and PuO_2^{2+} Nitrate Complexes using B3PW91 Functional[a]

complex	M–O_w (Å)	M–O_N (Å)	E	ΔE_u	ΔZPE	ΔD	ΔE_c	ΔG
			in vacuum					
$UO_2(NO_3)_2(H_2O)_2$	2.53	2.46	-1340.93304	-590.4	7.4	-10.2	-593.3	-546.2
$UO_2(NO_3)_2(H_2O)_3$	2.53	2.30	-1417.32142	-595.8	10.6	-15.1	-600.3	-539.1
$UO_2(NO_3)_2(H_2O)_2 \cdot H_2O$	2.50	2.48	-1417.33916	-606.9	10.3	-12.7	-609.4	-550.8
$PuO_2(NO_3)_2(H_2O)_2$	2.51	2.44	-1417.81304	-576.7	7.7	-12.1	-581.2	-530.2
$PuO_2(NO_3)_2(H_2O)_3$	2.51	2.27	-1494.20297	-583.0	10.8	-18.1	-590.3	-524.0
$PuO_2(NO_3)_2(H_2O)_2 \cdot H_2O$	2.49	2.46	-1494.21804	-592.5	10.5	-14.8	-596.8	-534.2
			in solution					
$UO_2(NO_3)_2(H_2O)_2$	2.51 (2.59)[b]	2.47 (2.43)[b]	-1340.95447	-96.8	7.2	-10.3	-99.9	-52.8
$UO_2(NO_3)_2(H_2O)_3$	2.48	2.33	-1417.34612	-99.4	9.8	-14.4	-104.0	-44.4
$UO_2(NO_3)_2(H_2O)_2 \cdot H_2O$	2.48	2.48	-1417.36043	-108.4	9.7	-12.7	-111.4	-53.2
$PuO_2(NO_3)_2(H_2O)_2$	2.49	2.46	-1417.83279	-103.1	7.5	-12.2	-107.8	-58.1
$PuO_2(NO_3)_2(H_2O)_3$	2.47	2.31	-1494.22565	-106.5	10.5	-17.5	-113.5	-49.3
$PuO_2(NO_3)_2(H_2O)_2 \cdot H_2O$	2.47	2.47	-1494.23785	-114.2	10.2	-14.8	-118.8	-58.0

[a] E is expressed in Ha and all other energies in kcal/mol. See footnotes of Table 5 for nomenclature.

[b] U–Ow and U–ON bond lengths reported using CPMD in solution by Bühl et al.[103]

Table 3.8. Calculated Binding Energy of $UO_2(NO_3)_2(H_2O)_5$ and $PuO_2(NO_3)_2(H_2O)_5$ clusters using B3PW91 Functional[a]

complex	E	ΔE_u	ΔZPE	ΔD	ΔE_c	ΔG
		in vacuum				
$UO_2(NO_3)_2(H_2O)_3\cdot(H_2O)_2$	-1570.13582	-630.1	15.6	-20.9	-635.4	-550.5
$UO_2NO_3(H_2O)_2(OH)\cdot(H_2O)_2\cdot HNO_3$	-1570.12467	-623.1	14.8	-18.9	-627.2	-546.5
$UO_2NO_3(H_2O)_3(OH)\cdot(H_2O)\cdot HNO_3$	-1570.12106	-620.9 (0.0)[b]	15.1	-20.2	-625.9	-542.2
$UO_2(H_2O)_3(OH)_2\cdot(HNO_3)_2$	-1570.10172	-608.7 (8.7)[b]	13.1	-20.1	-615.7	-533.1
$PuO_2(NO_3)_2(H_2O)_3\cdot(H_2O)_2$	-1647.01578	-616.3	16.4	-25.0	-624.9	-533.6
$PuO_2NO_3(H_2O)_2(OH)\cdot(H_2O)_2\cdot HNO_3$	-1647.00475	-609.4	15.3	-21.6	-615.7	-529.8
$PuO_2NO_3(H_2O)_3(OH)\cdot(H_2O)\cdot HNO_3$	-1647.00084	-607.0	15.5	-23.7	-615.1	-526.0
$PuO_2(H_2O)_3(OH)_2\cdot(HNO_3)_2$	-1646.98245	-595.4	14.3	-23.6	-604.8	-516.4
		in solution				
$UO_2(NO_3)_2(H_2O)_3\cdot(H_2O)_2$	-1570.16153	-124.9	14.5	-19.8	-130.1	-47.8
$UO_2NO_3(H_2O)_3\cdot(H_2O)_2NO_3$	-1570.15414	-120.3	14.4	-18.9	-124.8	-43.3 (2.5)[c]
$UO_2NO_3(H_2O)_4\cdot(H_2O)NO_3$	-1570.15453	-120.5	14.2	-20.9	-127.2	-43.1 (0.0)[c]
$UO_2(H_2O)_5\cdot(NO_3)_2$	-1570.13449	-107.9	14.0	-20.3	-114.3	-31.2
$PuO_2(NO_3)_2(H_2O)_3\cdot(H_2O)_2$	-1647.04087	-131.9	16.0	-24.2	-140.0	-50.5
$PuO_2NO_3(H_2O)_3\cdot(H_2O)_2NO_3$	-1647.03178	-126.2	14.6	-22.0	-133.5	-48.1
$PuO_2NO_3(H_2O)_4\cdot(H_2O)NO_3$	-1647.02907	-124.5	15.3	-24.3	-133.4	-44.5
$PuO_2(H_2O)_5\cdot(NO_3)_2$	-1647.01392	-114.9	14.9	-24.3	-124.3	-36.6

[a] E is expressed in Ha and all others in kcal/mol. See footnotes of Table 3.5 for nomenclature.

[b] Value in parentheses are relative energy of bidentate and monodentate $UO_2NO_3(H_2O)_4^+$ complex calculated using CPMD in gas phase by Bühl et al.[15]

[c] Value in parentheses are relative free energy of bidentate and monodentate $UO_2NO_3(H_2O)_4^+$ complex calculated using CPMD in aqueous phase by Bühl et al.[15]

For Pu(IV) ion, four nitrates are bonded to Pu(IV) ion in bidentate mode in first coordination shell. In order to study solvation of $Pu(NO_3)_4$ salt in water, we start by adding water molecules and optimize the structure. We observed that nitrates are very strongly bonded to Pu(IV) ion and they do not dissociate easily. The coordination number of first shell increases from 10 to 12 (Figure 3.4) and remains unchanged thereafter on addition of more water molecules to the system. The first coordinate shell can accommodate four water molecules in addition to four nitrates. Any additional water molecule ends up in the second coordination shell. In order to compare the stability of solvated ion, we also optimized the structure of $Pu(NO_3)_3(H_2O)_{6\cdot NO_3}$ and compare its energy with $Pu(NO_3)_4(H_2O)_4\cdot(H_2O)_2$. The binding energy of solvated ion is 9.8 kcal/mol higher indicating nitrates prefer to stay in first coordination shell (Table 3.9). When solvent effects are included, the difference in binding energy is reduced to 6.2 kcal/mol and follows an expected trend. We further increased number of water molecules to 8 to obtain second coordination shell of solvent molecules. Our calculations still show no dissociation of nitrates from the central ion. Water molecules in the second shell arrange themselves forming hydrogen bonds with those present in first shell.

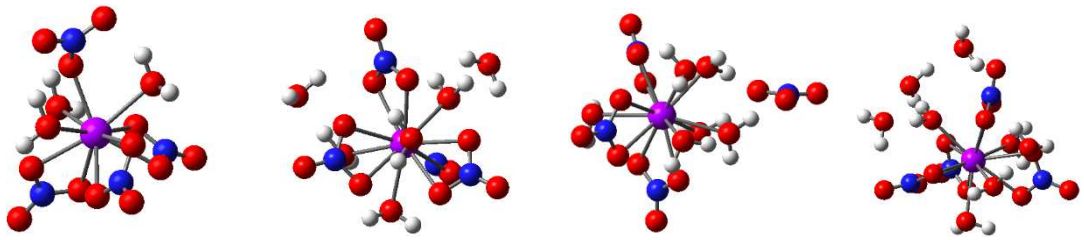

$Pu(NO_3)_4(H_2O)_3$ $Pu(NO_3)_4(H_2O)_4\cdot(H_2O)_2$ $Pu(NO_3)_3(H_2O)_6\cdot NO_3$ $Pu(NO_3)_4(H_2O)_4\cdot(H_2O)_4$

Figure 3.4. Optimized structures of hydrated Pu(IV) nitrate complexes using B3PW91 functional. Pu (magenta), O (red), N (dark blue), and H (white)

Table 3.9. Bond Lengths and Total Energy of Hydrated Pu(IV) Nitrate Complexes using B3PW91 Functional[a]

complex	$Pu–O_W$	$Pu–O_N$	E	ΔE_u	ΔZPE	ΔD	ΔE_c	ΔG
			in vacuum					
$Pu(NO_3)_4(H_2O)_3$	2.51 (2.50)[b]	2.39	-1904.26732	-1895.8	13.4	-23.5	-1906.0	-1809.6
$Pu(NO_3)_4(H_2O)_4\cdot(H_2O)_2$	2.55	2.49	-2133.47928	-1941.3	22.3	-39.2	-1958.2	-1816.4
$Pu(NO_3)_3(H_2O)_6\cdot NO_3$	2.58	2.46	-2133.46148	-1930.1	22.6	-40.8	-1948.4	-1805.0
$Pu(NO_3)_4(H_2O)_4\cdot(H_2O)_4$	2.52	2.51	-2286.28062	-1967.4	27.3	-44.9	-1985.0	-1820.2
			in solution					
$Pu(NO_3)_4(H_2O)_4\cdot(H_2O)_2$	2.54	2.49	-2133.50655	-285.0	21.5	-38.5	-301.9	-161.9
$Pu(NO_3)_3(H_2O)_6\cdot\cdot NO_3$	2.57	2.47	-2133.49399	-277.1	22.3	-40.9	-295.7	-152.7

[a] Lengths in Å, E in Ha, and all others energies in kcal/mol. See footnotes of Table 3.5 for nomenclature.

[b] In solution using B3LYP and PBE functionals.[17]

3.3.3 Solvation of Pu(IV) and Pu(VI) chloro-complexes

In this section, we study aquo-chloro complexes of Pu(IV) and Pu(VI) ions. Unlike nitrates, chlorides are weakly bonded to Pu(IV)/(VI) ions. We observe dissociation of counter-ions with as few as four water molecules during geometry optimization of Pu(IV) aquo-chloro complex itself. We optimized two conformers for $PuCl_4(H_2O)_4$. In one case, we found Cl^- leaves the first shell during optimization itself forming $PuCl_3(H_2O)_4^+$ and Cl^- ion, while in other case, all four chloride ions remain bonded to Pu(IV) ion. The energy difference between the two conformers is however only 1.1 kcal/mol (Table 3.10). The coordination number of U(IV) aquo complex has already been reported to be 8–9 in aqueous solution both theoretically[105-106] and experimentally[13]. The combined coordination of $N_{Cl}+N_{Ow}$ in U(IV) aquo-chloro complex was also reported experimentally to decrease from 9 to 8 with increase in chloride concentration.[13] The coordination number of Pu(IV) aquo complexes was found to be 8 using continuum model as explained in previous section. The coordination number for aquo-chloro complexes of Pu(IV) is also found to be 8 with three chlorides present in the first shell as shown in Figure 3.5. In order to confirm our findings, we also performed a geometry optimization for Pu(IV) aquo-chloro starting with a combined coordination of $N_{Cl}+N_{Ow}$ as 9. The final geometry reverts back to eight-coordination with a water molecule moving out of the first shell. The difference in binding energy between tetra-chloro complex $PuCl_4(H_2O)_5\cdot(H_2O)_2$ and tri-chloro complex $PuCl_3(H_2O)_5\cdot Cl(H_2O)_2$ is only 0.35 kcal/mol, and between tertra-chloro complex and di-chloro complex $PuCl_2(H_2O)_6\cdot Cl_2(H_2O)_1$ is calculated to be 13.3 kcal/mol in vacuum. However, using

solvation model, the binding energy of tri-chloro complex $PuCl_3(H_2O)_5 \cdot Cl(H_2O)_2$ is least among the three conformers. The observed trend in binding energy of these complexes remains unchanged if we ignore ZPE and dispersion corrections.

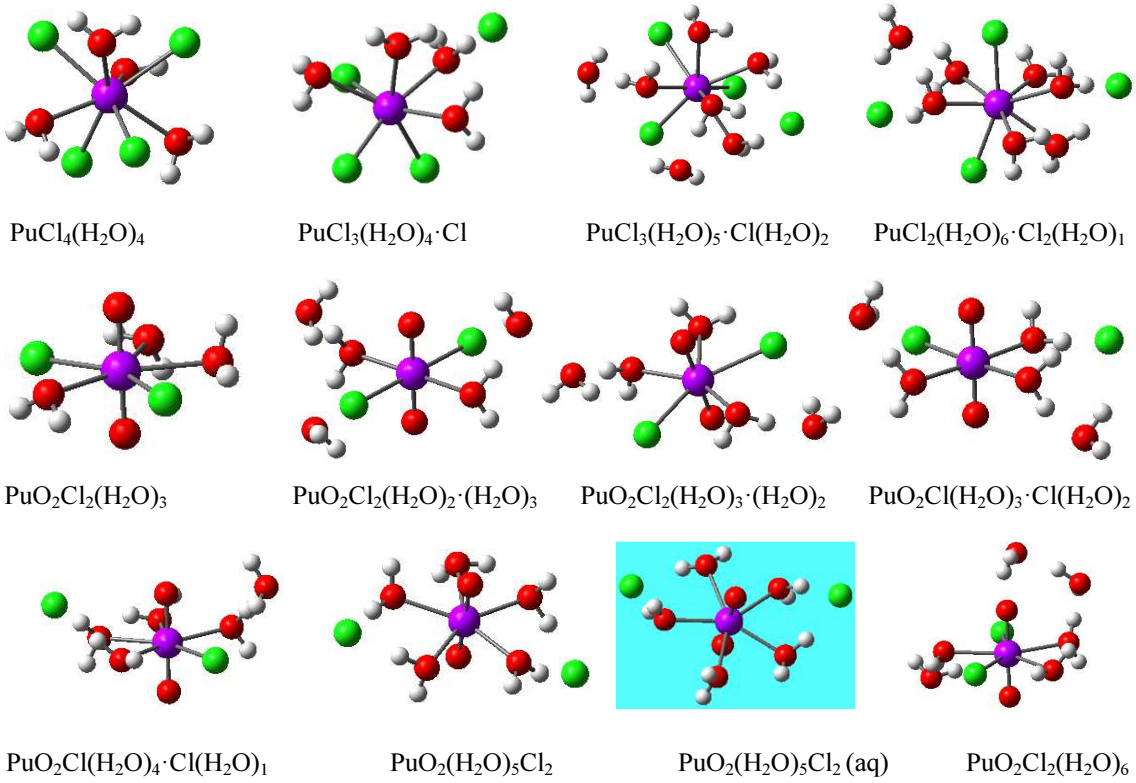

Figure 3.5. Optimized structures of hydrated Pu(IV) and Pu(VI) chloro complexes using B3PW91 functional. Pu (magenta), O (red), Cl (green), H (white), and CPCM calculated structures (blue background).

In the case of Pu(VI) chlorides, PuO_2^{2+} retain five-fold coordination number with two chlorides replacing two water molecules bonded to Pu(VI) ion. In order to study effect of dilution, we increased number of water molecules to 6. We observed that

chlorides remain bonded to the central cation with Pu–Cl bond length increasing from 2.49 Å to 2.69 Å (Table 3.10).

Table 3.10. Bond Lengths and Total Energy of Pu(IV) and Pu(VI) chloro complexes using B3PW91 Functional in Vacuum[a]

complex	Pu–O_w (Å)	Pu–Cl (Å)	E	ΔE_u	ΔZPE	ΔD	ΔE_c	ΔG
$PuCl_4(H_2O)_4$	2.50	2.62	-2700.52871	-1900.5	12.1	-20.5	-1908.9	-1825.58
$PuCl_3(H_2O)_4 \cdot Cl$	2.44	2.54	-2700.52621	-1898.9	11.3	-20.2	-1907.8	-1823.19
$PuO_2Cl_2(H_2O)_3$	2.58 (2.55)[b]	2.61 (2.67)[b]	-1854.14221	-584.4	8.7	-13.3	-588.9	-536.52
$PuO_2Cl_2(H_2O)_6$	2.47	2.69	-2083.35510	-630.4	16.7	-23.8	-637.6	-547.30

[a] E is expressed in Ha and all others in kcal/mol. See footnotes of Table 5 for nomenclature.

[b] Reported bond lengths for $PuO_2Cl_2(H_2O)_3$ in gas phase using B3LYP and PBE functional.[17]

We also obtained the optimized structure of different conformers of $PuO_2Cl_2(H_2O)_5$ to compare their relative stability as shown in Table 3.11. Among different conformers, $PuO_2Cl_2(H_2O)_2 \cdot (H_2O)_3$ is the most stable due to lowest binding energy and $PuO_2(H_2O)_5Cl_2$ is the least stable in vacuum, indicating chlorides prefer to remain bonded to Pu(VI) ion. On introducing solvation effects, the difference in binding energy between di-chloro complex $PuO_2Cl_2(H_2O)_2 \cdot (H_2O)_3$ and mono-chloro complex $PuO_2Cl(H_2O)_4 \cdot Cl(H_2O)_1$ is reduced to 1.56 kcal/mol. The binding energy of mono-chloro complex $PuO_2Cl(H_2O)_3 \cdot Cl(H_2O)_2$ is however 5.42 kcal/mol higher than di-chloro complex. These results are in line with earlier published Car-Parrinello molecular dynamics simulation[14] of aquo-chloro complexes of U(VI) in aqueous solution where it

was shown that $PuO_2Cl_2(H_2O)_3 \cdot (H_2O)_2$ was stable for a few picoseconds and transform into more stable $PuO_2Cl_2(H_2O)_2 \cdot (H_2O)_3$ conformer.

Table 3.11. Calculated Binding Energy of $PuCl_4(H_2O)_7$ and $PuO_2Cl_2(H_2O)_5$ clusters using B3PW91 Functional[a]

complex	E	ΔEu	ΔZPE	ΔD	ΔEc	ΔG
			in vacuum			
$PuCl_4(H_2O)_5 \cdot (H_2O)_2$	-2929.74804	-1950.6	20.8	-34.2	-1963.9	-1837.3
$PuCl_3(H_2O)_5 \cdot Cl \cdot (H_2O)_2$	-2929.74552	-1949.0	20.6	-35.3	-1963.6	-1835.7
$PuCl_2(H_2O)_6 \cdot Cl_2 \cdot (H_2O)_1$	-2929.72409	-1935.5	19.8	-34.9	-1950.6	-1822.7
$PuO_2Cl_2(H_2O)_2 \cdot (H_2O)_3$	-2006.95861	-619.9	14.5	-21.2	-626.6	-548.0
$PuO_2Cl_2(H_2O)_3 \cdot (H_2O)_2$	-2006.95125	-615.3	13.9	-19.5	-620.9	-544.3
$PuO_2Cl(H_2O)_4 \cdot Cl \cdot (H_2O)_1$	-2006.93884	-607.5	13.0	-21.5	-616.0	-536.5
$PuO_2Cl(H_2O)_3 \cdot Cl \cdot (H_2O)_2$	-2006.93988	-608.2	13.5	-19.8	-614.4	-537.3
$PuO_2(H_2O)_5Cl_2$	-2006.91764	-594.2	11.1	-21.7	-604.9	-525.4
			in solution			
$PuCl_4(H_2O)_5 \cdot (H_2O)_2$	-2929.77091	-243.6	19.7	-34.3	-258.3	-132.8
$PuCl_3(H_2O)_5 \cdot Cl \cdot (H_2O)_2$	-2929.78413	-251.9	20.0	-33.4	-265.4	-139.8
$PuCl_2(H_2O)_6 \cdot Cl_2 \cdot (H_2O)_1$	-2929.76822	-241.9	19.5	-35.2	-257.6	-129.9
$PuO_2Cl_2(H_2O)_2 \cdot (H_2O)_3$	-2006.98410	-114.2	13.1	-17.8	-118.9	-46.7

Table 3.11 Continued.

complex	E	ΔEu	ΔZPE	ΔD	ΔEc	ΔG
$PuO_2Cl_2(H_2O)_3 \cdot (H_2O)_2$	-2006.98022	-111.7	13.5	-19.6	-117.8	-41.9
$PuO_2Cl(H_2O)_4 \cdot Cl \cdot (H_2O)_1$	-2006.97649	-109.4	13.2	-21.2	-117.4	-39.7
$PuO_2Cl(H_2O)_3 \cdot Cl \cdot (H_2O)_2$	-2006.97454	-108.2	12.8	-18.1	-113.5	-39.4
$PuO_2(H_2O)_5Cl_2$	-2006.96671	-103.2	12.7	-22.0	-112.6	-33.8

[a] E is expressed in Ha and all others in kcal/mol. See footnotes of Table 5 for nomenclature.

3.3.4 Solvation of Th(IV) chloro-complexes

We also optimized five different conformers of $ThCl_m(H_2O)_n \cdot (H_2O)_{10-n}Cl_{4-m}$ both in vacuum and in solution as shown in Table 3.12. A, B, and C have a coordination number ($N_w + N_{Cl}$) of 9 while D and E are 10-coordinated structures. Conformers F and G are also 9-coordinated structures but with three chlorides in the inner coordination sphere. Based on the binding energy, conformer G $ThCl_3(H_2O)_6 \cdot Cl(H_2O)_4$ is the most stable than other conformers in vacuum, while in solution conformer A $ThCl(H_2O)_8 \cdot Cl_3(H_2O)_2$ is the most stable. Moreover, the binding energies of conformers C, D and F are very similar in vacuum. In solution, C and E have similar binding energy. The binding energy of D, F and G are also very close which is very interesting due to the fact that D is a 10-coordinated structure with one chloride in first shell while F and G are 9-coordinated structure with three chlorides in first shell. Based on change in free energy, conformer A is most stable and $\Delta\Delta G$ between conformers A and G is 2.7

kcal/mol in solution. In vacuum, we observe a clear trend for ΔG with conformer G is found to be most stable with $\Delta\Delta G$ between conformers C and G is 6.1 kcal/mol. It can be thus concluded that chlorides remains in the first shell forming inner sphere complex with Th–Cl bond length varying between 2.74–2.85 Å in vacuum. The coordination number ($N_w + N_{Cl}$) is found to be 9–10. In solution, our results indicate that one chloride enters the first coordination shell at 2.71–2.84 Å as observed experimentally by Johansson et al.[99] using large angle x-ray scattering measurements. Their experimental results indicate that chlorides tend to form inner sphere complexes, which leads to increase in coordination number around thorium ion by addition of chloride ion to inner sphere.[99] Recent work done by Spezia et al.[23], however, found no evidence of chloride in first shell at low concentration, but observed chloride ion in first shell at a distance of ~2.9 Å at high concentration. Thus we can conclude that Pu(IV) ions binds chloride ions more strongly than Th(IV) ions do.

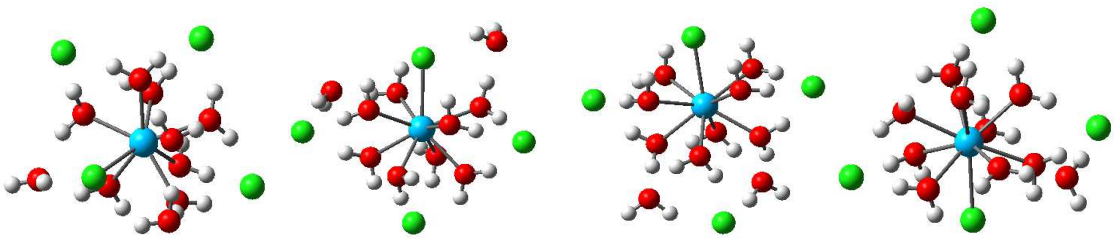

(A) (B) (C) (D)

Figure 3.6. Optimized structures of $ThCl_4(H_2O)_{10}$ clusters using B3PW91 functional. Th (cyan), O (red), Cl (green), H (white). A, B and C have a structural formula of $ThCl(H_2O)_8 \cdot (H_2O)_2Cl_3$. D and E have structural formula of $ThCl(H_2O)_9 \cdot (H_2O)_1Cl_3$. F and G have structural formula of $ThCl_3(H_2O)_6 \cdot (H_2O)_4Cl$.

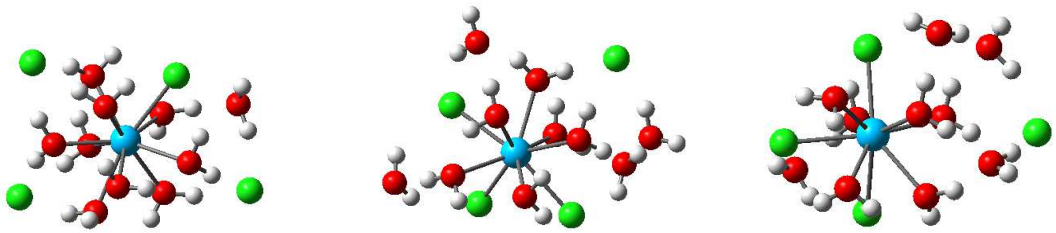

(E) (F) (G)

Figure 3.6 Continued.

Table 3.12. Calculated Binding Energy of $ThCl_4(H_2O)_{10}$ Clusters Using B3PW91 Functional[a]

complex	Th–Cl (Å)	*E*	ΔE_u	ΔZPE	ΔD	ΔE_c	ΔG
			in vacuum				
(A)	2.74, 4.17–4.34	-3012.77523	-1883.0	26.1	-40.6	-1897.5	-1735.1
(B)	2.85, 3.81–4.54	-3012.77730	-1884.3	25.8	-38.8	-1897.3	-1737.6
(C)	2.84, 4.26–4.68	-3012.78360	-1888.2	27.5	-39.4	-1900.2	-1738.5
(D)	2.82, 4.30–4.65	-3012.78156	-1887.0	27.1	-39.7	-1899.6	-1737.6
(E)	2.85, 4.29–4.51	-3012.78465	-1888.9	27.8	-41.0	-1902.1	-1737.9
(F)	2.68–2.81, 4.27	-3012.78544	-1889.4	29.0	-39.5	-1899.9	-1739.3
(G)	2.72–2.79, 5.10	-3012.79237	-1893.7	28.6	-39.0	-1904.1	-1744.6
			in solution				
(A)	2.71, 4.40–4.52	-3012.83608	-172.7	26.6	-39.7	-185.7	-25.4
(B)	2.84, 4.08–4.68	-3012.82801	-167.6	26.1	-39.6	-181.2	-20.7
(C)	2.83, 4.41–4.84	-3012.83397	-171.4	26.7	-39.5	-184.2	-23.9
(D)	2.82, 4.44–4.78	-3012.82922	-168.4	26.4	-40.3	-182.3	-21.1
(E)	2.83, 4.47–4.61	-3012.83273	-170.6	28.1	-41.5	-184.0	-19.3
(F)	2.78–2.83, 4.81	-3012.83226	-170.3	27.5	-39.5	-182.3	-22.7
(G)	2.76–2.78, 5.18	-3012.83337	-171.0	27.7	-39.0	-182.3	-22.8
Experiment[b]	2.8						

[a] E is expressed in Ha and all others in kcal/mol. See footnotes of Table 5 for nomenclature.

b Expeimental value[99]

3.4 Bonding nature of actinides with common counter-ions

Based on simple electronegativity difference between Pu(1.28), O(3.5) and Cl(3.0), the percentage ionic character of Pu–O and Pu–Cl bonds are 71% and 52% respectively. Similarly for U(1.38), the percentage ionic character of U–O and U–Cl bonds are 67% and 48% respectively. We performed a detailed natural bond order (NBO) analysis on several actinide complexes as shown in Table 3.13 to understand the nature of bonding present in actinide complexes with common counter-ions present in nuclear waste water.

Table 3.13. Summary of NBO Contribution Analysis for Common Actinide Complexes

complex	NC*	Actinide valence	bonds	Actinide (%)	$O/O_n/O_w$ (%)
$Th(H_2O)_8^{4+}$	2.27	$7S^{0.16}5f^{0.48}6d^{0.74}7p^{0.29}$	$Th–O_w$	6.7	93.3
$Pu(H_2O)_8^{4+}$	1.81	$7S^{0.19}5f^{4.76}6d^{0.80}7p^{0.35}$	$Pu–O_w$	10.2	89.9
$ThCl_4(H_2O)_7$	-0.04	$7S^{0.30}5f^{0.11}6d^{1.56}7p^{0.01}$	Th–Cl(1)	16.3	83.7
			Th–Cl(2)	4.6	95.4
			Th–Cl(3)	5.1	94.9
			$Th–O_w$	7.8	92.3
$PuCl_4(H_2O)_7$	0.30	$7S^{0.33}5f^{4.91}6d^{1.58}7p^{0.63}$	Pu–Cl	21.0	79.0
$UO_2(NO_3)_2(H_2O)_2 \cdot H_2O$	1.43	$7S^{0.20}5f^{2.62}6d^{1.44}7p^{0.41}$	$U–O_n$	10.7	89.3
$PuO_2(NO_3)_2(H_2O)_2 \cdot H_2O$	1.06	$7S^{0.21}5f^{5.14}6d^{1.35}7p^{0.40}$	$Pu–O_n$	12.3	87.8
			$Pu–O_w$	9.7	90.3
$UO_2Cl_2(H_2O)_3$	1.05	$7S^{0.23}5f^{2.71}6d^{1.63}7p^{0.17}$	U–Cl(1)	5.3	94.7
			U–Cl(2)	17.1	82.9
			U–Cl(3)	7.7	92.3

Table 3.13 Continued.

complex	NC*	Actinide valence	bonds	Actinide (%)	$O/O_n/O_w$ (%)
			$U–O_w$	8.5	91.5
$PuO_2Cl_2(H_2O)_3$	0.75	$7S^{0.25}5f^{5.17}6d^{1.53}7p^{0.45}$	Pu–Cl	21.1	78.9

*NC – natural charge

Based on NBO analysis of actinide complexes, we observe formation of covalent bonds between actinide ion and water as well as counter-ions present; however tending towards more ionic character. In case of $Th(H_2O)_8^{4+}$ complex, all $Th–O_w$ covalent bonds have very high contribution from water O atoms (93%). In case of $Pu(H_2O)_8^{4+}$ complex, we found only four $Pu–O_w$ covalent bonds, however the contribution from water O atoms was reduced to 90%. In case of $ThCl_4(H_2O)_7$ and $PuCl_4(H_2O)_7$, relatively stronger covalent bonds are formed between actinide and chloride ions with percentage contribution as high as 16% for Th(IV) and 18% in case of Pu(IV) ion. Unlike $ThCl_4(H_2O)_7$, we did not find covalent bonds between Pu(IV) and water O atoms in case of $PuCl_4(H_2O)_7$.

From NBO analysis performed on nitrate complex of actinyl species, we found covalent bonds formed between nitrate O atoms and U(VI) or Pu(VI) ions with percentage contribution from U(VI) being 10–11% and from Pu(VI) being 11–12%, respectively. We also found weak $Pu–O_w$ covalent bond for $PuO_2(NO_3)_2(H_2O)_2.(H_2O)$ with 90% contribution from water O atom.

3.5 Conclusions

Density functional theory has been applied to study the structure and solvation of U(VI), Pu(IV) and Pu(VI) using relativistic small core effective core potential. We found that zero-point vibrational energy corrections to the binding energies cancel nicely with the corresponding empirical dispersion corrections in vacuum despite the fact that these corrections individually contribute with up to 3%. In solution, dispersion corrections can exceed ZPE correction by up to 13% depending upon the size of the molecule; this may be due to the fact that these corrections are more suited to gas phase calculations. We also found that solvent effects are critical in examining the structure of these solvated ions. In vacuum, we observe hydrolysis of Pu(IV) ion for nine-coordination which was suppressed on introduction of solvent effects using polarizable continuum model. The eight-coordination was found to be most stable for both Th(IV) and Pu(IV) ions with nine-coordinated complex being 1.7 kcal/mol and 2.3 kcal/mol higher in energy for Th(IV) and Pu(IV) respectively. In case of U(VI) nitrate complexes, $UO_2(NO_3)_2$ complex with nitrates in mono-dentate mode is more stable both in vacuum and solution phase than hydrated mono-nitrate complex as well as completely solvated $UO_2(H_2O)_5^{2+}$ ions with counter-ions far from the central ion. For uranyl mono-nitrate complex, monodentate mode is preferred than bidentate mode for mono-nitrate complex in solution phase. In case of PuO_2^{2+}, both monodentate and bidentate are equally favored for mono-nitrate complex in solution phase. We observed that nitrates are very strongly bonded to Pu(IV) ion and they do not dissociate easily and prefer to stay in first coordination shell. Unlike nitrates, chlorides are weakly bonded to Pu(IV) ions. Pu(IV)

ions although have a greater affinity for chlorides than Th(IV) ions in solution. The coordination number for aquo-chloro complexes of Pu(IV) is found to be 8 with three chlorides present in the first shell. In case of Pu(VI) chlorides, PuO_2^{2+} retain five-fold coordination number with two chlorides replacing two water molecules bonded to Pu(VI) ion. The coordination number for chloro-aquo complexes of Th(IV) ($N_w + N_{Cl}$) is found to be 9–10, and one chloride enters the first coordination shell at 2.8 Å forming an inner sphere complex. The NBO analysis performed on actinide complexes reveals formation of covalent bonds between actinide ion and water as well as counter-ions present, but with high ionic character.

Both $UO_2^{2+}$and PuO_2^{2+} ions show coordination number of 4–5 with counter-ions replacing one or two water molecules from the first coordination shell. On the other hand, Pu^{4+}, has a coordination number of 8 both when completely solvated and also in the presence of chloride and nitrate ions with counter-ions replacing water molecules in the first shell. Nitrates were found to bind more strongly to Pu(IV) than chloride anions. In case of Th(IV) ion, the coordination number was found to be 9 or 10 in the presence of chlorides. Moreover, Pu(IV) ion shows greater affinity for chlorides than Th(IV) ion.

CHAPTER IV

DETECTION OF U/PU COMPLEXES USING GRAPHENE-BASED NANOSENSOR*

Uranium and Plutonium ions and their complexes play an important role in nuclear fuel reprocessing, and their trace characterization is important in nuclear forensics. In this chapter, we apply ab initio density functional theory calculations to design a graphene based fissile sensor in order to examine its applicability for detection of U and Pu complexes. We find that graphene needs to be functionalized to act as an effective sensor for detection of these radionuclides. Our calculations show that characteristic changes in the molecular electrostatic potential and current-voltage characteristics in finite-sized oxidized graphene-based nanojunctions can be used as strong signatures of the sorption of uranium and plutonium moieties.

4.1 Introduction

Groundwater contamination near nuclear fuel processing facilities due to accidental leakage is a major concern for the environment and human life in the surrounding areas. Preemptive actions in terms of detection and sensing are needs of the hour before any unforeseen disaster such as the Fukushima-Daiichi accident creates catastrophic damage to our ecosystem.

We review in this chapter our *ab initio* density functional theory calculations of U and Pu complexes with graphene and graphene oxide in order to examine the applicability of a graphene-based fissile sensor. Changes in the molecular electrostatic potential due to presence of a foreign moiety near graphene or GO can be transduced and amplified into current-voltage characteristics at nanoscale. By comparing the change in current due to presence of U or Pu complexes near a graphene and graphene oxide, we should be able to detect trace amounts of these radionuclides. The plasmonic features of nanosized graphene sheets (or graphene oxides) are strongly coupled to their electrical, magnetic, vibronic, and optical characteristics, and are significantly affected by presence of other molecules (such as nuclear agents) that may attach to its surface. Theoretical simulations in the past have shown the possible application of graphene-based devices to identify single molecules with high selectivity.[36,79]

4.2 Methodology

The Hamiltonian and overlap matrices required for current-voltage calculations as explained in detailed in Chapter III are obtained from optimized molecular structures of interest using the hybrid functional B3PW91.[59-60] This functional utilizes Becke exchange[61] with some component of Hartree-Fock[62-64] and the correlation functional of Perdew-Wang[65-69], and has been used successfully in a variety of applications involving molecular electronics devices[70-71]. Stuttgart effective core potential and associated basis set (ECP60MWB_SEG) are used for plutonium and uranium[86-87], with ECP parameters based on a quasi-relativistic level of theory.[86-87] The LANL2DZ basis set and effective

core potentials are used for gold atoms and include some relativistic effects.[107-109] For other atoms present in the system, 6–31G(d) basis set is used.[88] The Stuttgart small-core scalar relativistic effective core potentials (also referred as RECP) provide good agreement with experimental results with reasonable resources and therefore have been used widely to study structure of uranium and plutonium complexes. Successful comparison with experiment for Pu were reported (experimental values inside parentheses) for the ionization potentials 5.69–5.74 eV (6.03 eV);[86-87] and for geometry of several plutonium complexes, e.g., $PuO_2(H_2O)_5^{2+}$: Pu–O = 1.72 Å (1.74 Å) and Pu–O_w = 2.44 Å (2.41 Å); $PuO_2(NO_3)_2(H_2O)_2$: Pu–O = 1.74 Å (1.73 Å), Pu–O_w = 2.53 Å (2.43 Å), and Pu–O_N = 2.46Å (2.50 Å); $PuO_2(Cl)_2(H_2O)_3$: Pu–O = 1.73 Å (1.75 Å), Pu–O_w = 2.53 Å (2.49 Å), and Pu–Cl = 2.67 Å (2.70 Å); $Pu(H_2O)_8^{4+}$: Pu–O_w = 2.39 Å (2.39 Å).[17] Stuttgart ECP as implemented in Gaussian 09 has also been used to study hydration and oxidation study of plutonyl ion in gas phase.[110]

All of the DFT calculations are performed with the program GAUSSIAN-09[90] with convergence threshold for self-consistent cycle (SCF) set as 10^{-6} for density matrix and 10^{-8} for root-mean-square and maximum density matrix error respectively. Geometry optimizations are carried out with the Berny method[91-92]. The effect of the neighbor contact atoms to the molecule is directly considered in the discrete ab initio calculations by using an extended molecule which consists of single gold atom directly bonded to the molecule at both ends (Au–M–Au). Once we obtain optimized structure, single point energy calculations are performed at each bias voltage to account for charge transfer between molecule and the contact atoms as well as any reorganization of

electronic structure. The Hamiltonian and the overlap matrices are then extracted for each applied voltage. These two gold atoms (nano-contacts) are then assumed to be connected to a continuous electronic state of gold clusters connected to an external potential difference and acts as the source of electrons. The role of nano-contacts (individual gold atoms at each end) is to produce an adequate geometry and retain the interface chemistry in the neighborhood of the atoms attached to the gold contact. As a result, the pathway of electrons is through this minimum junction setting which is retained for all cases for the I-V characteristics. In case of more practical sensors, more than one gold atom will be attached to graphene sheets yielding larger currents. Although the scalability can be nonlinear, the idea behind using single gold atom contact for the molecule-electrode interface is to design smallest possible sensor. The Hamiltonian and overlap matrices obtained from density functional are then used by an in house GENIP[41,49,111] program which applies Green's functions theories for calculating the current-voltage relationship as described in detail in Chapter III. The GENIP program was tested successfully for small molecules like thioalkanes.[111]

4.3 Results and Discussion

The first ionization potential of plutonium using B3PW91/ECP60MWB_SEG is estimated as 5.72 eV (expt. value 6.03 eV);[112] however, it falls nicely in the range 5.69–5.74 eV obtained with the same basis-set but with state-averaged CASSCF with subsequent multi-reference averaged coupled-pair functional calculations[86-87] thus validating our chosen level of theory and basis-set. Furthermore, in order to confirm that

the chosen level of theory correctly identifies lowest energy spin-state, two or more spin states are considered for each of the bare ions, Pu^{4+}, PuO_2^{+}, PuO_2^{2+} studied here (Table 4.1). The lowest spin-state of the Pu^{4+} is found to be quintet, PuO_2^{+} quartet, PuO_2^{2+} triplet and UO_2^{2+} singlet, similar to those reported in previous work.[10]

Table 4.1. Properties of several spin states of Pu^{4+}, PuO_2^{2+}, and PuO_2^{1+} ions

Complex	m	Pu–O	q(Pu)	q(O)	Energy
Pu^{4+}	1		4		−551.04015
Pu^{4+}	3		4		−551.14892
Pu^{4+}	5		4		−551.19622
Pu^{4+}	7		4		−550.63525
Pu^{4+}	9		4		−550.07474
PuO_2^{2+}	1	1.654	2.15	−0.08	−703.61595
PuO_2^{2+}	3	1.656	2.15	−0.08	−703.65683
PuO_2^{2+}	5	1.711	2.19	−0.09	−703.63662
PuO_2^{1+}	2	1.690	1.56	−0.28	−704.21144
PuO_2^{1+}	4	1.707	1.59	−0.29	−704.28787
PuO_2^{1+}	6	1.761	1.64	−0.32	−704.20830

The lowest-energy spin-state for successive hydrates of the bare ions AnO_2^{z+} (z = 1,2) An being U, Np or Pu, are found to be same as that of bare ion as reported in literature.[110] We also used several multiplicities for other complexes in order to confirm that addition of other components does not alter the lowest spin state of bare ion (Table 2). In all cases, it is found that the lowest energy spin state of the complex is the same as that of the corresponding bare ion.

Table 4.2. Calculated properties of several plutonium complexes: q = complex net charge, m = multiplicity, Pu–O distance, Pu–O_w distance, q(A) = partial charge in atom A, and total energy

Complex	q	m	Pu–O	Pu–O_w	q(Pu)	q(O)	q(O_w)	q(H_w)	Energy
$PuO_2^{2+}(H_2O)_5$	2	1	1.695	2.438	1.59	−0.26	−0.83	0.51	−1085.95722
$PuO_2^{2+}(H_2O)_5$	2	3	1.698	2.441	1.59	−0.27	−0.83	0.51	−1085.99667
$PuO_2(NO_3)_2(H_2O)_2$	0	1	1.712	2.520	1.41	–0.33	–0.79	0.47	–1417.77320
$PuO_2(NO_3)_2(H_2O)_2$	0	3	1.716	2.510	1.42	−0.34	−0.80	0.48	−1417.81304
cis-$PuO_2(Cl)_2(H_2O)_2$	0	1	1.72	2.492	0.94	−0.34	−0.79	0.49	−1777.69323
cis-$PuO_2(Cl)_2(H_2O)_2$	0	3	1.72	2.488	0.96	−0.34	−0.79	0.49	−1777.72976
trans-$PuO_2(Cl)_2(H_2O)_2$	0	1	1.72	2.465	1.02	−0.34	−0.79	0.48	−1777.69659
trans-$PuO_2(Cl)_2(H_2O)_2$	0	3	1.72	2.464	1.03	−0.34	−0.79	0.48	−1777.73405
cis-$PuO_2(Cl)_2(H_2O)_3$	0	1	1.72	2.587	0.95	−0.34	−0.80	0.47	−1854.09703
cis-$PuO_2(Cl)_2(H_2O)_3$	0	3	1.72	2.582	0.97	−0.34	−0.80	0.47	−1854.13428
trans-$PuO_2(Cl)_2(H_2O)_3$	0	1	1.71	2.523	1.03	−0.33	−0.79	0.47	−1854.10337
trans-$PuO_2(Cl)_2(H_2O)_3$	0	3	1.72	2.523	1.04	−0.33	−0.79	0.47	−1854.14221

4.3.1 Geometry Optimization

Once ground state multiplicities are confirmed, geometry of some common U and Pu complexes present in nuclear waste water were optimized, the results of which are shown in Figure 4.1–4.2 followed by frequency calculations. All the geometries are fully optimized at B3PW91//ECP60MWB_SEG/6-31G(d) level of theory. The bond lengths, energy and Mulliken charges for several U and Pu complexes are listed in Table 4.3–4.4.

Table 4.3. Calculated bond distance, atomic Mulliken charges, and energies of AnO_2^{z+} (z = 1, 2; An = U, Pu) complexes

Complex	q	m	An–O	An–O_w	q(An)	q(O)	q(O_w)	q(H_w)	Energy
PuO_2^{2+}	2	3	1.656		2.15	−0.08	NA	NA	−703.65683
$PuO_2(H_2O)_2^{2+}$	2	3	1.696	2.373	1.66	−0.25	−0.83	0.52	−1009.57653
$PuO_2(H_2O)_5^{2+}$	2	3	1.698	2.441	1.59	−0.27	−0.83	0.51	−1085.99667
$PuO_2(H_2O)_6^{2+}$	2	3	1.701	2.432†	1.56	−0.28	−0.83	0.51	−1162.42399
$PuO_2(NO_3)_2(H_2O)_2$	0	3	1.716	2.510	1.42	−0.34	−0.80	0.48	−1417.81304
PuO_2^{1+}	1	4	1.707		1.59	−0.29			−704.28787
$PuO_2(H_2O)^{1+}$	1	4	1.719	2.403	1.48	−0.33	−0.83	0.51	−780.73266
$PuO_2(H_2O)_2^{1+}$	1	4	1.731	2.452	1.41	−0.36	−0.83	0.50	−857.16925
$PuO_2(H_2O)_3^{1+}$	1	4	1.743	2.456	1.32	−0.39	−0.82	0.49	−933.60248
$PuO_2(H_2O)_4^{1+}$	1	4	1.752	2.498	1.27	−0.41	−0.82	0.48	−1010.01966
$PuO_2(H_2O)_5^{1+}$	1	4	1.757	2.568	1.17	−0.42	−0.82	0.47	−1086.42230
cis-$PuO_2(Cl)_2(H_2O)_2$	0	3	1.72	2.488	0.96	−0.34	−0.79	0.49	−1777.72976
trans-$PuO_2(Cl)_2(H_2O)_2$	0	3	1.72	2.464	1.03	−0.34	−0.79	0.48	−1777.73405
cis-$PuO_2(Cl)_2(H_2O)_3$	0	3	1.72	2.582	0.97	−0.34	−0.80	0.47	−1854.13428
trans-$PuO_2(Cl)_2(H_2O)_3$	0	3	1.72	2.523	1.04	−0.33	−0.79	0.47	−1854.14221
$UO_2(NO_3)_2(H_2O)_2$	0	1	1.755	2.527	1.66	–0.39	–0.81	0.48	–1340.93304
$UO_2(NO_3)_2(H_2O)_3$	0	1	1.755	2.526	1.54	–0.39	–0.82	0.48	–1417.32142

†PuO_2^{2+} can accommodate only 5 water molecules in first shell, the sixth water molecule starts forming second shell (at 4.133 Å) around the PuO_2^{2+} ion.

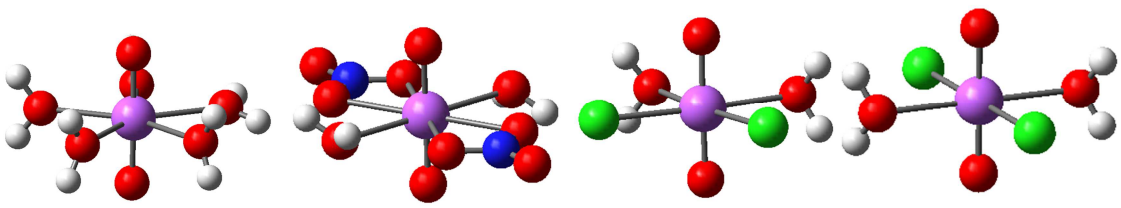

$PuO_2(H_2O)_5^{2+}$ $PuO_2(NO_3)_2(H_2O)_2$ *cis*-$PuO_2Cl_2(H_2O)_2$ *trans*-$PuO_2Cl_2(H_2O)_2$

Figure 4.1. Optimized structures of common PuO_2^{2+} and UO_2^{2+} moieties in nuclear waste water

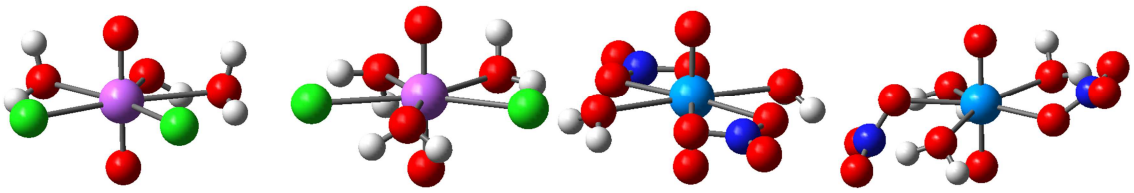

cis-$PuO_2Cl_2(H_2O)_3$ *trans*-$PuO_2Cl_2(H_2O)_3$ $UO_2(NO_3)_2(H_2O)_2$ $UO_2(NO_3)_2(H_2O)_3$

Figure 4.1 Continued.

Table 4.4. Calculated bond distance and atomic Mulliken charges of common Pu(IV) complexes

Complex	q	m	Pu–O_w	Pu–X (X=Cl/O_N)	q(Pu)	q(X)	q(O_w)	q(H_w)	Energy
$Pu(H_2O)_8^{4+}$	4	5	2.41	NA	2.09	NA	–0.85	0.54	–1163.68949
$Pu(NO_3)_2(H_2O)_2^{2+}$	2	5	2.394	2.246 3.906	1.96	–0.42 –0.17	–0.85	0.53	–1266.71432
$Pu(NO_3)_2(H_2O)_4^{2+}$	2	5	2.420	2.316 3.970	1.87	–0.45 –0.23	–0.84	0.52	–1419.61169
$Pu(NO_3)_4(H_2O)_3$	0	5	2.510	NA	1.73	–0.44	–0.82	0.48	–1904.26732
$PuCl_2(H_2O)_6^{2+}$	2	5	2.467	2.512	1.18	–0.16	–0.83	0.51	–1932.38799
$PuCl_4(H_2O)_4$	0	5	2.545 4.216	2.391 2.575	1.01	–0.28 –0.60	–0.82	0.47	–2700.52621

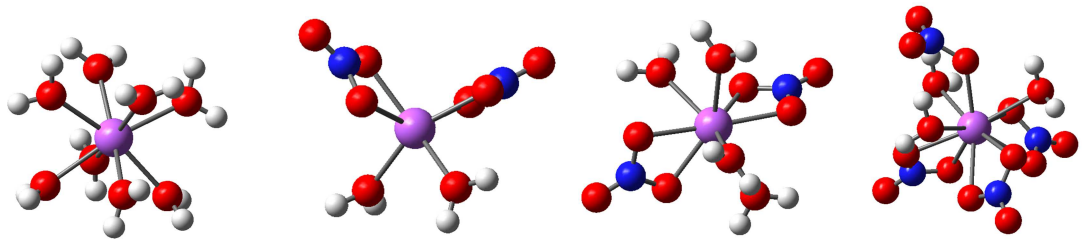

$Pu(H_2O)_8^{4+}$ $Pu(NO_3)_4(H_2O)_3$ $Pu(NO_3)_2(H_2O)_2^{2+}$ $Pu(NO_3)_2(H_2O)_2^{2+}$

Figure 4.2. Optimized structures of common Pu(IV) complexes present in nuclear waste water

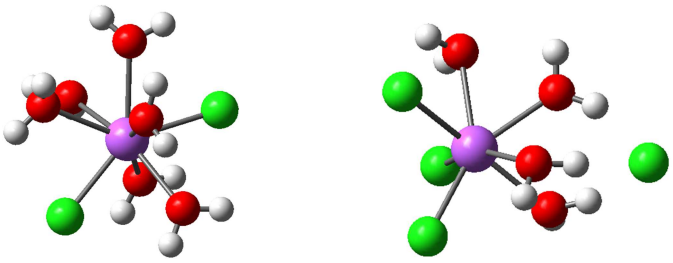

$PuCl_2(H_2O)_6^{2+}$ $PuCl_4(H_2O)_4$

Figure 4.2 Continued

When these uranyl or plutonyl complexes interact with a graphene molecule (Figure 4.3), the Pu–O and U–O bond lengths increase, thus indicating weakening of these bonds due to interactions of the actinide ions with graphene. Table 4.5 lists the bond distances of some U/Pu complexes for comparison purposes.

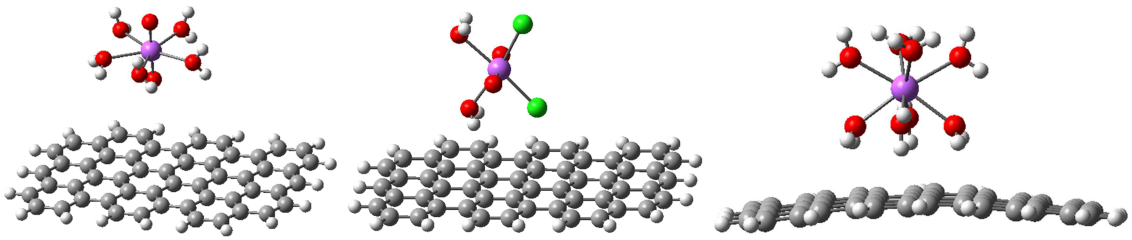

$PuCl_2(H_2O)_6^{2+}$ on G $PuO_2Cl_2(H_2O)_2$ on G $Pu(H_2O)_8^{4+}$ on G

Figure 4.3. Optimized geometries of some common U and Pu moieties adsorbed on a graphene (G) molecule

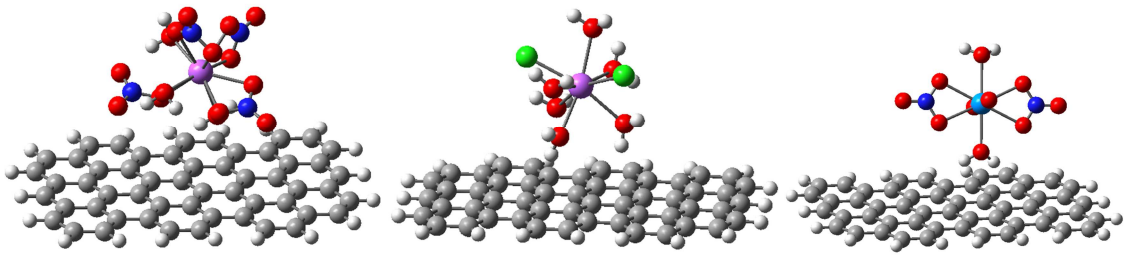

$Pu(NO_3)_4(H_2O)_3$ on G $PuCl_2(H_2O)_6^{2+}$ on G $Pu(NO_3)_4(H_2O)_3$ on G

Figure 4.3 Continued.

Table 4.5. Calculated bond distances, atomic Mulliken charges, and energies of Pu complexes adsorbed on graphene

Complex	Pu–O	Pu–O_w	Pu–X X=Cl,O_N	q(Pu)	q(O)	q(X)	q(O_w)	Energy
$PuO_2(H_2O)_5^{2+}$	1.757	2.564		1.16	–0.42	NA	–0.81	–3155.46987
cis-$PuO_2Cl_2(H_2O)_2$	1.739	2.543	2.632	0.96	–0.38	–0.44	–0.79	–3847.03326
$Pu(H_2O)_8^{4+}$		2.513		1.59			–0.86	–3233.42383
$Pu(NO_3)_2(H_2O)_2^{2+}$		2.458	2.358 3.999	1.59		–0.48 –0.30	–0.86	–3336.23895
$Pu(NO_3)_2(H_2O)_4^{2+}$		2.512	2.427 4.071	1.50		–0.49 –0.33	–0.84	–3489.08394
$Pu(NO_3)_4(H_2O)_3$		2.526	2.874 3.323	1.65		–0.45	–0.83	–3973.56671
$PuCl_2(H_2O)_6^{2+}$		2.551	2.672	0.93		–0.43	–0.83	–4001.83962

4.3.2 Molecular Electrostatic Potential

The graphene plasmons (π-electrons) are highly sensitive and significantly affected by the electrostatic field of a single molecule adsorbed on its surface. Indeed, a change in the molecular electrostatic potential (MEP) of graphene can be observed when

interacting with the Pu and U complexes. The molecular electrostatic potential (MEP) of graphene and some U/Pu complexes obtained from DFT calculations are plotted on their electron density as shown in Figure 4.4. The figure also reflects changes in MEP of graphene when U/Pu complexes are adsorbed on its surface which can be used as a signature for detection of these radionuclides. The magnitude of the potentials is shown by the solid surface colors. Blue is the most positive potential and red is the most negative. All complexes are shown at the same color scale (bottom of Figure 4.3). However, a potential challenge for the detection is that some waters are closer to graphene than are Pu or U, indicating the need for graphene functionalization to enhance sensitivity. All calculations have been done at B3PW91 level using Stuttgart ECP for U and Pu and the 6-31G(d) for other atoms.

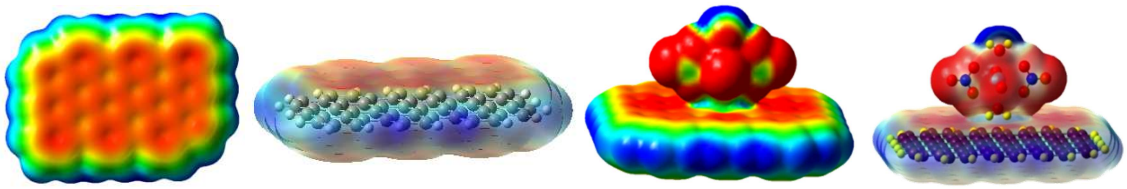

$C_{54}H_{20}$ graphene $UO_2(NO_3)_2(H_2O)_2$ on graphene

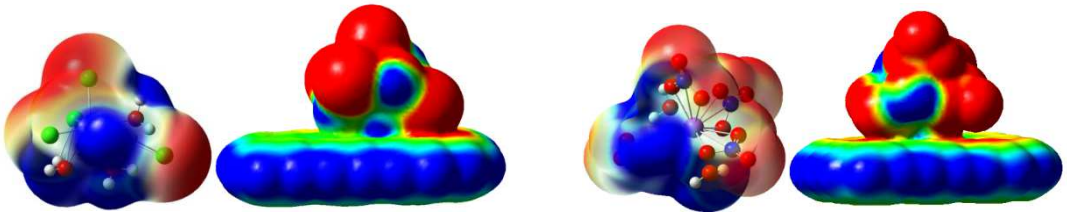

$PuCl_4(H_2O)_4$ $PuCl_2(H_2O)_4$ on graphene $Pu(NO_3)_4(H_2O)_3$ $Pu(NO_3)_4(H_2O)_3$ on G

Figure 4.4. MEPs of U and Pu complexes adsorbed on graphene

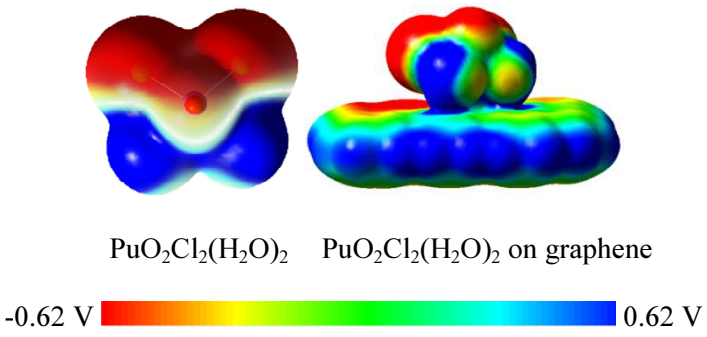

Figure 4.4 Continued.

GO contains random arrangement of functional groups and large structural disorder in the carbon skeleton as a result of partial oxidation. Common functional groups reported on oxidation of graphene are -COOH, -OH, -C=O at edges and C-O-C and –OH on the basal plane.[26-27,113-114] We studied the interaction of plutonium complex with graphene oxide (GO) using several functional groups as mentioned earlier. In this study, we present results for (i) a graphene oxide with two –OH and one –O– functional groups present or type I (Figure 4.5a), (ii) a graphene oxide containing a carbonyl functional group or type II (Figure 4.5b), and (iii) a graphene oxide with a –COOH group (type III). The introduction of –CO group on graphene oxide surface leads to breaking of few bonds and hence those C atoms are saturated with H atoms to satisfy the valence of carbon atoms. The hydrated form of plutonium nitrate was chosen for study due to the fact that nitrates form very strong bonds with Pu(IV) ion and hence a real comparison can be made with respect to its interaction with graphene oxide. In case of type I graphene oxide (Figure 4.5a), water molecules still remain closest to the GO nanosheet as observed for

interaction of plutonium complex with just graphene nanosheet.The molecular orbitals HOMO and LUMO, mainly responsible for electron transport remain unaffected by presence of Pu(IV) complex thus indicating weak interaction between –OH/ –O– and Pu(IV) complex. However, when GO with carbonyl group (type II) was tested, we observed rearrangement of nitrates around Pu(IV) ion in order to accommodate carbonyl group (Figure 4.5b). –CO group is known to form strong co-ordination complexes with d-block elements. The molecular electrostatic potential when plotted on electron density also shows strong changes as can be seen in Figure 4.4c.

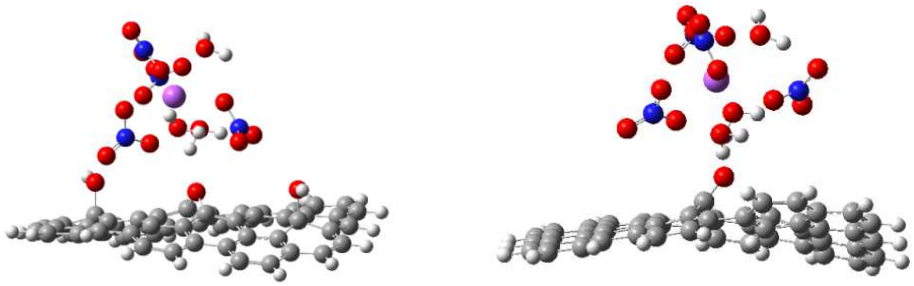

(a) $Pu(NO_3)_4(H_2O)_3$ adsorbed on GO (type I) (b) $Pu(NO_3)_4(H_2O)_3$ adsorbed on GO (type II)

Figure 4.5. Optimized geometry of nitrato-aquo-complex of Pu(IV) adsorbed on GO (type I) and GO (type II) and their corresponding molecular electrostatic potential (MEP).

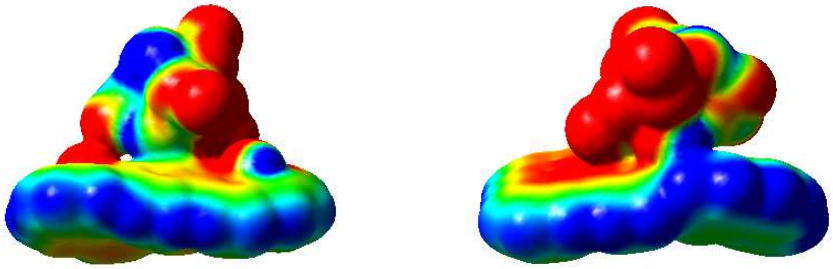

(c) MEP of $Pu(NO_3)_4(H_2O)_3$ on type I GO (d) MEP of $Pu(NO_3)_4(H_2O)_3$ on type II GO

-0.62 V 0.62 V

Figure 4.5 Continued.

4.3.3 Molecular Orbital Diagram

The change in current-voltage characteristics of the molecular junction is coupled to the change in molecular orbitals involved in electron transport at low bias voltages. A high conductance is obtained if the molecular orbital (MO) covers the entire molecule (delocalized) as there are high probabilities of electron transport at energies similar to the one of the MO. On the contrary, if the MOs are localized in certain region, this gives rise to high impedance. The MOs in the vicinity of highest occupied molecular orbital (HOMO) and lowest unoccupied molecular orbital (LUMO) for graphene/ graphene oxide nanosheets with and without $Pu(NO_3)_4(H_2O)$ complex adsorbed on its surface are presented in Figure 4.6a–f. The approaching plutonium nitrate complex causes localization of HOMO and LUMO indicating strong interaction (Figure 4.6), and thus significantly reduces the current as will be discussed in later sections.

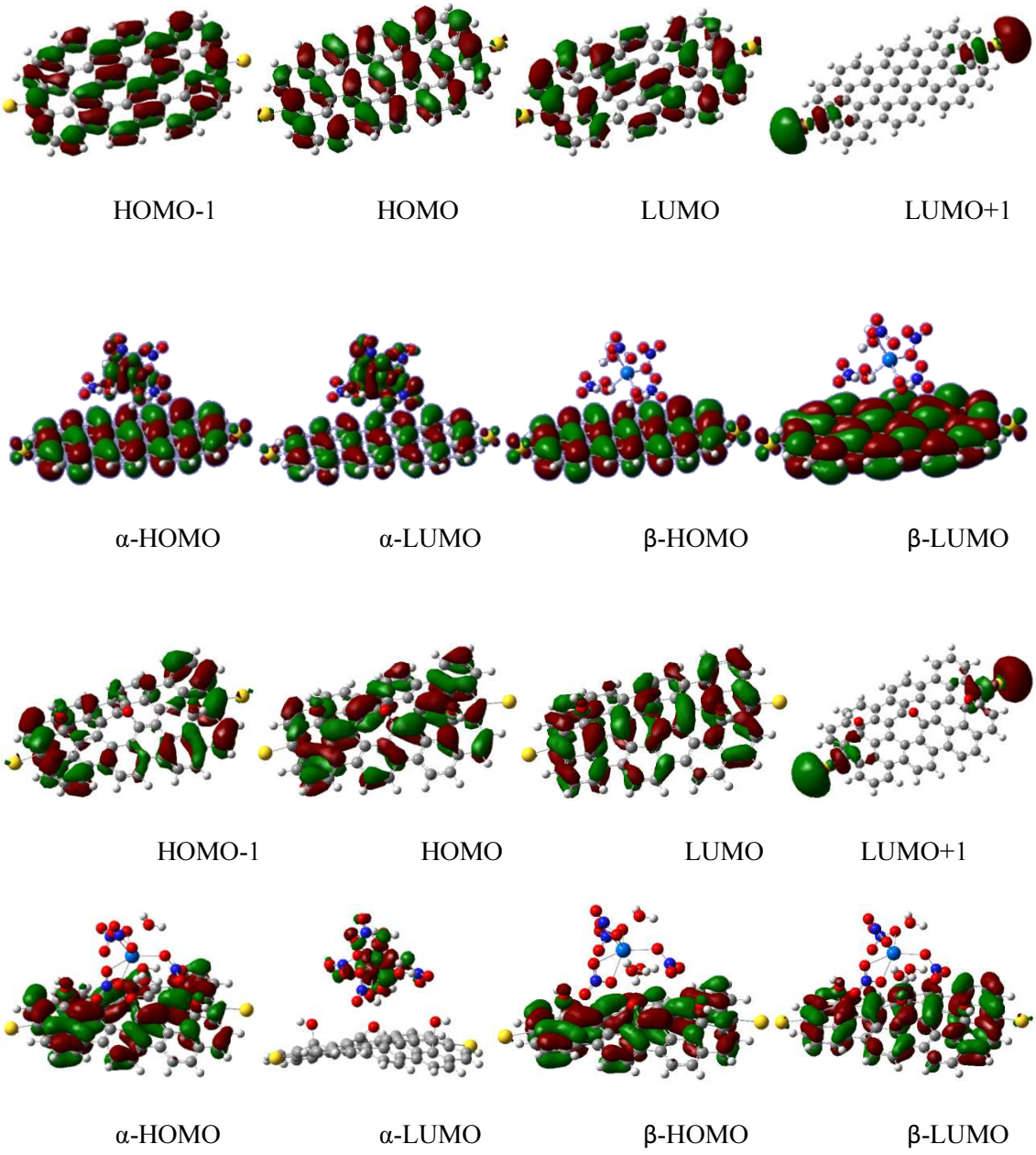

Figure 4.6. Molecular orbital diagrams of (a) graphene nanosheet, (b) $Pu(NO_3)_4(H_2O)_3$ adsorbed on graphene, (c) graphene oxide GO (type I), (d) $Pu(NO_3)_4(H_2O)_3$ adsorbed on GO (type I), (e) graphene oxide GO (type II), (f) $Pu(NO_3)_4(H_2O)_3$ adsorbed on GO (type II).

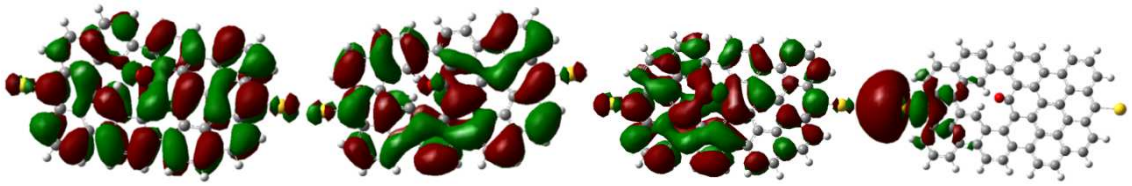

HOMO-1 HOMO LUMO LUMO+1

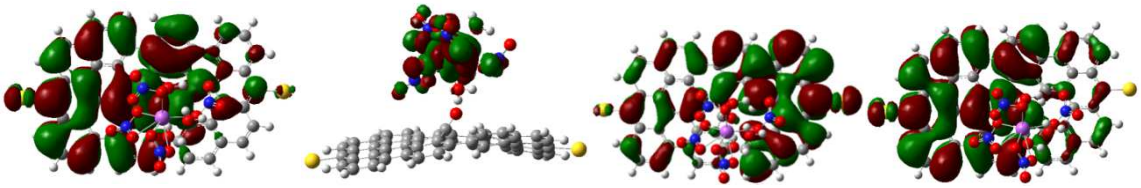

α-HOMO α-LUMO β-HOMO β-LUMO

Figure 4.6 Continued

4.3.4 Current-Voltage Characteristics

The current-voltage characteristics are obtained through Au-molecule-Au junctions using GENIP program. As explained earlier, the geometries of the molecular junctions Au-molecule-Au are first fully optimized using the Gaussian program and their Hamiltonians and overlap matrices are evaluated in presence of the applied external fields. The DOS of the bulk gold contacts is calculated using the Crystal-06 program[115] using periodic boundary conditions.

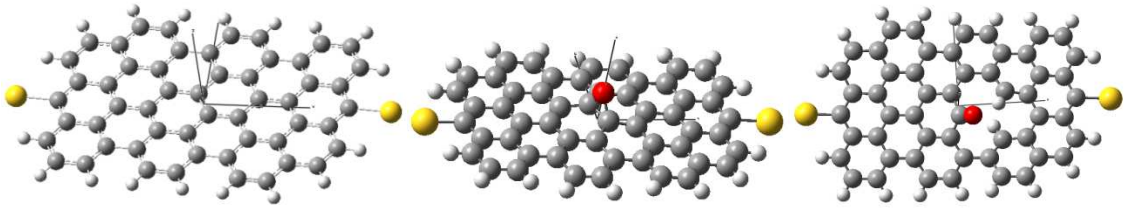

(a) Au-graphene-Au (b) Au-GO(with a –O–)-Au (c) Au-GO(with a –CO)-Au

Figure 4.7. Optimized structures of graphene/ graphene oxide junctions to be used as sensing molecule

The current-voltage curves for above three junctions (Figure 4.7a–c) are presented below in Figure 4.8. As indicated earlier, graphene needs to be functionalized to act as an effective sensor for detection of fissile materials such as uranium and plutonium complexes. The covalent functionalization can have significant effect on electronic properties. The conductance of graphene –O– group causes transformation of sp^2 hybridized C atoms to sp^3 hybridization. This causes conductance to reduce from 0.67 μAV^{-1} (for graphene) to 0.035 μAV^{-1}. The conductance decreases exponentially with further addition of –O– group. However, addition of –CO group preserves sp^3 hybridization of C atoms and conductance in this case is found to increase from 0.67 μAV^{-1} to 9.5 μAV^{-1}.

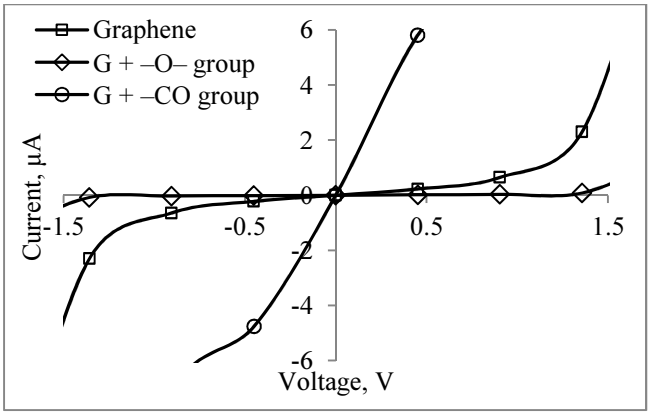

Figure 4.8. Current-voltage curves for graphene/ graphene oxide junctions

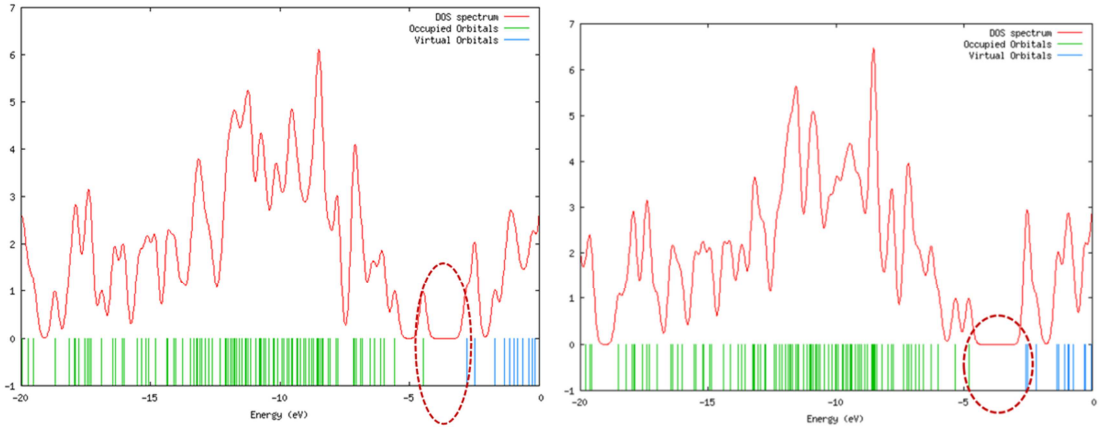

(a) (b)

Figure 4.9. Density of states plot for a) DOS of Au-graphene-Au, (b) Au-GO(with a –O–)-Au, and (c) Au-GO(with a –CO)-Au

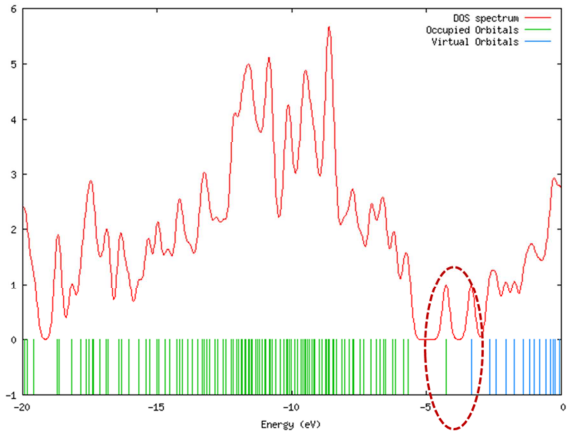

(c)

Figure 4.9 Continued.

The conductance obtained depends mainly on the energies of the orbitals in the neighborhood of the frontier molecular orbitals HOMO and LUMO) of the molecular junction as well as on the Fermi level of the gold electrodes and their coupling to the graphene complex. The density of states (DOS) plots for three cases shown in Figure 9a–c are obtained using GaussSum program[116]. The HOMO-LUMO gap appears to be widened by adding –O– group while it is significantly reduced when –CO group is present which explains the trend observed in conductance values.

We also tried to compare our calculated results to those obtained using experiments. We find similar trend as reported in literature for electrical conductivities comparing graphene and graphene oxide.[117] The minimum sheet resistance for graphene is reported as 6.45 kΩ/sq using experiments.[54] "Based on lateral dimensions and calculated current-voltage characteristics, the sheet resistance is found to be ~ 1150

kΩ/sq for our case, which is consistent with the fact that resistance increases with decrease in number of channels for electron transport and we consider a single point of contact; thus comparing to experiment, a 200 points-contact or ~60 nm electrode would yield the same resistance sheet." [118]

The optimized geometries of the molecular junctions Au–graphene+U/Pu–Au used to generate current-voltage curves are presented below in Figure 4.10. All the geometries were optimized at B3PW91 level using ECP60MWB_SEG/6-31G(d) basis-sets. Following optimization, single point calculations were performed at each bias voltage to extract Hamiltonian and overlap matrices.

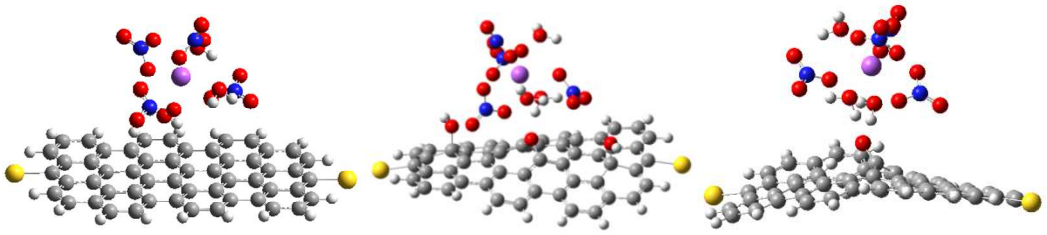

Graphene + $Pu(NO_3)_4(H_2O)_3$ GO(I) + $Pu(NO_3)_4(H_2O)_3$ GO(II) + $Pu(NO_3)_4(H_2O)_3$

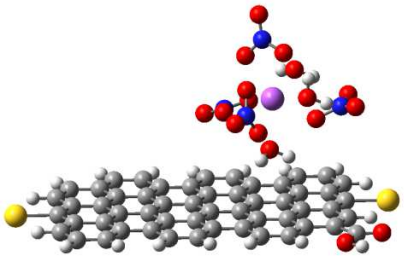

GO(III) + $Pu(NO_3)_4(H_2O)_3$

Figure 4.10. Au-molecule-Au junctions used for generation of I-V characteristics

The resulting current-voltage characteristics are shown in Figure 4.11. As indicated earlier, since we did not observe appreciable change in pi-pi orbitals on graphene surface in the presence of Pu^{4+} complex, the same is reflected in the I-V characteristics with and without plutonium complex adsorbed on a graphene sheet (Figure 4.11a) or GO of type I (Figure 4.11b). However, a significant reduction in current values is observed in the presence of plutonium complex for type II GO (Figure 11c). The change in average conductance in the linear region is presented in Table 4.6.

Table 4.6. Average conductance of graphene/graphene oxide before and after exposure to $Pu(NO_3)_4(H_2O)_3$ complex

Sensing molecule	Avg. conductance before exposure (μAV^{-1})	Avg. conductance after exposure (μAV^{-1})
Graphene	0.67	0.93
GO (type I)	0.007	0.006
GO (type II)	9.5	1.6
GO (type III)	0.70	0.97

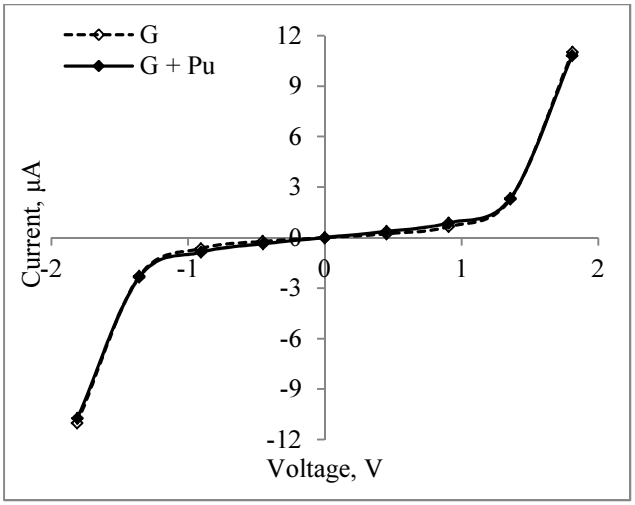

(a)

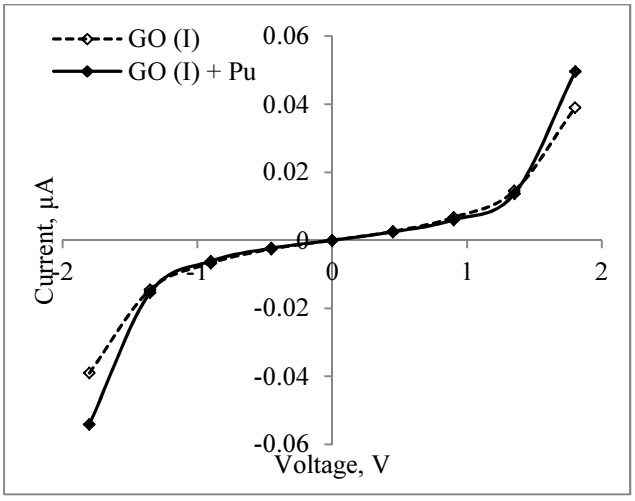

(b)

Figure 4.11. Current-Voltage characteristics of Pu(IV) complex adsorbed on Graphene/ Graphene Oxide: (a) $Pu(NO_3)_4(H_2O)_3$ on graphene, (b) $Pu(NO_3)_4(H_2O)_3$ on GO (type I), (c) $Pu(NO_3)_4(H_2O)_3$ on GO (type II), and (d) $Pu(NO_3)_4(H_2O)_3$ on GO (type III).

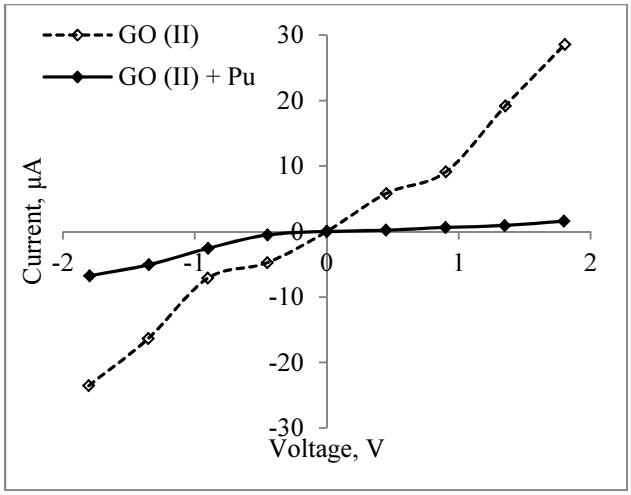

(c)

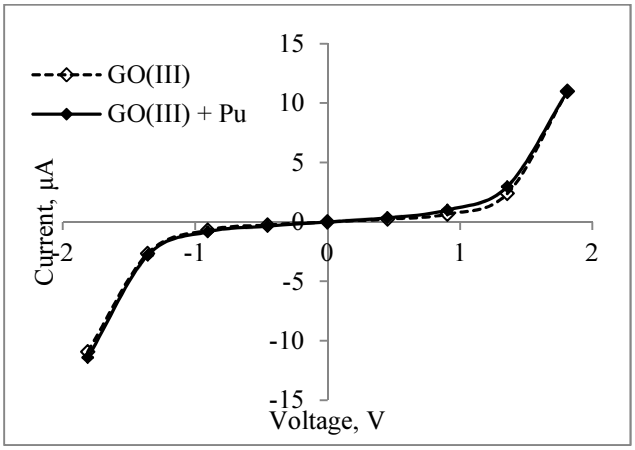

(d)

Figure 4.11 Continued.

It is important here to explain the effect of pH in case of graphene oxide with –COOH functional group (GO type III), referred to GCOOH in following sections. GCOOH can lose H^+ ions forming GCOO- ion at low pH. The calculated conductance changes from 0.705 μAV^{-1} to 1.634 μAV^{-1}. When this anionic form interacts with Pu(IV)

nitrate complex, the conductance reduces to 0.903 μAV^{-1} (see Figure 4.12). Therefore, pH can have strong effects in case of GO (type III) based molecular junctions.

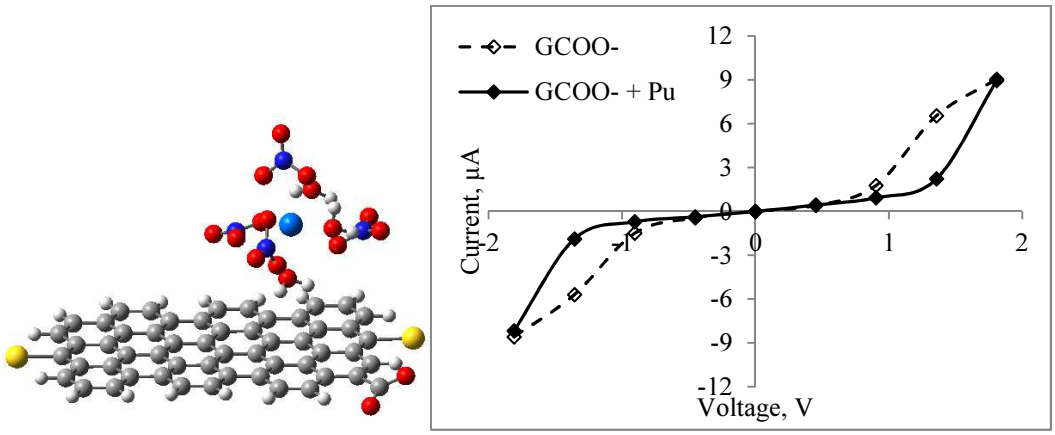

Figure 4.12. Optimized structure and current-voltage curve of $Pu(NO_3)_4(H_2O)_3$ complex exposed to anionic form of GO(type III)

The current-voltage for uranium nitrate complex with graphene and graphene oxide are also calculated using similar principles and are shown in Figure 4.13. As in the case of $Pu(NO_3)_4(H_2O)_3$ complex, GO with –CO group (type II) appears as more affective sensing material than graphene for UO_2^{2+} complexes as well. The average conductance of graphene in linear region of I-V curve changes marginally from 0.67 μAV^{-1} to 0.59 μAV^{-1} on exposure to $UO_2(NO_3)_2(H_2O)_2$ complex. But in case of GO (type II), the average conductance changes significantly from 9.5 μAV^{-1} to 6.3 μAV^{-1} on exposure to UO_2^{2+} complex.

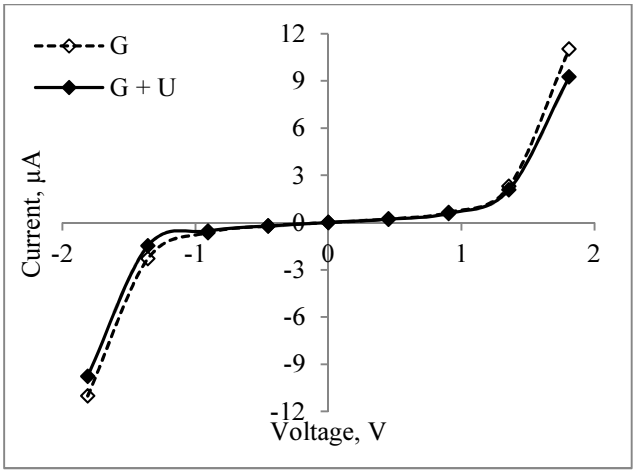

(a)

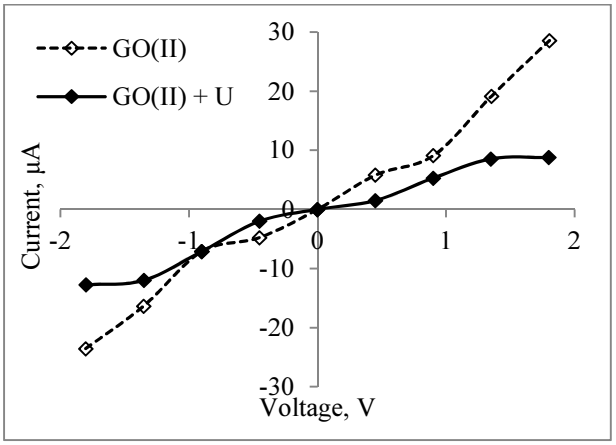

(b)

Figure 4.13. Current-Voltage characteristics of UO_2^{2+} complex adsorbed on Graphene/ Graphene Oxide: (a) $UO_2(NO_3)_2(H_2O)_2$ on graphene, and (b) $UO_2(NO_3)_2(H_2O)_2$ on GO (type II)

In addition to nitrate complexes, we also obtain current-voltage curves for chloro-complexes of Pu(IV) and Pu(VI) ions when adsorbed on graphene. The results are shown in Figure 4.14. A noticeable change in the electrical conductance of graphene junction can be observed which was absent in case of nitrate molecules. The average

conductance of graphene changes significantly from 0.67 μAV^{-1} to 2.23 μAV^{-1} on exposure to *cis*-$PuO_2Cl_2(H_2O)_2$ complex, while it creases to 2.28 on exposure to $PuCl_4(H_2O)_4$ complex. Unlike nitrates, the chloride ions are weakly bonded to the central cation and hence expose the Pu(IV) and Pu(VI) ions exposed to graphene surface. The positive charge of the central cation is not completely shielded and hence charge transfer can take place between the actinide complexes and graphene. The effect of positively charges actinide complexes on electrical conductance of graphene will become more obvious in next chapter.

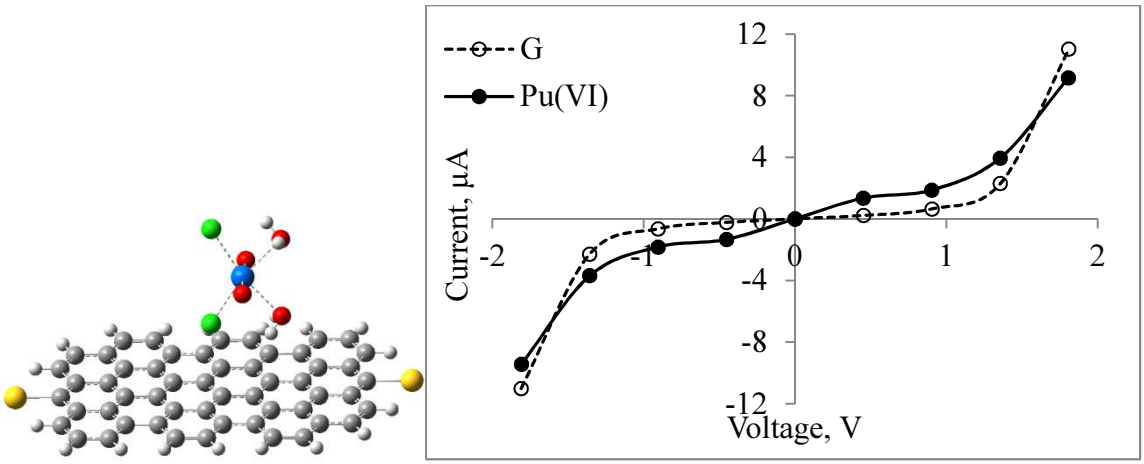

(a)

Figure 4.14. Optimized structure and current-voltage curves of (a) $PuO_2Cl_2(H_2O)_2$, and (b) $PuCl_4(H_2O)_4$ complexes adsorbed on graphene nanojunction

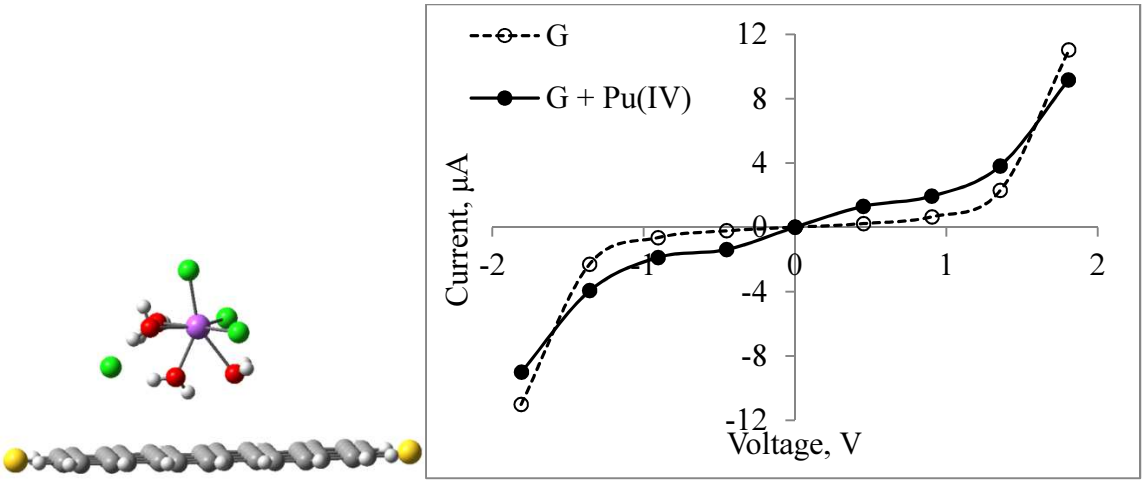

(b)

Figure 4.14 Continued

4.4 Conclusions

Our study indicated that B3PW91 functional along with Stuttgart effective core potential and associated basis-set ECP60MWB_SEG [87,89] yielded acceptable results when compared to very precise experimental data available.[37,119] Our calculations also show that An–O in actinyls and An–O_w (An – actinide) bond lengths are weakened on interaction with graphene. Our results show GO with –CO group as the most promising sensing material for detection of radionuclides.

CHAPTER V

ELECTRON TRANSPORT THROUGH GRAPHENE NANOSENSOR FOR DETECTION OF EUROPIUM*

In the last chapter, we showed that GO with a carbonyl functional group can be used to detect radionuclides in nuclear waste water by measuring the change in electrical conductance under an applied external voltage using a combined DFT-Green's function approach.[37-38]. In this chapter, we calculate the response of graphene-based nanosensor for Eu(III) complexes. Eu(III) complexes are safer and economical for experimentation and hence are best surrogates for studying electrochemical response of graphene-based fissile sensors.

5.1 Introduction

As indicated in earlier chapters, we need to identify the europium complexes prevalent in aqueous phase. Classical molecular dynamics simulation with explicit polarization showed that that europium nitrates are more likely to exist in monodentate form.[120] However, density functional theory (DFT) calculations performed on Eu(III) aquo-nitrate complexes showed that bidentate complex is more stable based on Gibbs free energy both in gas phase and aqueous phase.[121] However, the change in free energy was smaller in solution. Based on this information, we focus on the interaction of

* Reproduced in part with permission from N. Kumar and J.M. Seminario, J. Phys. Chem. C, Vol 119, Issue 21, Pages 12037–12046. Copyright 2015 American Chemical Society

europium nitrate complexes in bidentate mode for both dissociated as well as non-dissociated forms with graphene as they are more likely to be found in nuclear waste water. We also studied interaction of europium (III) oxide (Eu_2O_3) with graphene and graphene oxide. The electron transport calculations of europium oxide-graphene complex have important applications in the field of life sciences as luminescent bioprobes[122-123] and optoelectronics.[123] The residual oxygen functionalities present in reduced graphene oxide (RGO) are responsible for complexation of Eu(III) ions with RGO.[122] The electrical properties of Eu_2O_3-graphene nanocomposite was also recently reported experimentally[124] showing a linear reduction in electrical conductivity with increase in the Eu_2O_3 content.

5.2 Methodology

We use density functional theory[59-60] with the hybrid functional B3PW91[68-69,125-127]. B3PW91 functional has been used successfully in a variety of applications related to clusters of atoms,[128-131] molecular electronics devices,[132-133] and other metallic clusters.[134-140] For the gold LANL2DZ basis set and effective core potential[141-143] are used for the gold atoms while the Stuttgart effective core potential and associated basis set ECP28MWB_SEG[144-145] are used for europium. The 6-31G(d) basis set[146] is used for other remaining atoms. Geometry optimizations are carried out with the Berny method[147-148] and the optimized stable structures are confirmed local minima by performing frequency (second derivatives) calculations. All of the structure optimization and frequency calculations are performed with GAUSSIAN-09 program[90].

In order to obtain the I-V characteristics we use our in house GENIP program. The molecular junction consists of a graphene molecule (G) $C_{54}H_{20}$ terminated with gold atoms at opposite ends. The geometries of Au–graphene–Au molecular junctions are also fully optimized. The gold atoms are further assumed to be connected to two semi-infinite gold electrodes to which an external voltage is applied. The current-voltage through the molecular junction is calculated using a DFT-Green's function approach as discussed in earlier chapters. In addition, the macroscopic gold electrodes are terminated in one discrete gold atom attached to the two ends of the graphene sensor. The DOS of the semi-infinite gold electrodes act as the source of electrons and calculated using the program CRYSTAL.[115] Next we obtain optimized geometries of several europium nitrate complexes adsorbed on the Au-graphene-Au molecule. When a foreign molecule (europium complex in our case) is adsorbed on top of the graphene surface, it causes a change in electrical conductance of the molecular junction calculated using similar procedure.

The molecular electrostatic map (MEP) is mapped on electron isodensity surfaces for the $Eu(NO_3)_3(H_2O)_4$ complex alone as well as when it is complexed with graphene. The MEPs are observable quantity[149-151] and thus valuable tools to measure chemical reactivity, electron transfer process, and chemical recognition. The electron density is fully and uniquely dependent on the nuclei as per the Hohenberg-Kohn theorem;[59] therefore, when combined with MEP provides a unique signature of the nuclei to be detected.

In order to further understand the bonding nature, we perform natural bond orbitals (NBO) analysis for europium (III)-graphene complexes. NBOs are a set of

orthonormal localized maximum occupancy orbitals that describe the orbitals in the form of core, bonding, anti-bonding, and Rydberg orbitals.[152] This partitioning method is then used to determine atomic partial charges using natural population analysis (NPA).[153] The Mulliken charges are also listed for comparison purpose.

5.3 Results and Discussion

The first and second ionization potentials of europium calculated using the B3PW91/ECP28MWB_SEG level of theory were 5.55 and 11.31 eV, respectively, which are very close to the experimental values of 5.67 and 11.24 eV, respectively.[154] The ground state electronic structures predicted for Eu ($[Xe]4f^7 6s^2$), Eu^+ ($[Xe]4f^7 6s^1$), and Eu^{2+} ($[Xe]4f^7$) matched exactly with published results.[154]

The structure optimizations of europium nitrate complexes reveal that the $Eu–O_W$ and $Eu–O_N$ bond lengths increase when approaching the graphene molecule as shown in Table 1 where O_W and O_N are the nearest neighbor oxygen atoms of water molecules and nitrate ions, respectively. The increase in bond lengths marks the weakening of bonds similar to that observed in case of uranyl and plutonyl complexes adsorbed on graphene.[37-38] We also report the zero-point energy corrections along with total electronic energy for each molecule in Table 5.1.

The binding energies of trinitrate, dinitrate and mononitrate complexes of Eu(III) adsorbed on graphene (Figure 5.1) are calculated as -3.2, -25.3 and -65.5 kcal/mol respectively. The binding energy is defined as the difference between the sum of the total energy of the graphene molecule (G), -2068.73684 hartrees, and that of the nitrate

complex (Table 5.1) from the total energy of the graphene-europium nitrate complex. The zero-point vibrational energies corrections are also included in binding energy.

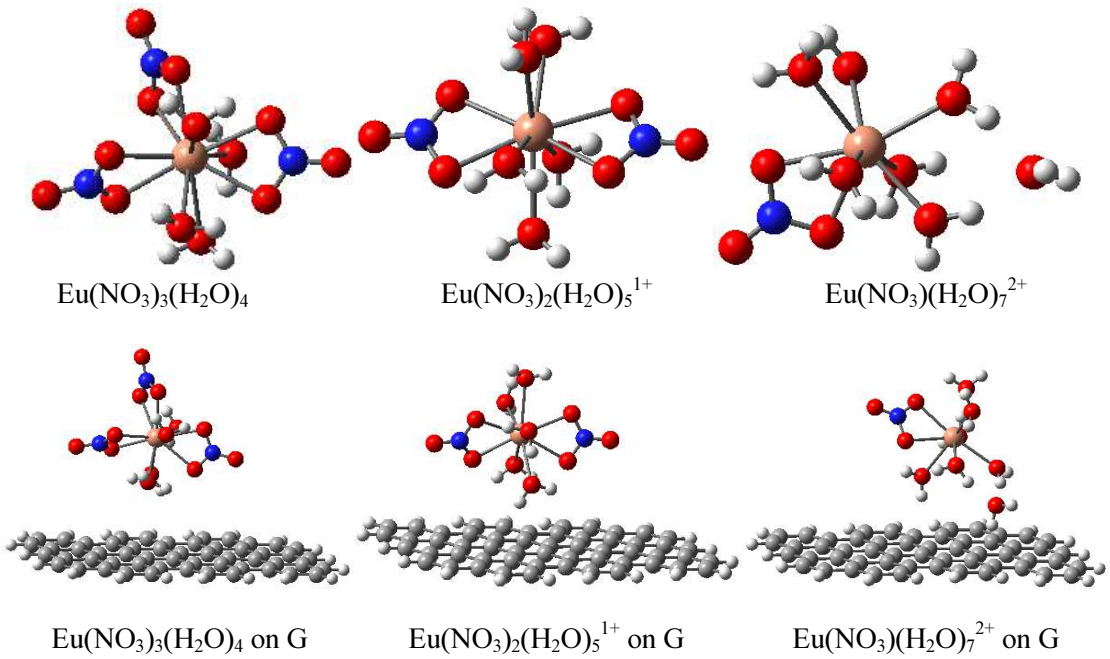

Figure 5.1. Stable conformations of europium nitrate complexes with a graphene molecule (G) $C_{54}H_{20}$. Eu(pink), C(grey), O(red), N(blue), and H(white).

Table 5.1. Calculated Bond Lengths, SCF Energies and ZPE Correction of Europium Nitrate Complexes Before and After Adsorption on Graphene (G)

Complex	Eu–O_W (Å)	Eu–O_N (Å)	SCF Energy (Ha)	ZPE (kcal/mol)
Before adsorption				
$Eu(NO_3)_3(H_2O)_4$	2.51–2.61	2.44–2.50	-1856.98563	94.0
	2.40–2.50[a]	2.47–2.63[a]		
$Eu(NO_3)_2(H_2O)_5^{1+}$	2.44–2.57	2.40–2.42	-1652.95486	98.0

Table 5.1 Continued.

Complex	$Eu–O_W$ (Å)	$Eu–O_N$ (Å)	SCF Energy (Ha)	ZPE (kcal/mol)
$Eu(NO_3)(H_2O)_7^{2+}$	2.44–2.52, 2.44[b]	2.34	-1525.21852	119.9
After adsorption[c]				
$Eu(NO_3)_3(H_2O)_4$_G	2.53–2.64	2.46–2.53	-3926.28482	443.7
$Eu(NO_3)_2(H_2O)_5^{1+}$_G	2.52–2.65	2.48–2.53	-3722.28977	448.1
$Eu(NO_3)(H_2O)_7^{2+}$_G	2.56–2.69	2.52	-3594.61668	469.4

[a] experimental values from X-ray structures[155]

[b] average bond lengths from molecular dynamic simulations[120]

[c] Graphene molecule (G), $C_{54}H_{20}$, with SCF energy of -2068.73684 hartrees

The atomic charge analysis in Table 5.2 indicate that the charge of Eu decreases, that of O_W is unaffected, and that of O_N is affected slightly as when europium nitrate complexes are adsorbed on graphene molecule. However for after adsorption case, as the total charge of the overall complex increases, Mulliken analysis show decreasing charge on Eu. On the other hand, natural population analysis (NPA) shows more consistent atomic charges. Like Mulliken population, the charge of Eu and nitrate O atoms decrease after adsorption, but the charge of Eu increases as total charge of the complex increases. The natural charges of Eu in trinitrate, dinitrate and mononitrate complexes are +1.19, +1.21, and +1.23 after absorption. Atomic charges are not expectation values thus they are based on definitions: Mulliken analysis divides the overlap population equally between two atoms forming a bond and it is known to be basis set dependent whereas

NPA charges are known to show better stability for compounds containing high ionic character.[153]

Table 5.2. Mulliken and Natural Charges of Europium Nitrate Complexes Before and After Adsorption on Graphene (G)

Complex	q_{Eu} (e)	q_{OW} (e)	q_{ON} (e)	q_{Eu} (e)	q_{OW} (e)	q_{ON} (e)
Before adsorption		Mulliken			NPA	
$Eu(NO_3)_3(H_2O)_4$	1.44	-0.81	-0.39, -0.50	1.21	-0.91	-0.35, -0.52
$Eu(NO_3)_2(H_2O)_5^{1+}$	1.55	-0.82	-0.35, -0.50	1.40	-0.92	-0.30, -0.53
$Eu(NO_3)(H_2O)_7^{2+}$	1.60	-0.84	-0.29, -0.48	1.62	-0.96	-0.23, -0.53
After adsorption						
$Eu(NO_3)_3(H_2O)_4$_G	1.39	-0.82	-0.41, -0.50	1.19	-0.92	-0.37, -0.52
$Eu(NO_3)_2(H_2O)_5^{1+}$_G	1.30	-0.83	-0.40, -0.52	1.21	-0.93	-0.36, -0.55
$Eu(NO_3)(H_2O)_7^{2+}$_G	1.18	-0.84	-0.37, -0.53	1.23	-0.96	-0.34, -0.58

5.3.1 Molecular Electrostatic Potential Maps

Figure 5.2 shows the molecular electrostatic potentials (MEP) of europium nitrate complex adsorbed on graphene calculated on a isodensity surface of 0.0004 e/au^3. This

surface encloses all points around the molecule that have the same electron density. The electrostatic potential is color-coded on the isodensity surface ranging from values of +1 (blue) to -1 (red). The isodensity surface is roughly at 2.3 Å from the plane of carbon atoms in graphene. The electrostatic potential of any foreign molecule, such as lanthanide or actinide, is able to modulate the properties of the graphene plasmons (sea of π-electrons on the graphene surface). Similarly, to some extent, as the density of carriers are modulated by the potential in the gate of a field-effect transistor.[156] Graphene electrical and optical responses depend on the interaction of those plasmons with the moieties bound to the graphene surface.

The MEPs are, in principle, indicators of charge affinity at the possible points of interaction of a molecule either before or after the interaction takes place. This is why MEPs are used to predict initial attack sites by another molecule; certainly, the site conditions may change according to the nature of the two interacting molecules. In our particular case under study, the MEP of graphene had a given shape before interacting with a molecule and another shape after a molecule gets trapped on the graphene. We are interested in analyzing those changes in shape around the regions of neutral potential (~0 MEP), i.e., regions in green color in Figure 5.2. A green region near to a yellow one means a change to the negative side and a green region near a light blue correspond to a change to the positive. These shape changes on graphene could produce a change on the current-voltage characteristics that we could use to sense the molecule.We suggest that plasmons are highly sensitive and likely to be affected by the electrostatic field of a single molecule.[157] Indeed, a significant change in the electrostatic field of graphene (Figure

5.2a,b) was observed when interacting with the europium complexes as the potential color map of graphene changes from yellow to blue (Figure 2d) at the nearest distance from the Eu(III) complex (Figure 5.2c). The change in the potential suggests electron transfer from graphene to the europium nitrate complex and is further corroborated from the natural population analysis (Section 5.2). A challenge for the detection is that some water molecules are closer to graphene than is Eu.

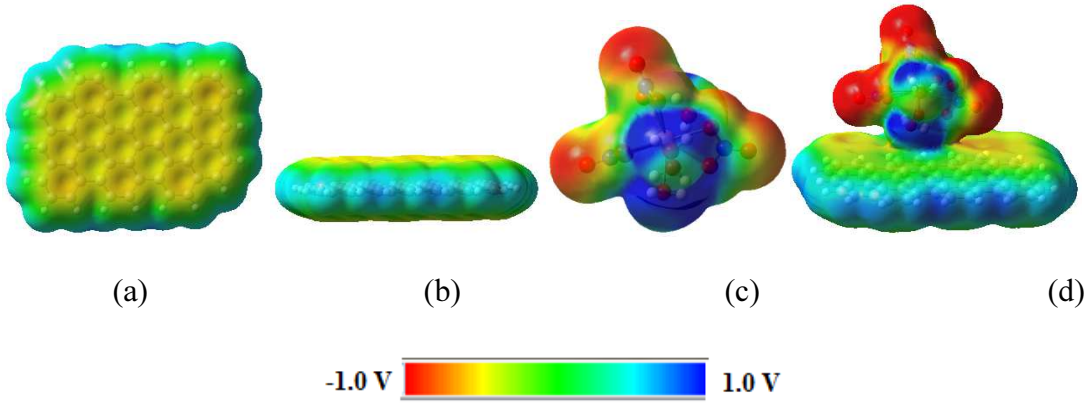

Figure 5.2. Molecular electrostatic potentials of $Eu(NO_3)_4(H_2O)_4$ complexes adsorbed on graphene. Blue is the most positive potential and red is the most negative; all complexes are at the same color scale and the location of the atoms is indicated in Figure 1. (a) top view of $C_{54}H_{20}$ (b) side view of $C_{54}H_{20}$ (c) $Eu(NO_3)_4(H_2O)_4$ (d) $Eu(NO_3)_4(H_2O)_4$ on $C_{54}H_{20}$

5.3.2 Current-Voltage Characteristics

The current-voltage curves (Figure 5.3) for mononitrate, dinitrate, and trinitrate complexes of Eu(III) adsorbed on a graphene molecule were calculated using the procedure GENIP (Chapter II). From Figure 5.3a–b we can infer that water molecules when coordinated to the Eu(III) neutral complex, practically suppress any change in the

electrical conductance of graphene. In general, the electrical conductance of the Au–G–Au junction increases with an increase in the charge of the europium nitrate complex, as seen in Figure 5.3b–d.

We suggest that this trend is a result of the mutual effect of the HOMO–LUMO α-gaps and the delocalization of the frontier molecular orbitals. The α-HOMO-LUMO gaps were calculated as 0.38, 0.40, and 0.37 eV for trinitrate, dinitrate and mononitrate complexes, respectively. On the other hand, a plot of the MO's for the trinitrate complex show that the α-HOMO is fully delocalized on the graphene and partially on the Eu-complex and the α-LUMO is only localized on the Eu-complex. However for the dinitrate both the HOMO and the LUMO are fully delocalized on the graphene and partially on the Eu-complex. Therefore, we conclude that although the dinitrate complex has a slightly larger gap, the effect of delocalization of the HOMO and LUMO results in better conductance than the trinitrate complex.

Finally the mononitrate complex has smaller gap than all of the others and have the LUMO fully delocalized and the HOMO localized on the Eu-complex; we assume that the smaller gap determines the larger conductance behavior of the mononitrate complex. Notice that the beta HOMO-LUMO gaps were 1.67, 1.62 and 1.57 eV, respectively, therefore they are not determining factor for the conductance due to larger HOMO-LUMO gaps with respect to the alpha orbitals; however this large difference between alpha and beta gaps suggests the possibility of using this sensor as a spin filter for spintronics. The HOMO-LUMO gap for graphene molecular junction was estimated to be 1.71 eV; however, this gap becomes 1.69 eV when the gold atoms are added. The

higher charge on the cation complex introduces a strong polarization effect in the graphene molecule. The total natural charges of the graphene molecular junction (Au-graphene-Au) were +0.13, +0.56, and +0.90 in case of trinitrate, dinitrate and mononitrate complexes, respectively, according to the NPA we performed for the three cases shown in Figure 5.3(b–d). These results are of higher importance for dilute solutions. As already shown by others using bulk MD simulations,[120] Eu(III) complexes are more likely to exist in dissociated ion form; the higher charge on the cation will result in higher sensitivity of the graphene junction.

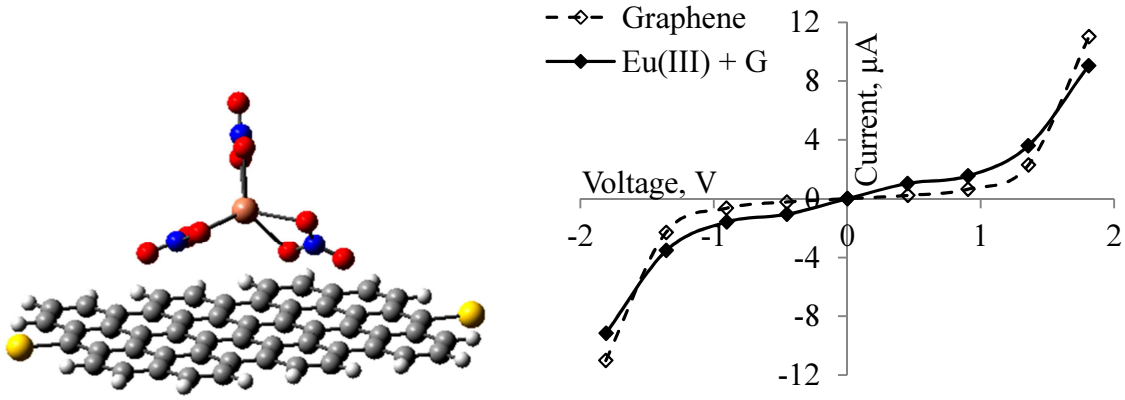

Figure 5.3. Current-Voltage characteristics and frontier molecular orbitals with their energies for (a) $Eu(NO_3)_3$, (b) $Eu(NO_3)_3(H_2O)_4$, (c) $Eu(NO_3)_2(H_2O)_5^{1+}$, and (d) $Eu(NO_3)(H_2O)_7^{2+}$ adsorbed on graphene. These structures were first geometry-optimized and then used as shown in Scheme 1 in order to calculate the I-V characteristics. Dotted lines indicate the response of the graphene sensor before exposure to europium nitrate complexes.

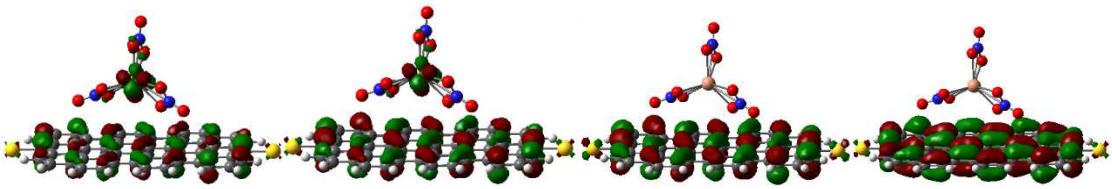

α-HOMO (-4.69 eV) α-LUMO (-4.27 eV) β-HOMO (-4.95 eV) β-LUMO (-3.32 eV)

(a)

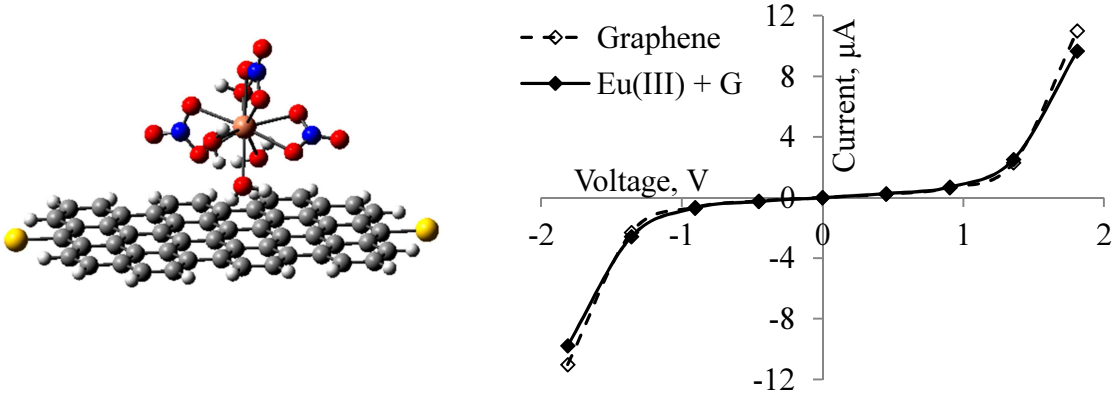

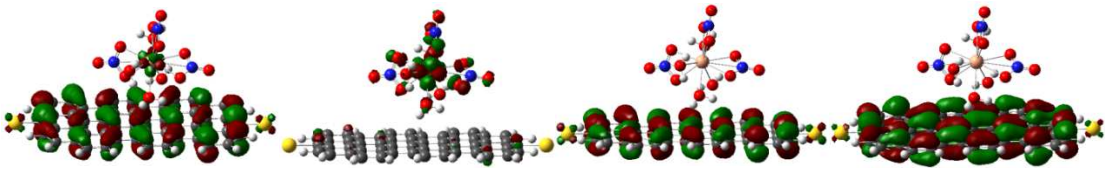

α-HOMO (-4.74 eV) α-LUMO (-4.37 eV) β-HOMO (-4.81 eV) β-LUMO (-3.13 eV)

(b)

Figure 5.3 Continued

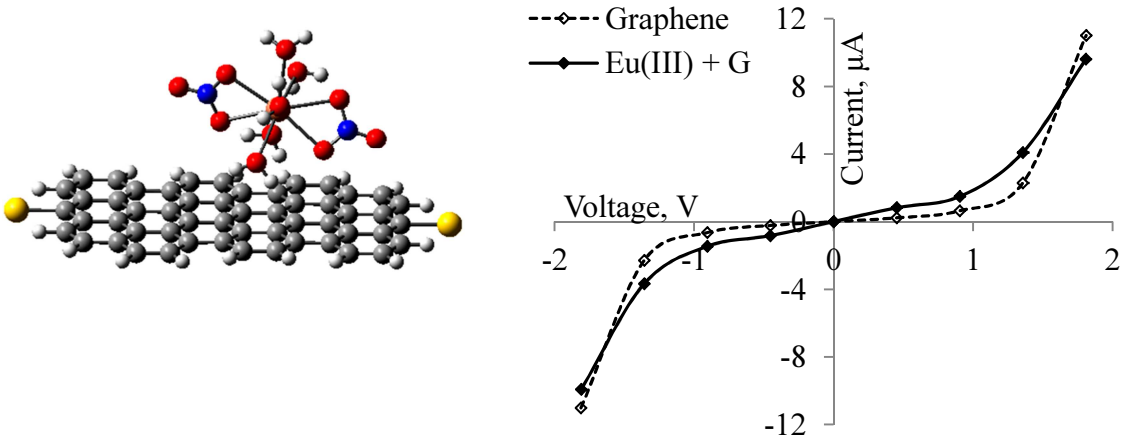

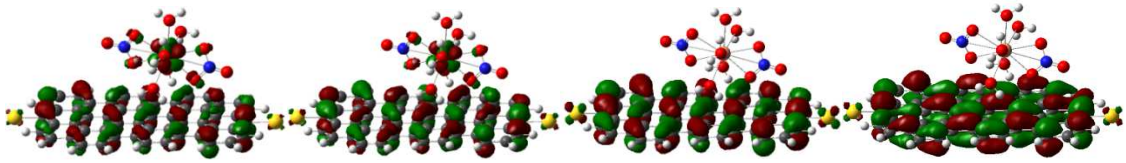

α-HOMO (-6.40 eV) α-LUMO (-6.20 eV) β-HOMO (-6.86 eV) β-LUMO (-5.24 eV)

(c)

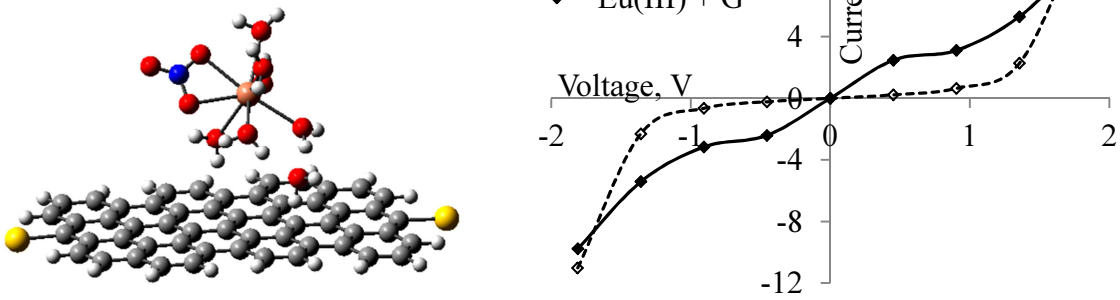

Figure 5.3 Continued

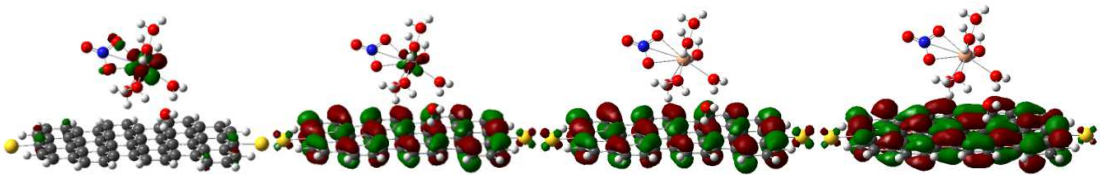

α-HOMOα-LUMO (-8.46 eV)(-8.10 eV) β-HOMO (-8.91 eV) β-LUMO (-7.33 eV)

(d)

Figure 5.3 Continued

We also calculated current-voltage curves for a europium oxide (Eu_2O_3) complex observed on graphene, graphene oxide (GO), and GO containing an epoxy group (Figure 5.4). The results for G (Figure 5.4a) already show a sharp change on the I-V curve when the Eu(III) is added to the sensor, at least in the range from 1 to 2 V showing, as exected a symmetric curve. The graphene oxide we chose has a –CO group on its surface (Figure 5.4b) due to its higher binding tendency towards heavier elemenents.[37-38] The effect on the I-V is even larger than the case of the graphene sensor and it is in agreement with the experimental trends.[122] We observed that the electrical conductance decreased two-fold in magnitude in the case of GO when a single molecule of Eu_2O_3 was in contact with GO. In the case of the GO containing an epoxy group (Figure 5.4c), also a large change is observed on the I-V characteristics at voltages larger than 0.5 V.

The NBO analysis for the three molecules shown in Figure 5.4 was performed in order to understand the charge transfer mechanism. Eu atoms from Eu_2O_3 form strong ionic bonds with the carbonyl oxygen atom present on the GO surface as observed from

the NBO analysis results. The total natural charge on the Eu_2O_3 complex in the presence of GO was +1.25, indicating a strong charge transfer between the GO molecular junction and the Eu_2O_3 molecule. The alpha HOMO-LUMO gap of the Au-GO-Au junction increased from 0.94 eV to 1.37 eV on exposure to Eu_2O_3, resulting in reduced electrical conductance. The graphene molecular junction experienced an ~8.5 increase in electrical conductance in the -1.0 to +1.0 V range. The interaction between Eu_2O_3 and the graphene molecular junction was also purely electrostatic in nature according to the NBO analysis with a total natural charge of the Eu_2O_3 complex of +0.835. Unlike the GO molecular junction, the alpha HOMO-LUMO gap of the Au-graphene-Au junction decreased from 1.71 eV to 1.11 eV when Eu_2O_3 was complexed with graphene. On the other hand, we found that oxygen atoms from the epoxy group are non-reacting towards Eu_2O_3; this is important because epoxy groups are the most common functional groups present on GO. The net charge on Eu_2O_3 complex is close to zero (-0.04) using the NPA, suggesting negligible charge transfer between the europium complex and GO junction after adsorption. The lower values of current are due to the presence of sp^3 hybridized carbon atoms bonded to the O atom and, hence, the electrical conductance is very low when compared to that of the graphene molecular junction. The g_2/g_1 ratio increases from 1.9 at ~0.5 V to 3.9 at ~1.0 V, where g_1 and g_2 are electrical conductance values at the Au-GOX-Au junction before and after, respectively, exposure to the Eu_2O_3 complex.

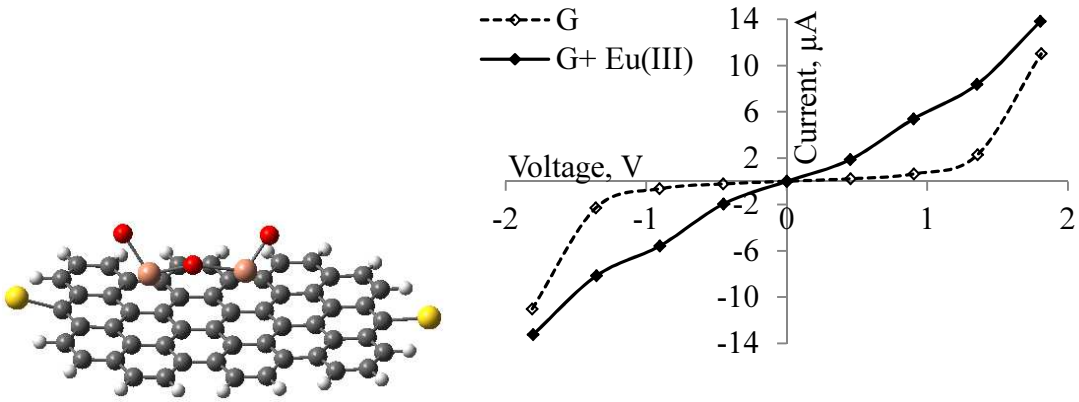

(a)

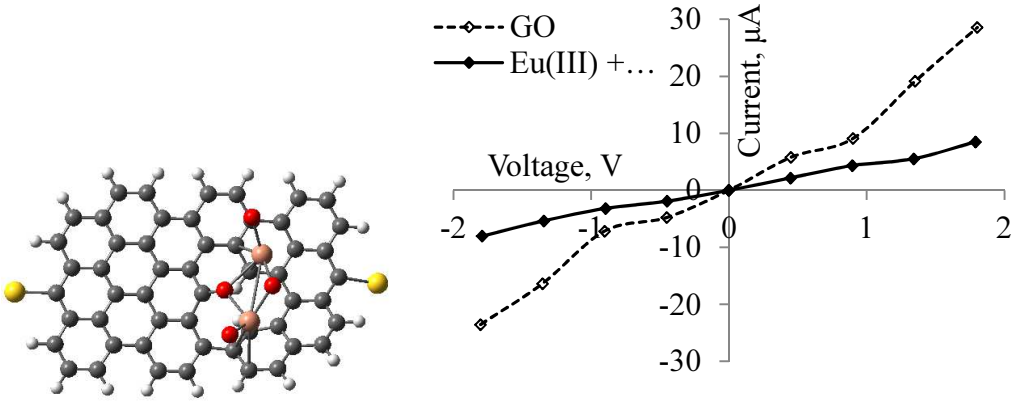

(b)

Figure 5.4. Current-voltage characteristics for Eu_2O_3 adsorbed on the surface of (a) graphene, (b) graphene oxide (GO) with a –CO functional group, and (c) graphene oxide with –O– group (GOX). Dotted lines indicate the current before exposure of graphene sensor to Eu_2O_3.

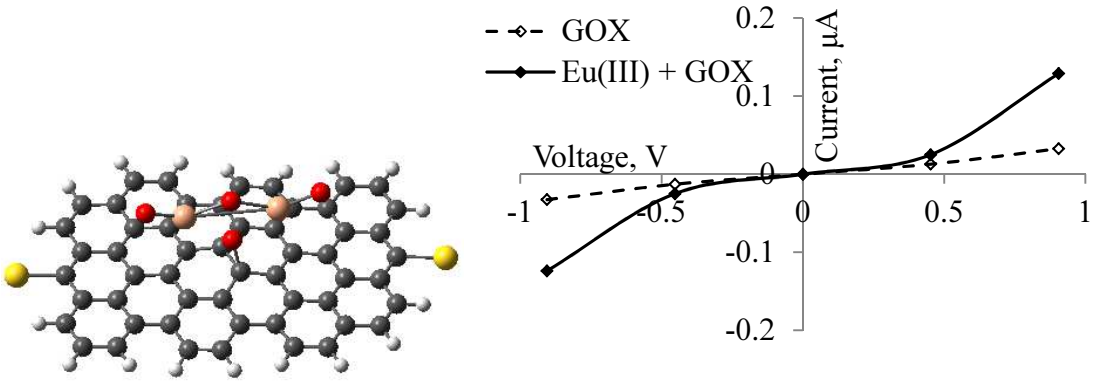

(c)

Figure 5.4 Continued.

5.4 Conclusions

We performed ab initio molecular orbital calculations to predict the behavior of graphene sensors under the exposure of europium (III) complexes and our calculations predict noticeable changes in the electron transport of graphene based sensors; therefore, supporting the fabrication of these nanosensors. The larger the change in electron transport characteristics, the better the sensitivity. The theoretical current-voltage performed on graphene molecular junctions shows an increase in electrical conductance in the presence of Eu(III) complexes. The interaction between Eu(III) ions and graphene was found to be predominantly electrostatic in nature. Conductance increases with an increase in positive charge of europium atom perhaps because the increase produces a combined effect on the energy gaps and on the delocalization nature of the frontier molecular orbitals. In GO molecular junctions, Eu_2O_3 forms strong ionic bonds with

carbonyl oxygen atoms present on the GO surface causing a reduction of conductance as also supported by others. Interestingly, the epoxy O atoms present on the GO surface does not take part in the charge transfer process.

CHAPTER VI

DNA ORIGAMI-APTAMER ASSEMBLY FOR CAPTURE OF THROMBIN

The fabrication of DNA origamis is one of the very few possibilities to create nano-structures with precise atomistic tailored geometries of a variety of shapes. In addition, these origamis can in turn be functionalized or be impregnated with specialized aptamers in order to convert them into nanosensors or to tune them with pre-specified properties simply by impregnating single-stranded DNA or RNA chains (aptamers) via the precise features of DNA pairing. We performed molecular dynamics simulations to determine the relative energetics associated with the capture of thrombin by two aptamers TBA26 and TBA29 attached to a rectangular DNA origami. The molecular simulations provided detailed structural information of aptamer-enzyme interactions which are crucial for the design of aptamer-based biosensors in an efficient way. In addition, the simulations also showed a remarkable selectivity of the biosensor assembly for thrombin. Technical problems due to the large number of atoms involved together with the range of approximations are also discussed. The detection, capture, sensing of enzymes is of great significance in biomedicine. In particular, the detection of thrombin is a major task in cardiovascular diagnostics and therapeutics. On the other hand, our simulations can be extended to detect biotoxins or any other chemical or biological agent by simply choosing proper aptamers.

6.1 Introduction

The DNA origami has emerged as a new and promising pathway to self-assemble DNA into desired complex two-dimensional[158] and three-dimensional shapes.[159] The DNA origami structure usually consists of a single long DNA strand (scaffold) of a viral genome which is folded back and forth in a desired pattern so that it constitutes one of the two strands in each helix. The DNA helices are held together by a periodic array of crossovers at which short complementary oligonucleotides (staple) run from one helix and continue to the next helix to keep the scaffold in place.[158] The programmed folding of DNA strands into custom shapes can have profound applications in nanotechnology such as molecular electronics,[78,81,158,160-166] mobile nano and micro mechanical devices,[167] biosensors and therapeutics,[168] precision catalysis, and several others yet to be discovered. In particular, the DNA origami can act as a vehicle for docking of protein- or enzyme-specific aptamers without loss of activity, and therefore, it can be used as a biosensor. Aptamers are single stranded DNA or RNA chains, typically consisting of 15-40 nucleotides in length with high affinity and specificity for molecular targets such as proteins, nucleic acids and other small organic molecules.[169-172] Nucleic acid aptamers have significant advantages over protein therapeutics due to smaller size, non-immunogenicity,[169-170] and stability over wide pH and temperature range.[170] Thrombin inhibition by aptamers can be reversed by using complementary single stranded DNA sequences (antidotes).[168,173] Aptamers cause minimal immune response and toxicity when compared to conventional drugs;[173] however, aptamers are limited by relatively short half-life due to nuclease degradation.[170] In order to enhance their

activity towards target molecules and stability against degradation, two common strategies apart from chemical modification, have been developed: (1) using assembly of aptamers joined together by simple nucleotide linkers[173] or annealing to more complex DNA scaffolds[168] and (2) conjugation of aptamers to nanoparticles.[174] In this work, we are interested in detection of thrombin, a serine protease involved in blood coagulation. Thrombin is directly involved in the conversion of soluble fibrinogen (a glycoprotein) into fibrin clot as well as platelet activation.[169,173] The presence of thrombin indicates the existence of blood clot.

Among others, there are three well known aptamers for thrombin, TBA15 (HD1), TBA26, and TBA29 also known as HD22. The structure of TBA15 (5'-GGTTGGTGTGGTTGG-3') has been determined experimentally and is characterized as a chair-like quadruplex arrangement consisting of two planar guanine quartets connected by two TT loops and a single TGT loop.[173,175] [175-176] The structure of TBA26 (5'-CGCCTAGGTTGGGTAGGGTGGTGGCG-3') has not been determined crystallographically; however, there exists structural similarities between TBA15 and TBA26.[177] The structure of TBA29 has also been published in literature[173,178] but it consists of 27-mer only without the first and last nucleotides. TBA29 ('5-AGT CCG TGG TAG GGC AGG TTG GGG TGACT-3') contains both a G-quadruplex connected by two TT and a GCA loop and a duplex motif near 5'- and 3'-ends.[178] TBA15 and TBA26 binds on anion-binding-exosite I (ABE-I) using their quadruplex structure while TBA29 is known to bind on anion-binding-exosite II (ABE-II) of thrombin using its duplex structure.[173,179] ABE-I is responsible for molecular recognition of fibrinogen

while ABE-II is required for interaction with heparin (an anti-coagulant), a cofactor for the inhibition of thrombin by antithrombin (a glycoprotein produced by lever).[169]

Aptamers have shown to be very promising for designing biosensors for detection of several types of enzymes such as thrombin. Several aptamer-based sensors for thrombin utilizing a single 15-mer thrombin binding aptamer (TBA)[171,180-181] or two non-overlapping aptamers (TBA15 and TBA29),[172,182-183 184] have been reported and their sensing mechanisms can be based on several strategies such as fluorescence resonance energy transfer (FRET),[172,181-182] electrochemistry,[183-184] surface enhanced Raman scattering (SRS),[180,185-186] and surface enhanced resonance Raman scattering (SERRS).[171] There has been considerable research on SERS-based sensors for thrombin. Bizzarri *et al.*[185] reported a SERS-based sensor using gold nanoparticle capped with a bifunctional molecule having a thiol group to bind with gold nanoparticles and a diazonium moiety capable of reacting with aromatic residues of protein; their detector was based on typical vibration of diazo bonds. On the other hand, Pagba *et al*.[180] designed a SERS based sensor using TBAs as molecular receptors; this sensor utilized immobilized silver nanoparticles functionalized with thiol modified TBA15 and the binding of thrombin was indicated by the presence of additional Raman bands. Wu *et al*.[186] developed a turn-off biosensor using a combination of SERS and enzymatic amplification for detection of thrombin. Among the electrochemical sensors, Zheng *et al*.[183] fabricated a two-aptamer based sensor in sandwich shape; one of the aptamers was immobilized on a magneto nanoparticle while the other aptamer was labeled with gold. In a separate work, Yang *et al*.[184] implemented a sandwich-like biosensor where one of

the aptamers was attached to gold electrodes via a thiol group while the second aptamer was labeled with CdSe quantum dots. Fluorescence-based sandwich microarray for detection of thrombin using two distinct aptamers has also been reported.[172,182] On the other hand, the impedance of DNA origamis were reported experimentally at room temperature[187-188] and as function of temperature[189] which can be potentially exploited to tether aptamers in fixed positions for designing electrochemical sensors.

The binding affinities of TBAs with thrombin have been reported both experimentally and theoretically using molecular mechanics; the experimental binding free energy of TBA15 with thrombin was reported as 8 ± 1 kJ/mol using isothermal titration calorimetry[190] while theoretically the binding free energy was reported as 17 kcal/mol using molecular dynamics and umbrella sampling.[191] In another theoretical work, HD22 was shown to have higher binding energy than HD1.[192] The theoretically calculated binding free energies are usually on the higher side. Recently, Rangnekar et al.[168] showed that multiple aptamers tethered at programmed positions on an origami-based DNA weave-tile structure can be used to maximize anticoagulant activity; the DNA architecture used only 2 DNA strands without any cross-overs and the helix ends were connected by –TTTT– loops and the aptamers HD1 and TBA29 (HD22) were connected to the DNA nanostructure via a –TT– spacer; the antithrombin activity of the aptamer-DNA nanostructure as well as its reversal were found to be rapid and stable. [168] [168] [168] [168] [168] [168] [168] [168] [170] [171] [169] However, there are not many studies done on the structure and dynamics of these assemblies to understand the phenomena at molecular level. In a pioneering work, Yoo et al.[193] using an all-atom molecular dynamics simulation reported

the characterization of the structure and dynamics of rod-like monolithic DNA origami and structural properties were found to match with experiments. In another work, by King et al.,[194] continuum mechanics was applied to study the stretching, twisting and bending mechanics of DNA origami structures by modeling them as bundles of homogeneous elastic rods connected by rigid crossovers using finite elements method.

In this chapter, using an all-atom molecular dynamics approach, we study the structure and dynamics of thrombin docked on an aptamer-DNA origami assembly prepared for biosensing applications. We obtain complete structural models of TBA26 and TBA29 based on the knowledge of nucleotide sequences and structural similarities between TBA15 and TBA26. The TBA26 and TBA29 aptamers are then docked on a rectangular DNA origami and the molecular dynamics of the thrombin biosensor assembly in the presence of thrombin is performed using the CHARMM27 force field. The simulations not only show a remarkable selectivity of the nanobiosensor assembly for thrombin, but also can be extended to detect biotoxins such as ricin by simply choosing proper aptamers.

6.2 Methodology

The molecular dynamics of thrombin biosensor assembly has been performed using LAMMPS program.[195] The CHARMM27 force field[196-197] is employed for DNA origami and protein structures along with TIP3P water model. The ion parameters are taken from CHARMM27 force field. The DNA origami is constructed using caDNAno program.[198] The spatial arrangement of DNA origami consists of rod-like structures on a

square lattice. The origami consists of a long continuous scaffold with cross-overs at fixed length. Complementary DNA strands (also referred to as staples) are then added to the scaffold. The sequences corresponding to circular genomic DNA from the virus M13mp18 are then assigned to both scaffold and staples. An all-atom representation is then generated from the caDNAno geometry along with the sequence using caDNAno to PDB conversion tool.[193,199]

All-atomic models of two aptamers TBA26 were generated from their known sequences and structural information available in literature using the UCSF Chimera program[200]. TBA26 is known to bind at the exosite I of thrombin using G-quadruplex structure similar to TBA15. We replaced TBA15 by TBA26 in the x-ray crystallographic structure of human alpha thrombin inhibited by 15-mer DNA aptamer (PDB ID 1HUT)[176] and then using sequence matching we docked TBA29 on the exosite II using x-ray crystallographic structure of alpha thrombin complexed with 27-mer aptamer (PDB ID 4I7Y)[178]. Two staples of DNA origami nanostructure are then selected and their backbone is split in the middle, creating aptamer junctions. The approximate distance between two split points is ~60 Å. The ends of the two aptamers TBA26 and TBA29 along with thrombin are then connected to the origami at the specified locations using four thymine bases as connectors at each end of the aptamers. Thrombin is then finally docked on the biosensor using Chimera program by careful placement of the thrombin-aptamer binding sites. The biosensor-thrombin assembly is further solvated by adding an extra 5 Å blanket of water molecules to avoid interaction of the origami structure with its image. Counter-ions (Na^+) are added to make the whole

system neutral. All the visualizations have been performed using VMD program[201]. The structure files are generated using psfgen tool available in VMD. Finally LAMMPS input files are generated using the charmm2lammps tool available in LAMMPS program using the CHARMM27 topology and parameter files[196].

We use periodic boundary conditions in all three-directions and an inner and outer cut-off of 14 and 16 Å are used for both Lennard-Jones and Coulombic potentials, respectively. We avoided long range electrostatic corrections due to the little uniformity of the whole system as well as to avoid interaction of aptamers and thrombin with their respective periodic images. The MD simulations begin with a minimization in order to fix any unusual bonds created initially, followed by a ramp of temperature from 0 K to 300 K using a time step of 0.5 fs under the Berendsen thermostat[202] with a damping time of 50 fs under the NVE ensemble. The system is then equilibrated at 300 K for 3 ns under NVT ensemble with a time step of 1 fs. The average interaction energy of thrombin with the rest of the atoms is obtained during a 500 ps of production run.

The steps following the aptamer connections are repeated several times by moving the thrombin to four different locations both in horizontal and vertical directions on the biosensor in order to access the likelihood of the binding event of protein-origami assembly . The number of water molecules and ions as well as volume of the simulation box is kept fixed for all cases in order to have a consistent comparison. Our study is based on the assumption that the interaction energy of thrombin to the aptamer-origami assembly in the presence of solvent and counter-ions can be used as a measure of probability of binding event. In addition, we also performed molecular dynamic

simulations of TBA26 and TBA29 in the presence of thrombin individually in order to compare their binding affinities.

6.3 Results and Discussion

Molecular dynamic simulation of TBA26-thrombin and TBA29-thrombin show that TBA26 binds to the exosite I of thrombin using its G-qadruplex structure whereas TBA29 has a higher affinity for exosite II of thrombin and binds using both G-quadruplex and duplex motifs. The root mean square displacement (RMSD) of protein structure for the two cases are shown in Figure 6.1a,b during the course of equilibration at 300 K. We observed that the RMSD becomes constant after 3 ns of equilibration. The pair-wise interactaction energy of TBA26 and TBA29 with thrombin is plotted in Figure 6.1c,d. Thus TBA29 has a much higher binding afffinity for thrombin than TBA26 as indicated by higher interaction energy between TBA29 and thrombin.

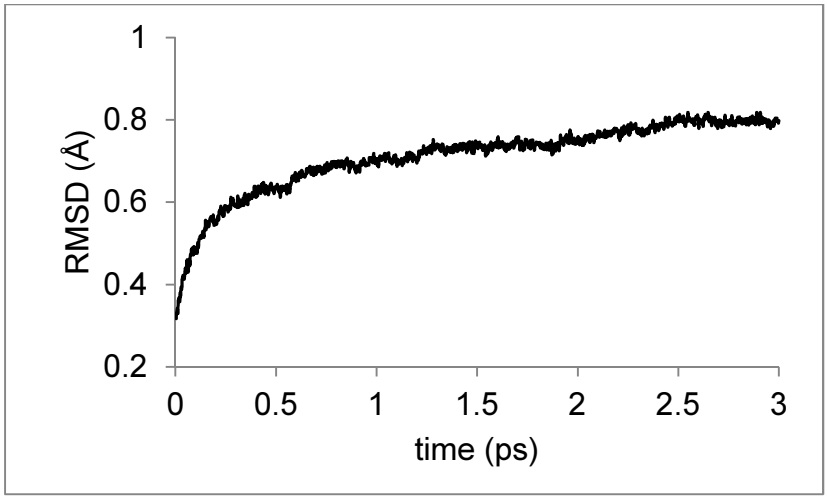

(a)

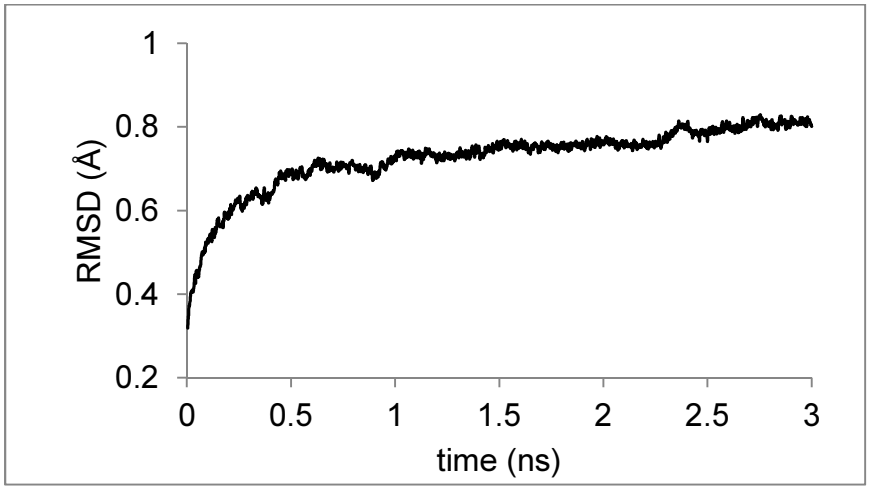

(b)

Figure 6.1. Root-mean-square displacement of thrombin during equilibration at 300 K for (a) TBA-thrombin complex and (b) TBA29-thrombin DNA complex. Pair-wise interaction energy of thrombin with (c) TBA26 and (d) TBA29 aptamers

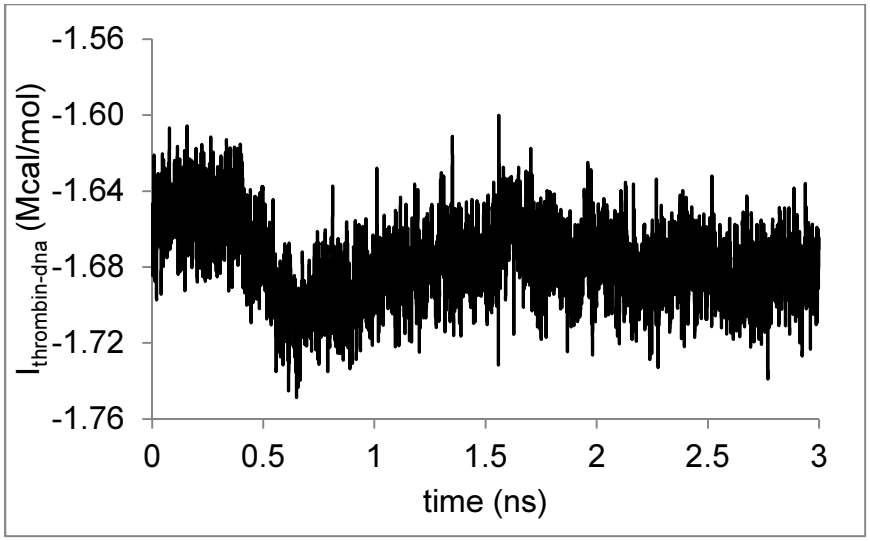

(c)

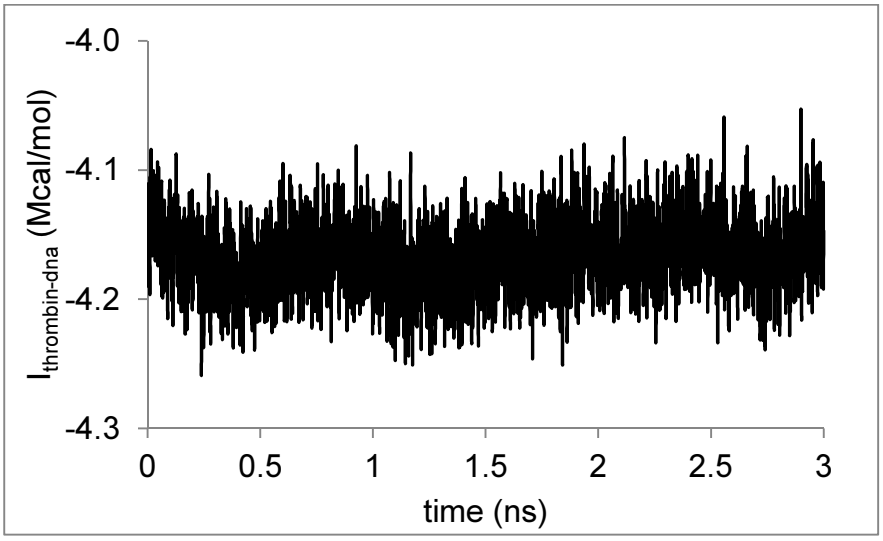

(d)

Figure 6.1 Continued.

Figure 6.2 shows thrombin docked between the TBA26 and TBA29 aptamers, which are tethered to the DNA origami structure at 300 K after 3 ns of equilibration.

The entire system is immersed in a box of water molecules. Sodium cations are added to make the system neutral.

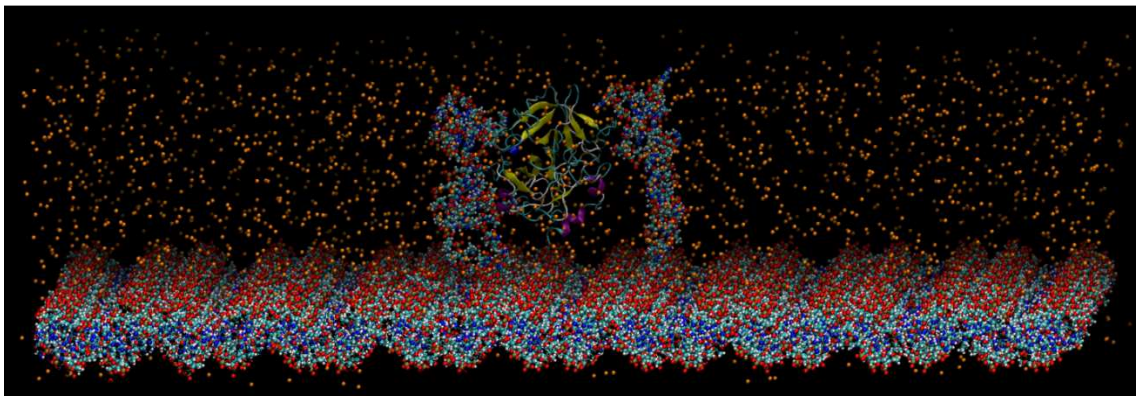

Figure 6.2. Docking of thrombin on DNA origami-aptamers assembly

The DNA origami surface is composed of a long scaffold made of 1,152 nucleotides, 33 staple strands with 32 nucleotides each, 2 staples with 26 nucleotides each, and 2 staples with 22 nucleotides each. The two vertical aptamers are TBA29 on the left (37 nucleotides including –TTTT– at both ends) and TBA26 on the right (34 nucleotides including –TTTT– at both ends); in addition, there are 2,371 Na^+ ions (orange dots) all surrounded by 239,243 water molecules (not shown for the sake of clarity). The total number of atoms is 800,133 and the whole box is 338.8 Å long, 273.0 Å wide and 93.8 Å high; with 328.8 Å and 263.0 Å as the length and width of the origami plane.

Table 6.1 provides the detailed pair-interactions of thrombin with two aptamers. The TBA29 (left aptamer in Figure 6.3) interacts with multiple residues of thrombin (88-94, 123-132, 159-166, 237-248) when using both, the duplex as well as the quadruplex

structure. The aptamer TBA26, however, only interacts with thrombin residues (9, 62, 66, 70-78, 114) using its G-quadruplex structure.

Table 6.1. DNA Aptamers (A)' Nucleotides (N) Interacting with Thrombin Residues

A	N	thrombin residues
TBA26	THY 9	ILE 9, HSD 66, GLU 72, ILE 75, TYR 114
	THY 10	ARG 73, ASN 74, ILE 75
	GUA 11	ARG 73
	GUA 18	ARG 62, TYR 71, ILE 78
	THY 19	ARG 70, TYR 71, ARG 73
	GUA 20	ARG 70
TBA29	GUA 6	ARG 89
	GUA 9	ARG 89
	THY 10	PRO 88, ARG 89, TYR 90, ASN 91, TRP 92, ARG 93, GLU 94
	ADE 11	ARG 89, ARG 93
	GUA 18	LYS 244
	THY 19	TYR 85, TRP 241, LYS 244, GLN 248
	THY 20	HSD 87, PRO 88, ARG 89, TRP 241, LYS 244
	GUA 21	ARG 89
	GUA 22	LYS 240
	GUA 23	ARG 237, LYS 240
	GUA 24	ARG 123, ARG 237
	THY 25	ARG 123, ARG 127, LEU 130, GLN 131, ALA 132, ILE 159, ARG 162, ARG 237
	ADE 27	ARG 162, ASP 175
	CYT 28	PRO 163, LYS 166

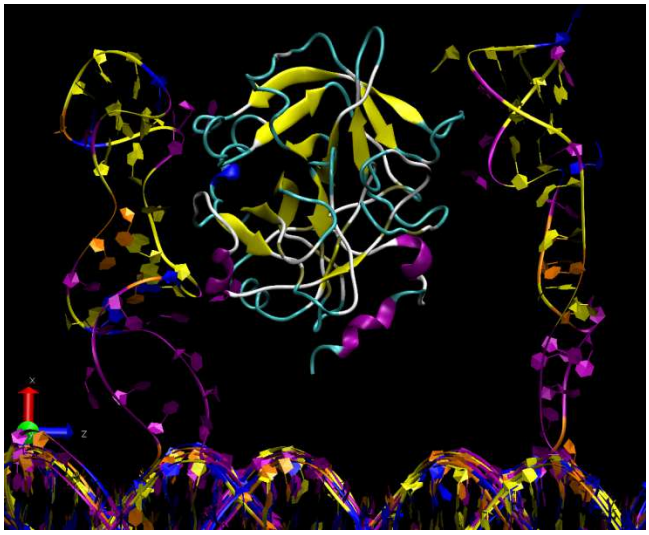

Figure 6.3. Equilibrated structure of thrombin docked between two aptamers TBA29 (left) and TBA26 (right) at 300 K. The aptamers are tethered to the DNA origami by a TTTT sequence at both ends. Aptamers are represented by *ribbons* and are color coded based on their residue type: ADE (blue), CYT (orange), GUA (yellow), and THY (magenta). Thrombin (center) is represented as a *cartoon* and color coded according to its secondary structure.

Figure 6.4 shows the variation of the sum of the kinetic and potential energies versus time during an equilibration run at 300 K. Though there is a small negative slope at the end of the 3 ns, the interaction energy of thrombin with origami and other molecules becomes fairly constant. The small change in the total energy is due to further relaxation of the DNA origami structure. The kinetic energy reached steady state quickly as shown by the almost flat behavior of the temperature-time plot. .

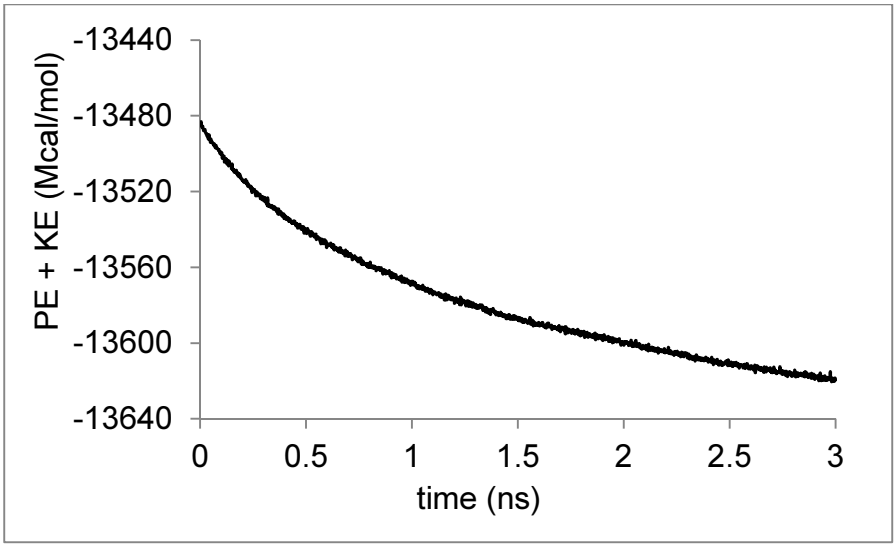

(a)

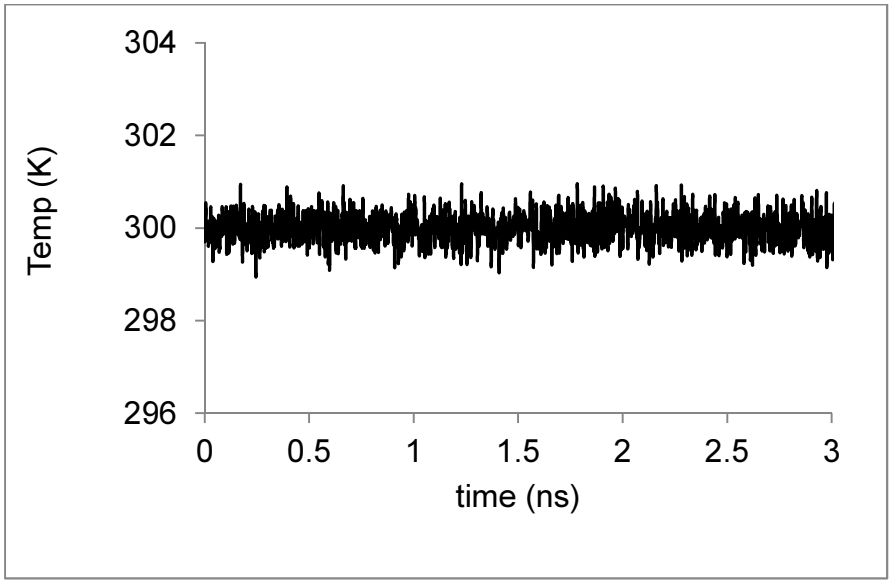

(b)

Figure 6.4. Total energy (a) and temperature (b) evolution during equilibration of DNA origami-thrombin assembly at 300 K shown in Figure 2 and Figure 5a**,** (c) Root mean square displacement of thrombin trapped between two aptamers as a function of time during equilibration at 300 K.

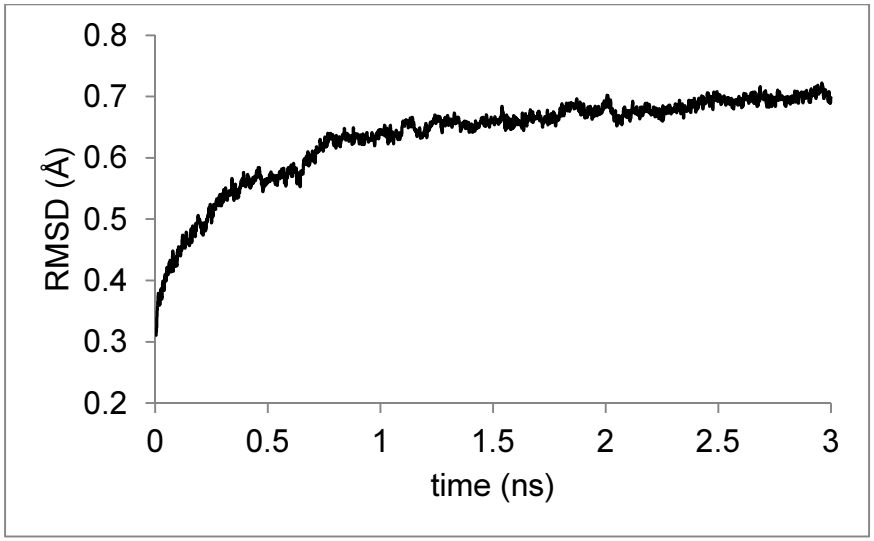

(c)

Figure 6.4 Continued.

Since our goal is to study the capture of thrombin using a DNA origami-aptamer assembly, we made an attempt to study the migration of thrombin on the origami surface. However, the simulation time span of realistic simulations is insufficient to study this phenomenon, primarily due to the large size of the whole system. Therefore, in order to determine the binding properties of DNA origami-aptamers assembly, we performed 5 different molecular dynamics runs starting from several locations of thrombin on the origami surface (Figure 6.5). Figure 6.6 shows the variation of total interaction energy of thrombin with rest of the atoms including water and ions over last 500 ps of equilibration. We then calculated the average and standard deviation of interaction energy of thrombin with its surroundings as listed in Table 6.2. We use the total values of energies to check the equilibrations of our samples; however the energy relative values are used to

understand the energetics. Among all the pair interaction energies, the one for thrombin with DNA origami-aptamers assembly (column *dna* in Table 6.2) is the most important. Our hypothesis is that the latter provides the binding affinity of thrombin with the aptamer-origami assembly in the presence of counter-ions and solvent

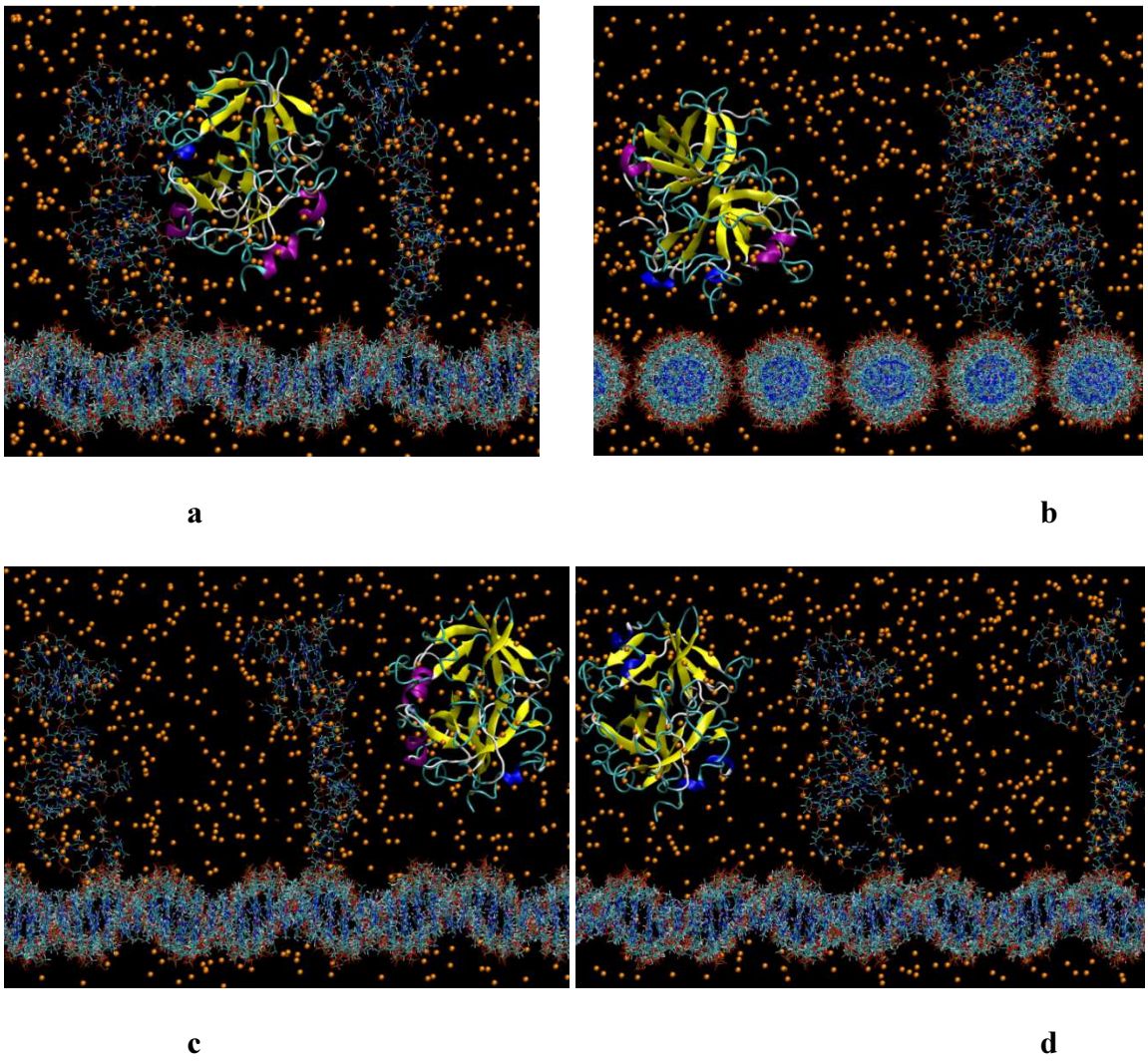

Figure 6.5. Snapshots (structures) of equilibrated structure at 300 K for several locations of thrombin on the DNA origami-aptamer assembly: a bound to the two aptamers at exosites I and II, b away from the two aptamers facing the two aptamers, c approaching

TBA26, d approaching TBA29, and e interacting with the two aptamers away from exosites I and II.

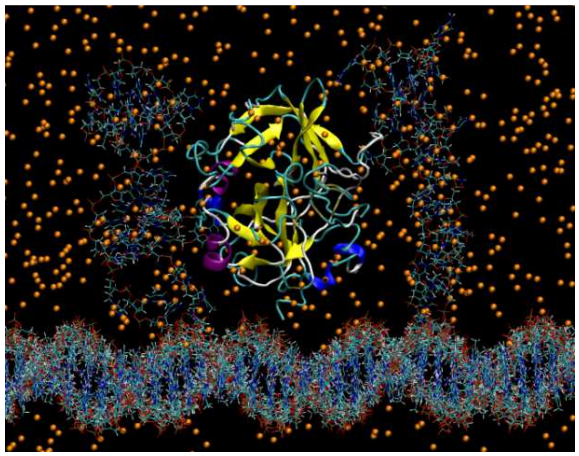

e

Figure 6.5 Continued.

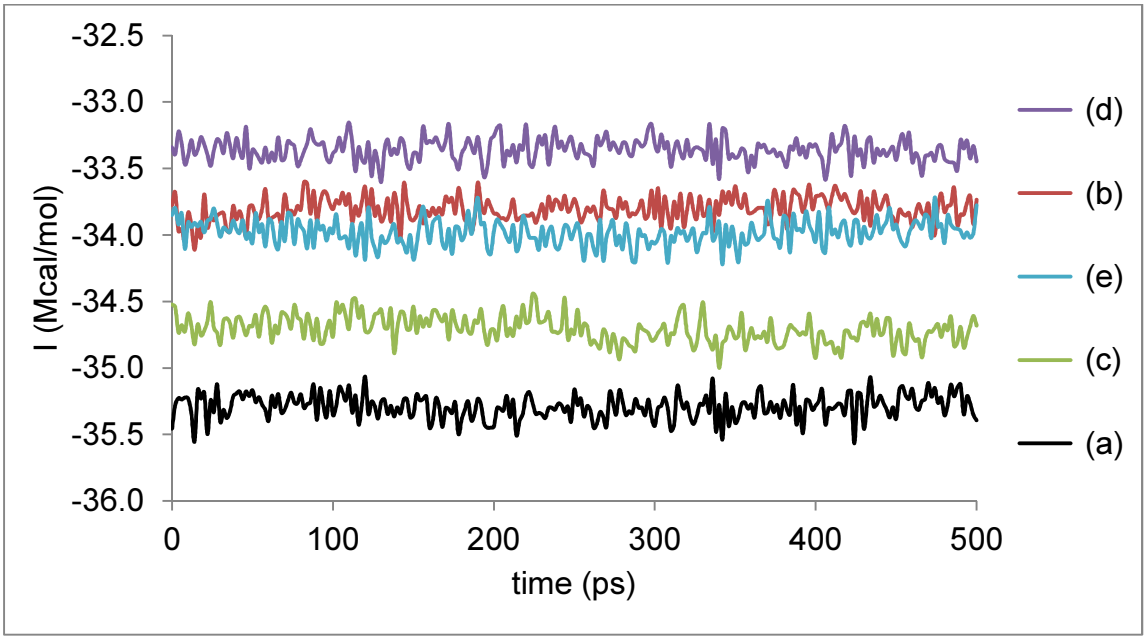

Figure 6.6. Interaction energy versus time of thrombin with the rest of the atoms present in the system for each of the five locations of thrombin shown in Figure 6.5

Based on the total interaction energy of thrombin with rest of the atoms, structure **a** where thrombin is docked between two aptamers has a maximum negative energy followed by structure **c** where thrombin is very far from TBA29 but somewhat closer to TBA26. However, when considering the interaction of thrombin with DNA origami-aptamer assembly alone (column *dna* in Table 6.2), the structure **a** has a much greater contribution of interaction with aptamer-origami assembly when thrombin is docked between two aptamers. There is a higher contribution from thrombin-solvent interactions when thrombin is far from the aptamers compared to the structures **a** and **e**. This suggests that there is an exchange of neighboring water molecules when thrombin binds to the aptamers as it has been also suggested in previous literatures.[203-204] However, in bulk water, the effect of solvent and ions are expected to be uniform and the interaction of thrombin with aptamer is expected to dominate. All conformations show a negative binding energy due to electrostatic repulsion between negatively-charged DNA and thrombin residues. However, when thrombin is located between two aptamers (structure **a**), the binding energy is much larger than when thrombin is closer to each of the aptamers individually (Figure 6.1c,d). As the thrombin moves farther from origami-aptamer assembly, the interactions become very weak. We also performed equilibration runs by moving thrombin perpendicular to the origami plane and much closer towards the origami surface (structure **e**). Compared to structure **a**, the binding energy is smaller due to the difference in binding sites. Thus the interaction of thrombin with the aptamers is very site-specific and any change in the location of thrombin with respect to the two aptamers, as shown in structure **a**, results in a lower binding affinity.

Table 6.2. Average Interaction Energies of Thrombin with the Components of the Origami Assembly[1]

s	*all*	Δ	*dna*	Δ	*ion*	Δ	*water*	Δ
a	-35,289	93	-6,110	32	-451	13	-28,729	90
b	-33,806	92	-35	10	223	14	-33,993	91
c	-34,707	100	-678	12	-226	12	-33,802	101
d	-33,360	87	-852	15	-375	16	-32,133	87
e	-33,982	97	-6,002	36	10	13	-27,990	90

[1]Interactions with DNA ions and water (*all*), DNA assembly only (*dna*), ions only (*ion*), and solvent only (*water*); each followed by their standard deviations (Δ) for all structures (*s*) in Figure 6.5. All energies are in kcal/mol

We also did a comparison analysis of the two minima structures in order to study the effect of cut-offs for non-bonded interactions by performing equilibration runs using inner/outer cut-off of 8Å/10Å, 10Å/12Å, 12Å/14Å, and 14Å/16Å. The ineteraction energies of thrombin with the rest of the molecules present in the system were calculated for each structure and compared with each other. Except for 8/10 Å cut-off, the structure with thrombin captured between two aptamers (structure **a**) has the maximum negative interaction energy in all structures.

6.4 Conclusions

We performed a molecular dynamics study of the structure and capture of thrombin by a DNA origami-aptamer assembly in order to estimate binding affinities based on relative energy of interaction between nuclic acids and thrombin residues. We

found that TBA29 shows a higher binding energy to thrombin than to TBA26, which binds to exosite I via its quadruplex structure while TBA29 prefers exosite II via both of its duplex and quadruplex structures to bind to thrombin. The two aptamers attached to the DNA origami assembly have better binding affinity to thrombin than the corresponding binding of the two aptamers without the origami, meaning that the origami boost each individual aptamer binding to thrombin. Thrombin shows a strong interaction with water molecules which can be a challenge in designing efficient biosensors. Nevertheless, predictive modeling can provide a deep insight into the function of biomolecules and thermodynamic processes of binding with novel biosensor assemblies.

CHAPTER VII

HYDRODESULFURIZATION OF HEAVY OIL USING CLUSTER MODEL*

Using materials genome initiative ideas, it is possible to create new materials with tailored properties for applications in nanoelectronics, catalysis among many other fields. With current advances in computational resources both software and hardware, catalyst design from first principles is becoming reality. The removal of sulfur from heavier fractions of crude oil as well as middle distillates has a great significance in petroleum refining industry. The growing uncertainties in supply of crude oil have forced refiners worldwide to process wide variety of crude. In order to adhere to the stringent environmental norms, the refineries now have to produce gasoline and diesel with sulfur content as low as few ppm which demands highly effective novel catalysts.

7.1 Introduction

Molybdenum disulfide, MoS_2, is a versatile material belonging to layered transition-metal dichalcogenide family and composed of vertically stacked, weakly interacting layers held together by van der Waals forces. The wide range of electronic, optical, mechanical, chemical and thermal properties of MoS_2 has been the focus of many review articles in the past.[205-207] It has a sizable bandgap that changes from indirect to direct bandgap on exfoliation of single layer which causes changes in

* Reproduced in part with permission from N. Kumar and J.M. Seminario, J. Phys. Chem. C, Vol 119, Issue 52, Pages 29157-29170. Copyright 2015 American Chemical Society

photoconductivity, absorption spectra and photoluminescence.[206] As a result, MoS_2 has great potential applications in electronic devices,[206,208] photodetectors, and optoelectronic devices[209]. The edge modification of MoS_2 clusters is responsible for the enhanced catalytic activity in HDS catalysis[210] and electrocatalysis for hydrogen evolution[211-215]. Its high surface-to-volume ratio can be exploited in molecular sensing applications like NO[216], NO_2[217] as well as biomolecules[218]. The application of MoS_2 for energy storage application[205,219] has also generated significant interest among researchers. Due to high reversible capacity, easier intercalation and extraction of lithium ions and low average voltage, MoS_2 has potential applications as both anode[215,220] and cathode[221] materials for secondary lithium ion batteries.[205]

The hydrodesulphurization (HDS) is one the most important processes in a refinery to remove sulfur containing compounds from petroleum fractions. Common catalysts used for removal of sulfur from heavy oil in refineries are mainly based on molybdenum disulfide (MoS_2), usually promoted with cobalt or nickel, which modify the electronic properties of the MoS_2 matrix, thus enhancing its desulfurization catalytic activity.

Over the last decade, significant effort has been made to elucidate the reaction mechanisms and to identify reaction intermediates using both periodic and finite cluster approaches via density functional theory. The advantage of using periodic calculations using plane wave basis sets is the lower computational cost to study large MoS_x clusters; however the drawback is the high coverage and defects are difficult to model.[222] However, industrial catalysts are highly dispersed and have predominant sizes within 10-

30 Å, i.e., one to four Mo atoms on a corresponding edge assuming regular hexagonal clusters as most stable structure.[223] Therefore, the use of MoS_2 clusters with sizes close to real MoS_2 particles instead of periodic structures should be more realistic.[224] The cluster approach provides efficient analysis tools for single molecule adsorption.[222]

Theoretical study of MoS_2 surface showed that depending on the reaction conditions, the catalytic edges are covered by sulfur and hydrogen and there are not many actives sites or coordinately unsaturated sites (CUS) available for HDS reaction.[225-227] Hydrogen undergoes dissociative adsorption forming Mo–H and S–H pairs as most favorable case. Under working conditions, the most stable surface obtained was Mo-edge with 50% sulfur coverage with S atoms in bridging positions.[226,228-230] The promoter atoms Ni and Co were located predominantly at the edges with Ni substituting Mo atoms at the Mo-edge while Co atoms substituting Mo atoms at the S-edge.[225,228,230-231] The Ni atoms at the Mo-edge resulted in square planar structures and were not covered by S atoms under HDS conditions while Co and Mo atoms at the S-edge were 50% sulfide with sulfur atoms in bridge positions. The bridging sulfur atoms on Mo atoms were located in zig-zag configuration while those on Co atoms occupied regular bridge positions between metal atoms.[232] Hydrogen can also react with S creating vacancies and it was shown that the barrier to create a vacancy on Mo-edge was 0.67 eV, i.e., it was lower than the barrier for S-edge, which was 1.34 eV. The promoters Co and Ni decrease the barrier to create vacancies on Mo- and S-edges.[226] The H_2 to H_2S molar ratio decreases at the end of a catalytic cycle or at the bottom of an industrial reactor and the most stable surface is the one with three sulfur atoms on Mo-

edge and S-edge containing six sulfur atoms. The adsorption mechanism of thiophene and DBT on MoS_2 catalyst have been studied in detailed.[233] Two common modes of adsorption are the η_1 and η_5. The HDS of DBT can follow either direct desulfurization (DDS) forming biphenyl or a hydrogenation (HYD) pathway forming cyclohexyl benzene as final product.[233] There is also considerable research done on hydrogen activation on Mo-S, Co-Mo-S and Ni-Mo-S under working conditions. The adsorption of hydrogen on Mo-S was exothermic with high activation barrier while on Co-Mo-S adsorption was exothermic. Ni-S sites were not observed due to their instability. Thus, substitution of promoters helps in creating stable CUS sites.[234] Molecular hydrogen undergoes heterolytic dissociation on Mo-edge to form one Mo-H and S-H pair with E_a = 0.50 eV and two S–H on S-edge with an activation barrier of 1.25 eV.[227] Cobalt was more stable on S-edge while Ni can be present on both Mo-edge and S-edge. A systematic evaluation of the number of S atoms and then of the number of vacancies on the edges for different promoters has not been done yet. Adding cobalt increases the amount of hydrogen present on a catalytic surface.[222]

Sun et al.[230] studied MoS_2 modified with Ni and Co partially or fully under sulfiding conditions. Ni was mostly present on Mo-edge while Co was preferred on the S-edge.[230] For unpromoted MoS_2 at molar ratio of H_2S to H_2 >> 1, fully sulfided Mo-edge and S-edge was obtained. For Ni-Mo-S catalyst, sulfur was only present on Mo atoms and Ni–S was unstable. On the other hand, for Co-Mo-S, Co–S bonds formed if molar ratio of H_2S to H_2 > 0.05 and the most stable structure is bridge S between Mo and Co.[230] Regarding the dissociation of hydrogen on the Ni(Co)Mo catalyst, it was found

that heterolytic dissociation on unpromoted MoS_2 leads to the formation of Mo–H and S–H pairs and Ni-promoted in Mo-edge requires a slightly lower activation energy of 0.04 eV while Co-promoted in an S-edge requires an activation energy of 0.6 eV; however, fully promoted Ni has no sulfur on Mo-edge while fully promoted Co has bridge sulfur on the S-edge.[235-236] On an unpromoted Mo-edge containing bridge S, homolytic dissociation to form two S–H groups is preferred over the Mo-H and S-H pairs and over two Mo–H pairs; however, on unpromoted S-edge, hemolytic dissociation becomes endothermic. For Ni-promoted Mo-edge, the molecular hydrogen dissociation is the rate determining step; however, once dissociated, Ni–H and S–H pairs are very mobile. For Co-promoted on S-edge, dissociation is highly exothermic forming two S–H groups. For Ni-Mo-S, the ability to generate H-species with higher reactivity on the surface, favors the HYD pathway. For Co-Mo-S, cobalt reduces the dissociation energy of hydrogen on the S-edge but dissociated H-species are less mobile and therefore favors HDS over HYD.[235-236]

Adsorption of thiophene and DBT on catalytically active MoS_2 has been studied in great detail. Thiophene was shown to adsorb in the η_5 configuration with thiophenic ring parallel to the Mo-edge. This configuration resulted in the highest adsorption energy and helped in the C–S bond scission.[237] Orita et al.[238] studied adsorption of thiophene on MoS_2 cluster for several adsorption modes using a finite cluster approach, showing that simplification to a $Mo_{16}S_{32}$ cluster is reasonable for examining the adsorption of thiophene due to its correct stoichiometry and electroneutrality without any saturating hydrogen atoms. Thiophene remains flat in the η_1 mode but becomes bent in

other configuration. The adsorption of thiophene required CUS sites on Mo-edge.[238] Faye et al.[239] used a $Mo_{12}S_{24}$ cluster as a model for active phase for adsorption of thiophene.[239] Yang et al.[240] used a $Mo_{10}S_{18}$ cluster to study adsorption of DBT and alkyl substituted DBT as well as their hydrogenated derivatives and showed that flat adsorption is favored over perpendicular adsorption. The adsorption energy increased for a flat adsorption on hydrogenation of phenyl rings while it decreased for perpendicular adsorption due to fewer available sites. Their results showed that DBT and alkyl substituted DBT show similar interaction in flat mode while steric hindrance plays an important role in perpendicular adsorption.[240] Wen et al.[224] studied structure and stability of several MoS_x clusters and showed that $Mo_{16}S_x$ can model S coverage on Mo-edge effectively and the addition of S to Mo-edge was always exothermic. They obtained two stable structures, one with 33% S-coverage and one with 50% coverage on Mo-edge with 100% S on the S-edge. They also obtained one stable structure with 67% S on the S-edge with no S on the Mo-edge.[224] Borges et al.[241] used distributed multipole analysis to study the electronic structure and microwave effects on adsorption of thiophene over a $Mo_{16}S_{32}$ cluster.[241] The HYD and DDS reaction pathways for HDS of thiophene over MoS_2 at both Mo-edge and S-edge under typical reaction conditions were reported using density functional theory and finding that under HDS conditions, the most stable edge configurations correspond to the Mo-edge with 50% S coverage and 50% H coverage and a S-edge with 100% S coverage and 100% H coverage.[242-243] Their work showed that HYD can proceed at Mo-edge even in the absence of CUS Mo sites. The HYD pathways follow hydrogenation of thiophene to form 2-hydrothiophene followed

by hydrogenation to form 2,5-dihydrothiophene and subsequent S–C bond scission while DDS involves the first initial hydrogenation followed directly by S–C scission.[242] Thus, it was predicted the interplay of Mo-edge and S-edge in catalyzing HDS reactions where adsorption and hydrogenation occur at Mo-edge and S–C scission occurs at S-edge. However, vacancies were required at the S-edge for reactions to occur.[242] DBT and alkyl substituted DBT also underwent through two parallel reaction pathways: DDS yielding biphenyl-type compound, or HYD yielding tertrahydro-DBT and cyclohexyl benzene-type products.[244] For DDS pathway, hydrogenation of one double bond in the aromatic ring next to sulfur atom occurred followed by S–C bond scission by elimination process while for HYD successive hydrogenation of one of the aromatic ring occurred followed by S–C bond scission.[244] The role of Ni and Co promoters on HDS of dibenzothiophenes in the presence of H_2S and amines was studied experimentally and the results showed that Ni-promoted MoS_2 catalyst was less sensitive to amine than unpromoted as well as Co-promoted MoS_2 catalyst.[232] The rate of DDS pathway for DBT was dependent on the nature of the catalytic surfaces and increased as Mo << CoMo << NiMo. The higher DDS rate in CoMo was a result of the higher number of S-vacancies available on the S-edge while in Ni-promoted catalyst, the rate of DDS increased significantly due to presence of one free coordination site which can easily adsorb DBT. On the other hand, the HYD pathway of DBT can occur on both S-covered and uncovered Mo, CoMo and NiMo edges, but the reaction was strongly hindered in the presence of amines.[232]

In this work we focus on the removal of thiophene and dibezothiophene (DBT) over both, unpromoted and Ni-promoted MoS_2 catalyst using a finite cluster approach. Efforts have been made to analyze HDS reactions over both pristine MoS_2 as well as under industrial conditions. Since HDS of thiophene has been widely investigated, we use it as control calculations and we focus on the HDS of DBT.

7.2 Methodology

The molecular dynamics simulations of sulfur-containing hydrocarbon oil over MoS_2 catalyst are performed using the Large-scale Atomic/Molecular Massively Parallel Simulator (LAMMPS) program[245]. The hydrocarbon sample is a mixture of 217 n-C15, 369 n-nonylcyclohexane, 130 n-nonylbenzene, 152 naphthalene and 217 thiophene or dibenzothiophene molecules and it corresponds to a specific gravity of ~0.68-0.76 (diesel fraction), sandwiched between two parallel MoS_2 clusters each of $111.89 \times 14.85 \times 95.53$ $Å^3$. The simulation box also contains H_2 molecules distributed randomly in the oil mixture. The initial atomic coordinate file is generated with the Packing Optimization for Molecular Dynamics Simulations (Packmol) program[246]. Periodic boundary conditions (PBC) are applied in all three directions and the system is first minimized at 0 K and then heated to 600 K under the microcanonical NVE ensemble. A cut-off of 10 Å is used for both van der Waals (VdW) and Coulombic interactions. All parameters for bonded and non-bonded interactions are taken from the universal force field (UFF)[247-248]. The charge equilibration method (QEq) is used to determine charges on each atom based on the electronegativity equalization for each

atom as described by Rappe and Goddard[249]. The ionization potentials, electron affinity and atomic radii required for the QEq procedure is obtained from the values given by Rappe et al.[249] Atom velocities are rescaled at every time-step with the Berendsen thermostat[250] within the NVE ensemble to control the temperature. This is followed by equilibration at 600 K for 50 ps with a time-step of 0.05 fs (0.025 fs in case of thiophene) under NVT ensemble. Such a small time step was required for the convergence of charge equilibration procedure. Visualization of trajectories is performed using the graphics software package VMD.[201] A number density plot of thiophene/DBT S and H atoms from H_2 molecule is then generated using the Density Profile Tool[251] available for VMD.

All quantum chemistry calculations are performed using GAUSSIAN-09 Program[252] using density functional theory[253-254] with the hybrid functional B3PW91[255-260]. The LANL2DZ basis-set with effective core potentials[261] is applied for transition elements (Mo, Ni) while 6-31G(d,p) basis-set[262-263] is used for the remaining atoms. Geometry optimization is performed using the Berny method[91-92] with self-consistent field (SCF) convergence threshold of 10^{-6} for the density matrix and 10^{-8} for the RMS and maximum density matrix error respectively. A cluster model for MoS_2 catalyst with formula $Mo_{16}S_{32}$ is employed as suggested by other researchers[238]. The binding energy for adsorption of hydrogen, thiophene, and dibenzothiophene is then calculated from the total energies. Calculations are performed for both unpromoted and Ni-promoted MoS catalysts.

7.3 Results and Discussion

Figure 7.1 provides the initial snapshot of a simulation box containing a hydrocarbon mixture containing thiophene and gaseous hydrogen between two layers of MoS_2 catalyst layers. The catalyst edges exposing Mo-edge without any sulfur and S-edges without any defects were modeled in this simulation. The objective here is to identify the orientations of thiophene molecules with respect to the catalyst edges as well as their locations before the HDS reactions progress.

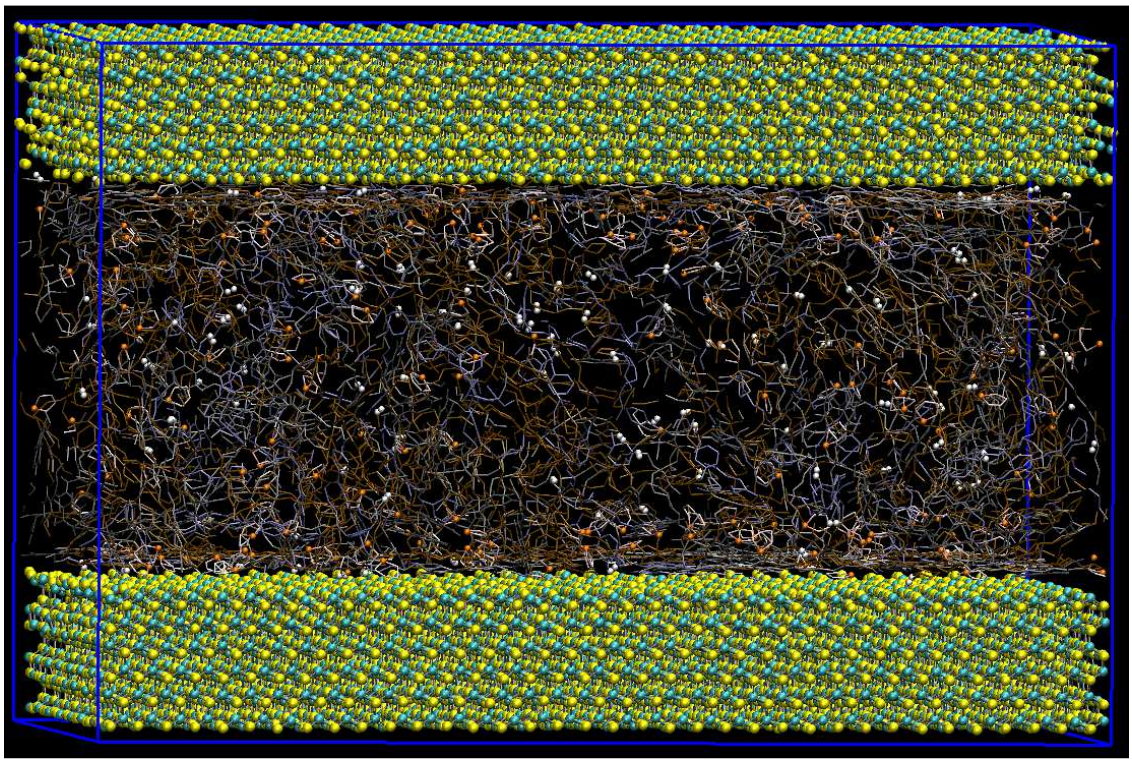

Figure 7.1. Unit cell simulation box for periodic in all three dimensions MD simulations. The unit cell contains 217 n-C15, 369 n-nonylhexane, 130 n-nonylbenzene, 152 naphthalene and 217 DBT, with 108 H_2 molecules sandwiched between two parallel MoS_2 slabs; each MoS_2 slab contains 3456 Mo and 6912 S atoms, making a total of 57515 atoms for the full unit cell.

Following equilibration, we observe that most of the thiophene molecules diffuse from the bulk hydrocarbon oil to the catalyst edges. The density plot of thiophene molecules is shown in Figure 7.4(a) after 50 ps of equilibration at 600 K. The density plot shows two peaks near 2 Å and 5 Å from the catalyst edges indicating reactive sites for thiophene molecules. The thiophene molecules show multiple orientations close to the catalyst edge as observed in Figure 7.2. The temperature and total energy plots during the equilibration are shown in Figure 7.3. The density plot of gaseous hydrogen molecules is shown in Figure 7.4(b). The density maxima are located at 1 Å from the edges. Since we have not considered dissociative adsorption of hydrogen in the molecular dynamics, hydrogen molecules are repelled away from the edges as seen from a wider peak near the middle of the simulation box.

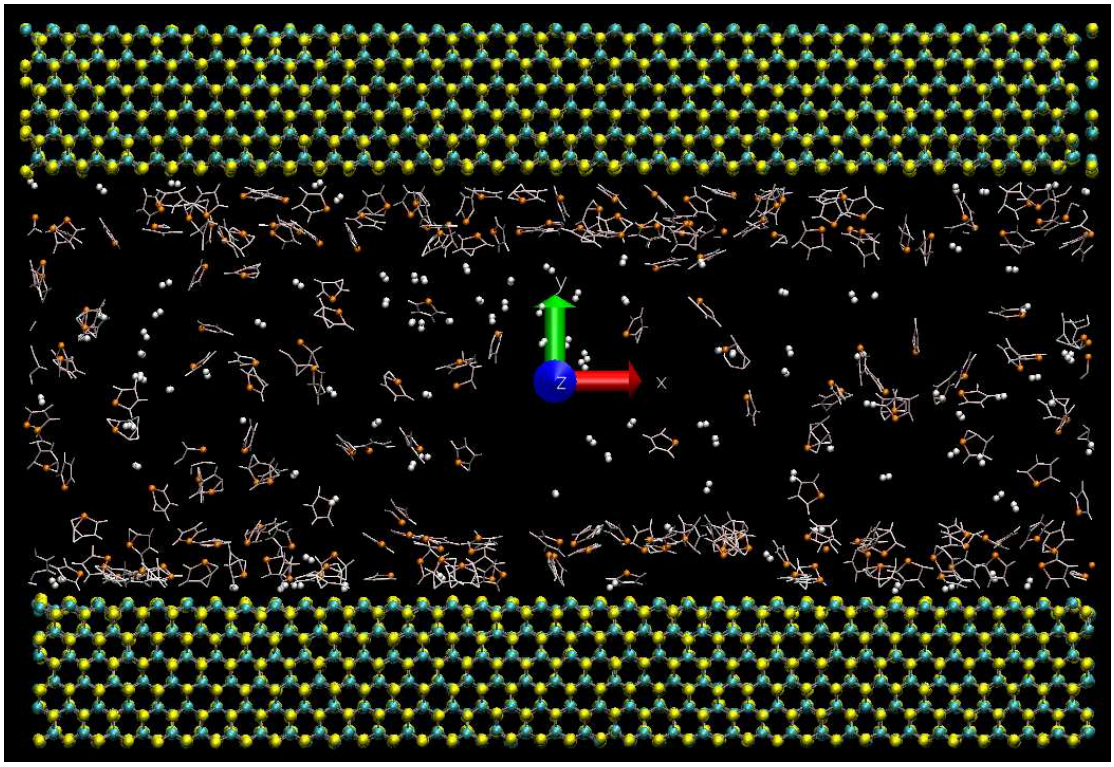

Figure 7.2. Snapshot of equilibrated system showing thiophene and H_2 between the two layers of MoS_2 catalyst using the UFF with charge equilibration. For the sake of clarity the HC oil is not shown.

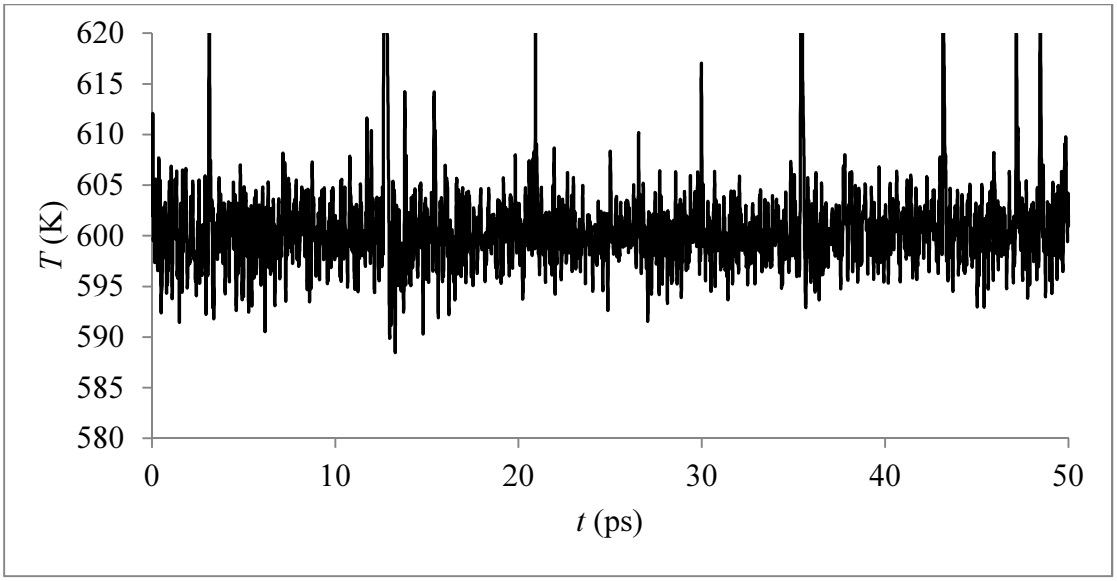

(a)

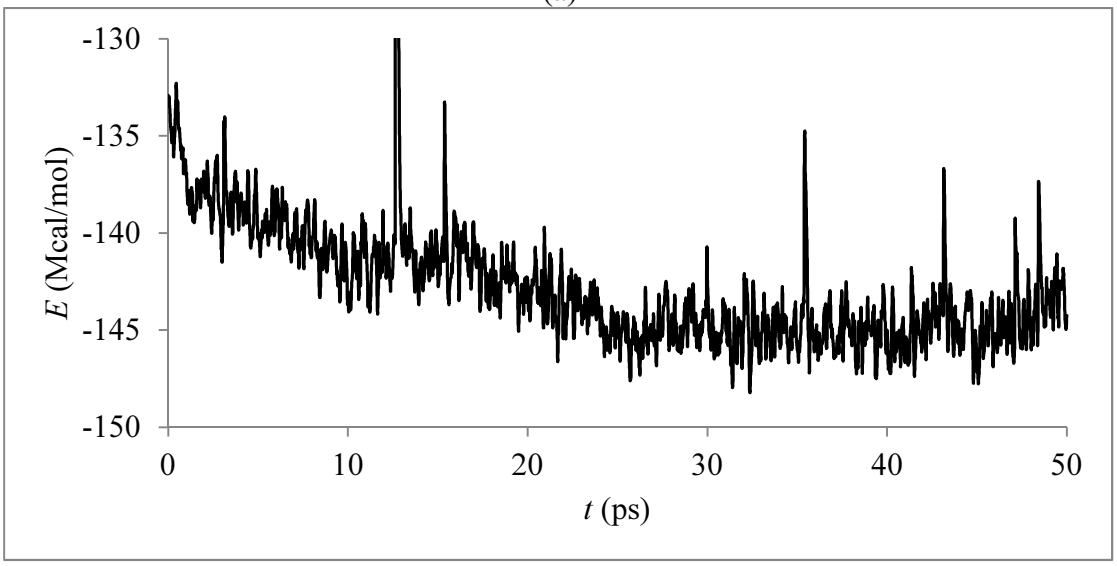

(b)

Figure 7.3. Temperature T (a) and total energy E (b) versus time (t) plot of hydrocarbon mixture between two MoS2 layers as decribed in Figure 7.2.

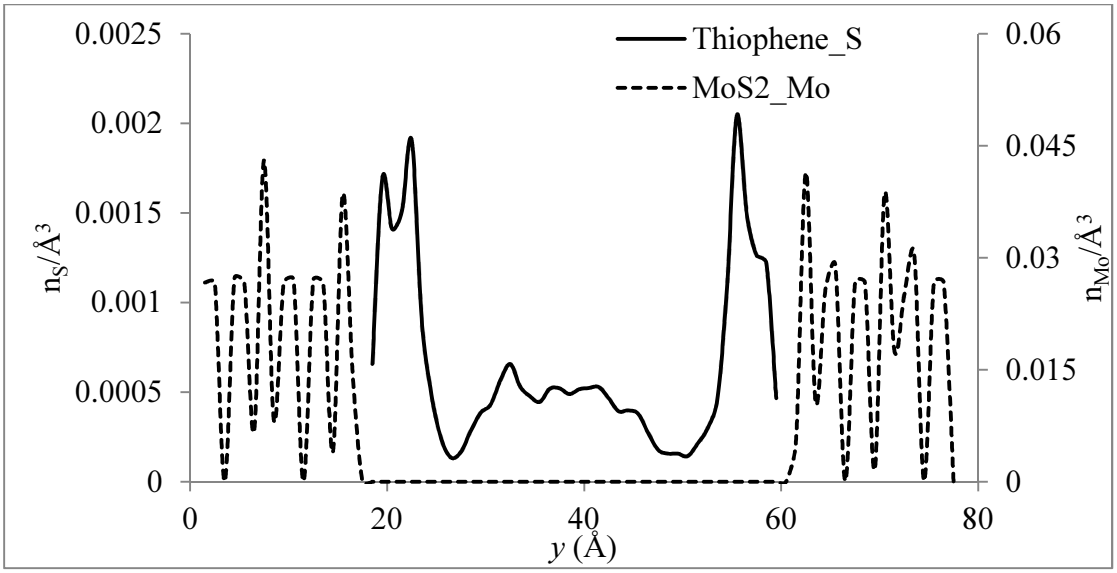

(a)

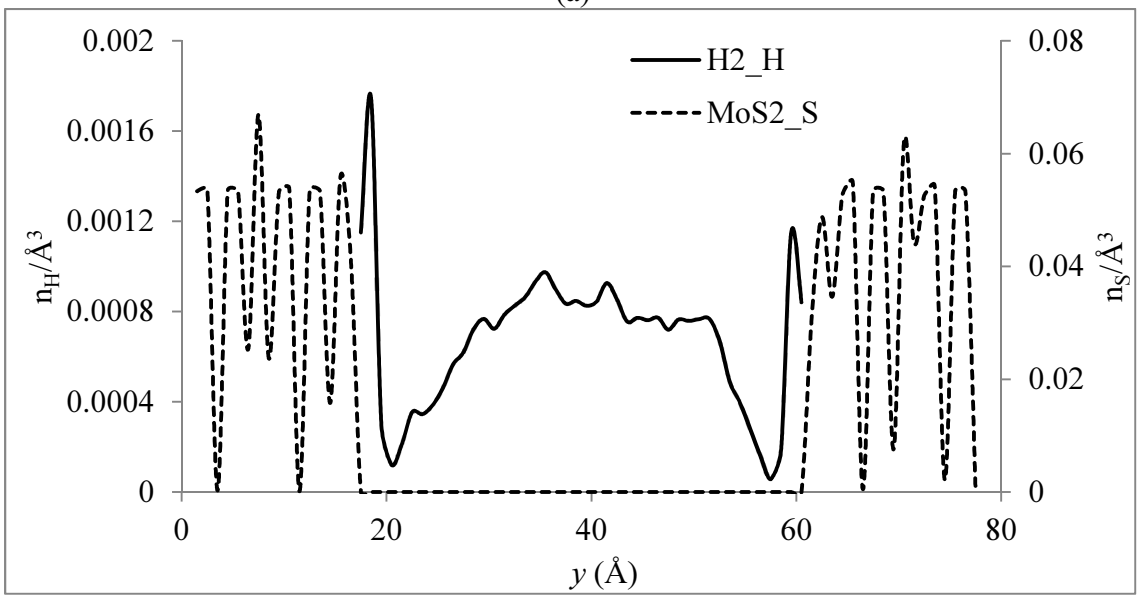

(b)

Figure 7.4. Density n (atoms/Å^3) of (a) S from thiophene and Mo from MoS_2, and (b) H from H_2 and S from MoS_2 (b) along the y axis.

The molecular dynamics of DBT containing hydrocarbon mixture is run along similar procedure as done for thiophene containing oil. Following equilibration at 600 K, we observe that density of the DBT molecules is largest near the edges of MoS_2 clusters

with two peaks at 2 Å and 5 Å respectively (see Figure 7.5). By visual inspection of the orientations of dibenzothiophenes in Figure 7.5, we observe that the DBT molecules closest to the edges are parallel to the surface. However, the peaks are narrower when compared to thiophene as seen in Figure 7.6. However, as the reaction progresses, the catalytic surfaces will be covered by sulfur and hydrogen atoms making parallel adsorption less likely.

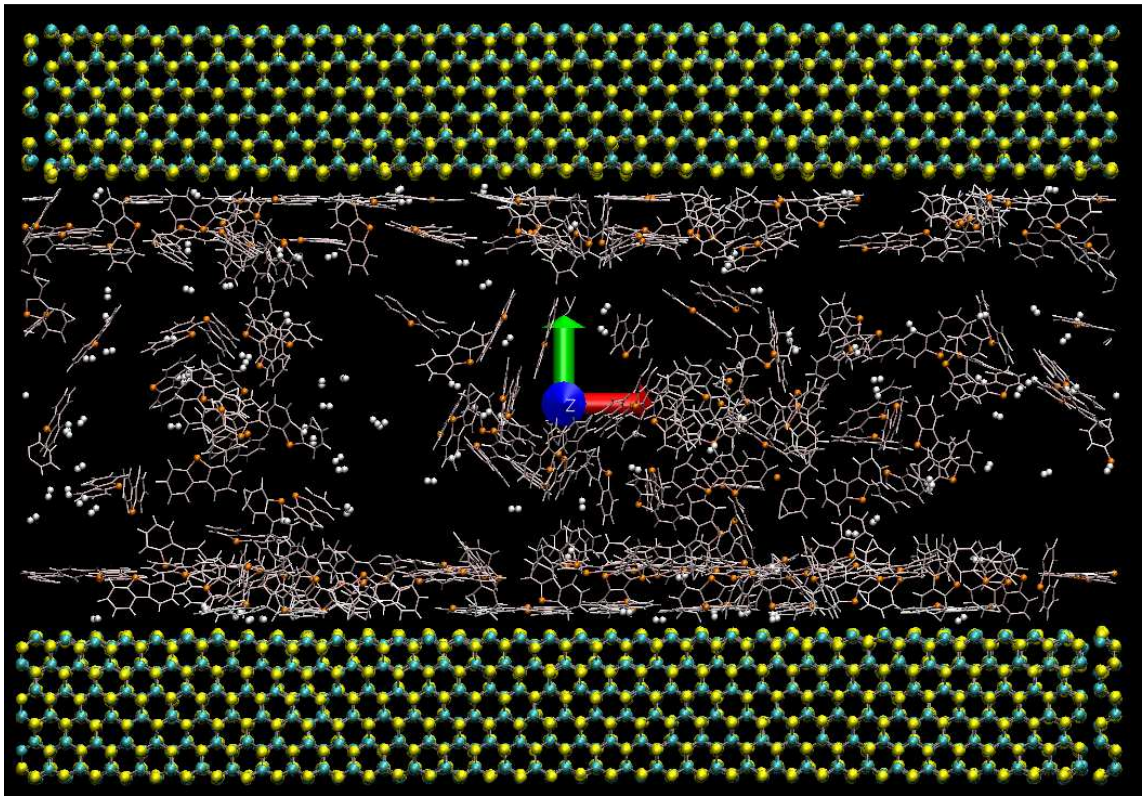

Figure 7.5. Snapshot of equilibrated system showing DBT and H_2 between two layers of MoS_2 catalyst using UFF with charge equilibration. HC oil is not shown for the sake of clarity.

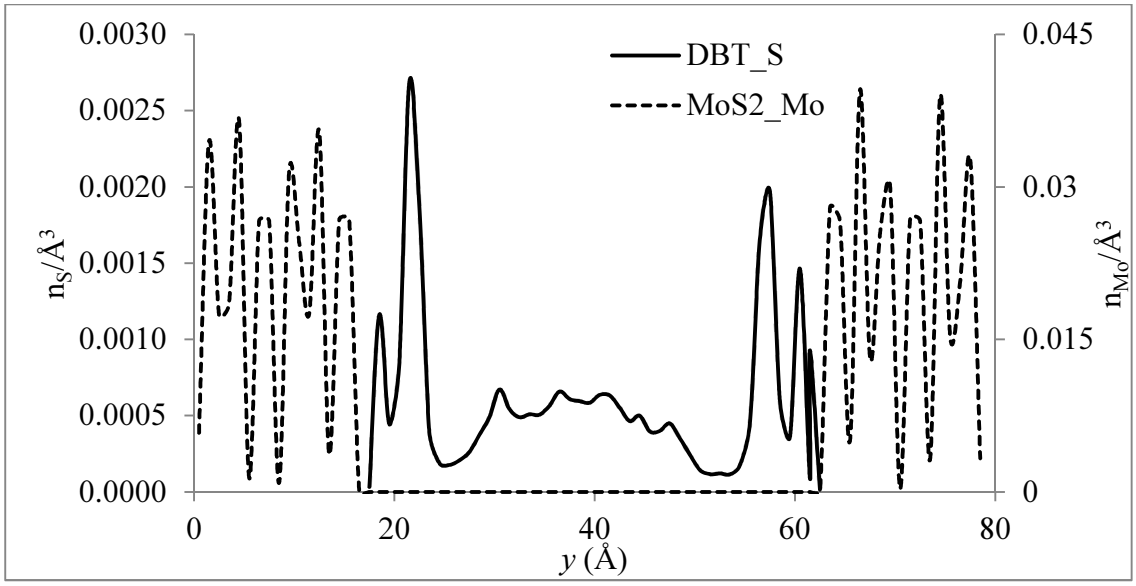

(a)

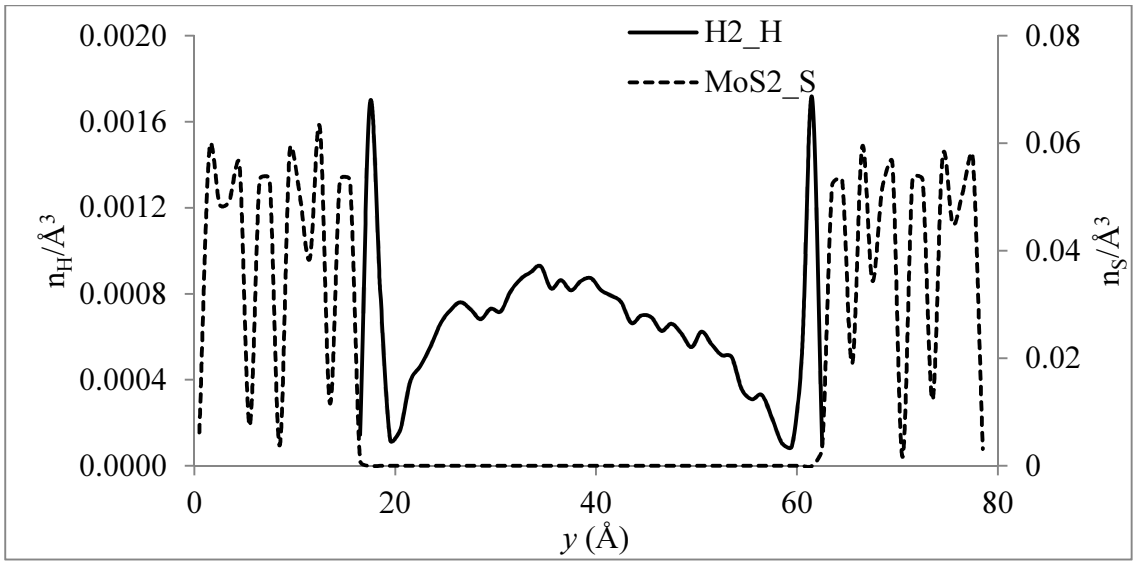

(b)

Figure 7.6. Density n (atoms/$Å^3$) of S from DBT and Mo from MoS_2 (a) and H from H_2 and S from MoS_2 (b) along the y axis (Å).

In order to study specific reaction sites of thiophene with MoS_2 and some of their doped variations, we calculate several of their cluster conformations (Figure 7.7). Most of them are based on variations of basic cluster of $Mo_{16}S_{32}$ to which we have doped with Ni atoms and approached or attached to H_2 or thiophene molecules. As reported in literature, Ni and Co act as promoters and predominantly present on the edge sites. We obtain the optimized geometries of Ni-promoted MoS_2 clusters for both partially promoted and fully promoted cases. Pristine MoS_2 yields the strongest binding to thiophene when interacting with two Mo in parallel adsorption mode (see Table 7.1). This bonding strongly reduces ~60% when the interaction is to only one Mo in perpendicular adsorption mode. Adding promoters further weakens these interactions as the calculated binding energies decreases further as shown in Table 7.1. However, it has already been shown by other researchers that pristine form of MoS_2 clusters is less likely to be present under reaction conditions. Therefore we also obtain the optimized structures of MoS_2 clusters with sulfur atoms present on the Mo-edge to study the adsorption of thiophene. Our calculations show that S-vacancies are necessary on Mo-edge to create coordinately unsaturated sites for adsorption of thiophene as can be seen from close to zero value of binding energy. Since the reactions occur in an atmosphere of H_2 and H_2S, these vacancies will be continuously created and destroyed. The most stable Mo-edge under reaction conditions was shown to contain three S atoms in bridging positions.[226,228-230] In order to create a single S-vacancy, we remove one S atom from the Mo-edge and re-optimize the structure for both unpromoted and Ni-promoted clusters. It is also interesting to note that when promoted with Ni, S atoms are only

present on the Mo atoms which is understandable since Ni-S bonds are less stable as reported earlier.[234] The binding energies of adsorption of thiophene on sulfur-containing Mo-edges are much smaller than those of pristine Mo-edges.

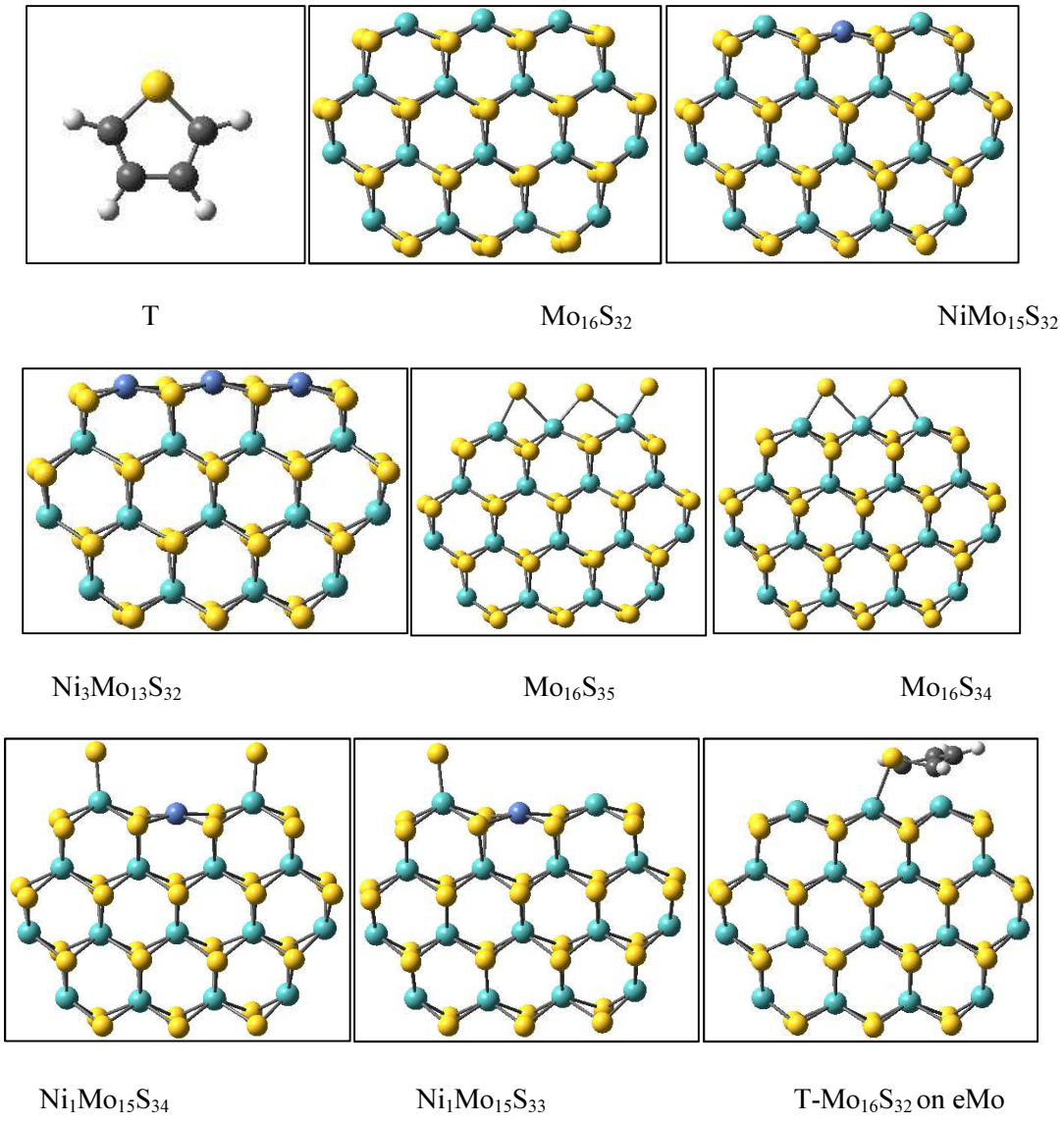

Figure 7.7. Adsorption of thiophene (T) on unpromoted and Ni-promoted $Mo_{16}S_{32}$ clusters. Binding energies with thiophene inside parentheses**:** Mo(cyan), C(grey), S(yellow), Ni(blue), and H(white).

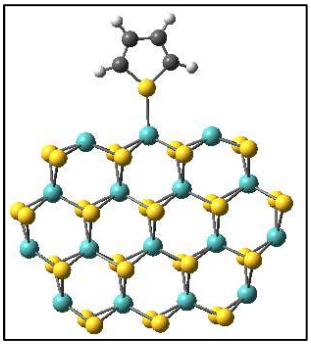

T-$Mo_{16}S_{32}$ on eMo

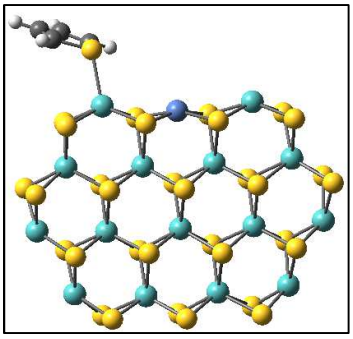

T-$Ni_1Mo_{15}S_{32}$ on pNi eMo

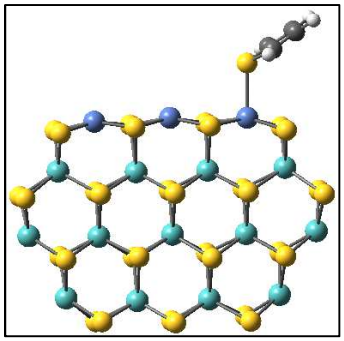

T-$Ni_3Mo_{13}S_{32}$ on pNi eMo

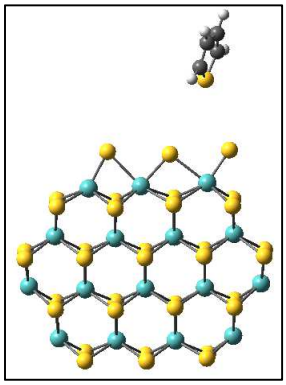

T--- $Mo_{16}S_{35}$ on eMo

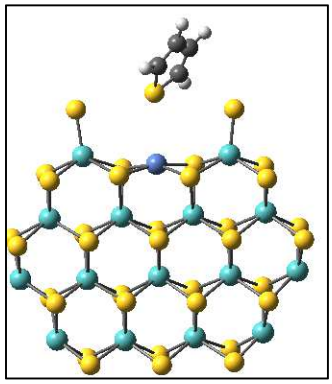

T--- $Ni_1Mo_{15}S_{34}$ on pNi eMo

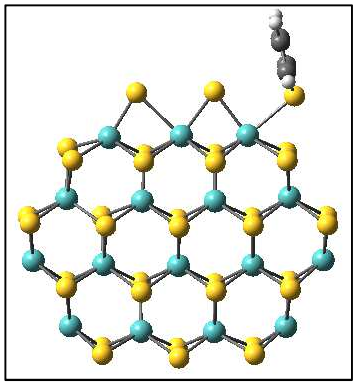

T-$Mo_{16}S_{34}$ on eMo

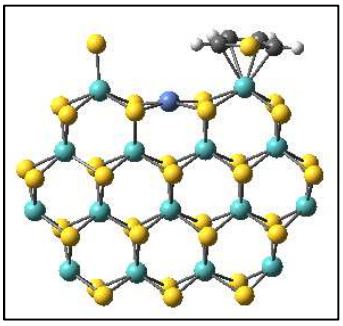

T-$Ni_1Mo_{15}S_{33}$ on pNi eMo

Figure 7.7 Continued.

Table 7.1. Total (*E*) and Binding Energies (*D*) of Thiophene and MoS_2 Clusters at the B3PW91/LANL2DZ/6-31G(*d*,*p*) Level of Theory

Complex	*E* (Hartree)	*D* (eV)
Thiophene (T)	-552.89741	
$Mo_{16}S_{32}$	-13823.38206	
$NiMo_{15}S_{32}$	-13925.15425	
$Ni_3Mo_{13}S_{32}$	-14128.68166	
$Mo_{16}S_{35}$	-15018.01421	
$Mo_{16}S_{34}$	-14619.85984	
$Ni_1Mo_{15}S_{34}$	-14721.59832	
$Ni_1Mo_{15}S_{33}$	-14323.37740	
T-$Mo_{16}S_{32}$ on eMo	-14376.38136	-2.77
T-$Mo_{16}S_{32}$ on eMo	-14376.31897	-1.07
T-$Ni_1Mo_{15}S_{32}$ on pNi eMo	-14478.08712	-0.97
T-$Ni_3Mo_{13}S_{32}$ on pNi eMo	-14681.60426	-0.69
T--- $Mo_{16}S_{35}$ on eMo	-15570.91201	-0.01
T--- $Ni_1Mo_{15}S_{34}$ on pNi eMo	-15274.49576	0.0
T-$Mo_{16}S_{34}$ on eMo	-15172.77806	-0.57
T-$Ni_1Mo_{15}S_{33}$ on pNi eMo	-14876.34697	-1.96

Since the HDS reactions are carried out in the presence of hydrogen, it is equally important to study the activation of hydrogen on MoS_2 clusters and the role of promoters on the nature of catalytic surface present under reaction conditions. Gaseous hydrogen can get adsorbed on Mo-edge activating the H–H bond as indicated by increases in bond length from 0.73 Å to 0.86 Å. Hydrogen atoms once dissociated can adsorb on Mo-edge and S-edge as well as the corner sites as shown in Figure 7.8. Our calculations show that hydrogen undergoes dissociative adsorption on both Mo-edge and S-edge forming a variety of surfaces. The adsorption is most exothermic in case of Mo-edge and least on

S-edge as shown in Table 7.2. When Mo-edge is partially promoted by nickel atoms, the exothermicity of the reaction decreases and becomes endothermic when the Mo-edge is fully promoted by nickel atoms as there are no Mo atoms available for Mo–H formation. Hydrogen plays a key role in creation of S-vacancies in addition to directly participate in HDS reactions. Similarly, H_2S can also be adsorbed on Mo-edges when sulfur vacancies are present. The reaction changes from exothermic to endothermic when nickel atoms are present as promoters.

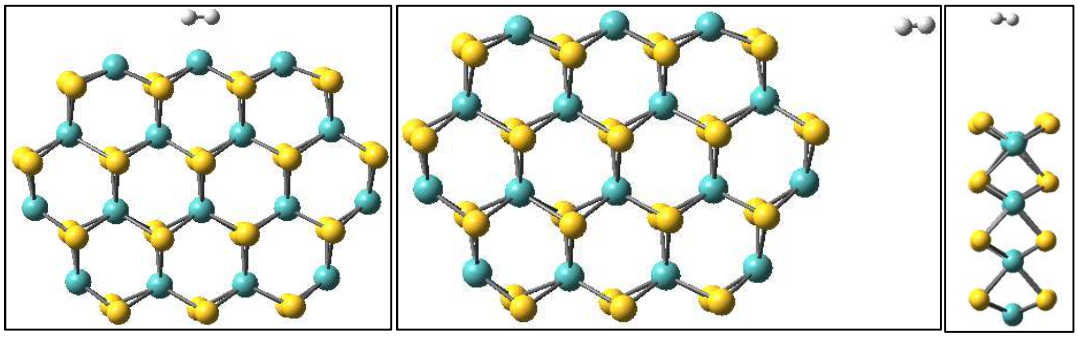

H_2-$Mo_{16}S_{32}$ on eMo H_2---$Mo_{16}S_{32}$ on c H_2---$Mo_{16}S_{32}$ on eS

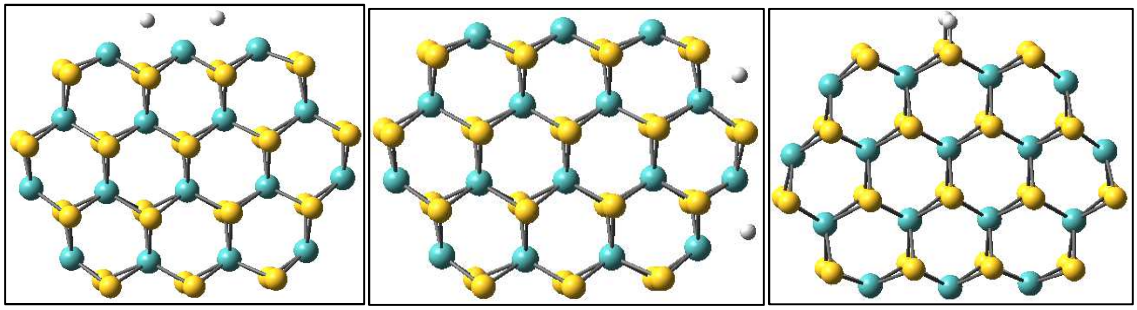

2H-$Mo_{16}S_{32}$ on eMo 2H- $Mo_{16}S_{32}$ on c 2H-$Mo_{16}S_{32}$ on eS

Figure 7.8. Adsorption of H_2 (binding energy 4.71 eV) and H_2S on unpromoted and Ni-promoted $Mo_{16}S_{32}$ clusters $Mo_{16}S_{32}$. Catalytic sites are indicated by e = edge, c= corner, p = promoted, and "-" indicates bonded and "---" indicates nonbonded. Color coding follows Mo(cyan), C(grey), S(yellow), Ni(blue), and H(white).

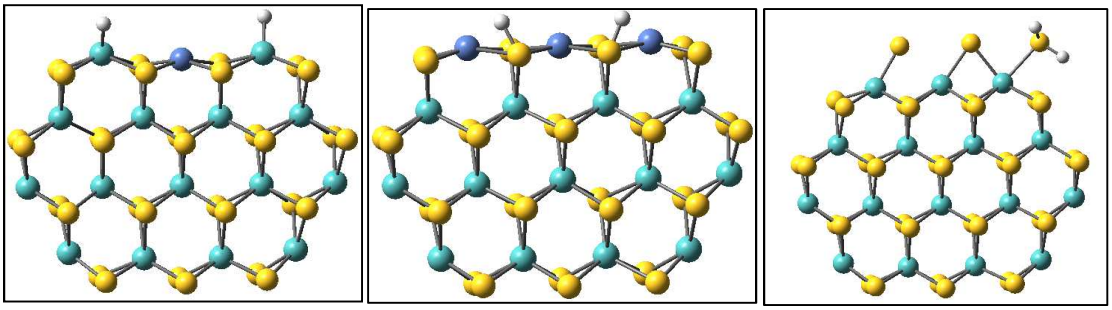

2H-$Ni_1Mo_{15}S_{32}$ on pNi eMo 2H-$Ni_3Mo_{13}S_{32}$ on pNi eMo H_2S- $Mo_{16}S_{34}$ on eMo

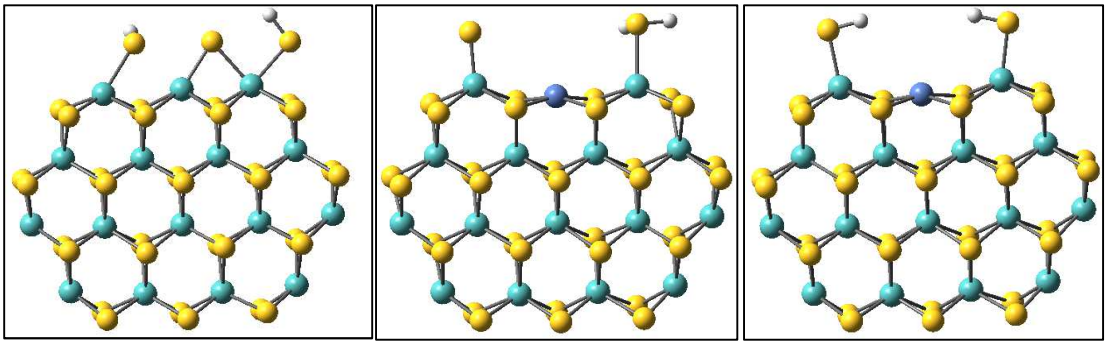

2SH- $Mo_{16}S_{33}$ on eMo H_2S-$Ni_1Mo_{15}S_{33}$ on pNi eMo 2SH-$Ni_1Mo_{15}S_{32}$ on pNi eMo

Figure 7.8 Continued.

Table 7.2. Energy (E) and Binding Energy of H_2 and H_2S Adsorption (D) on $Mo_{16}S_{32}$ Clusters at the B3PW91/LANL2DZ/6-31G(*d*,*p*) Level of Theory

Complex	E(Hartree)	D (eV)
H_2	-1.17752	-4.71
H_2-$Mo_{16}S_{32}$ on eMo	-13824.58490	-0.69
H_2---$Mo_{16}S_{32}$ on c	-13824.55957	0.00
H_2---$Mo_{16}S_{32}$ on eS	-13824.55957	0.0
2H-$Mo_{16}S_{32}$ on eMo	-13824.59853	-1.06
2H-$Mo_{16}S_{32}$_H_2 on c	-13824.58580	-0.71
2H-$Mo_{16}S_{32}$_H_2 on eS	-13824.57564	-0.44
2H-$Ni_1Mo_{15}S_{32}$ on pNi eMo	-13926.35418	-0.61
2H-$Ni_3Mo_{13}S_{32}$ on pNi eMo	-13824.57564	0.32

Table 7.2 Continued.

Complex	E(Hartree)	D (eV)
H_2S-$Mo_{16}S_{34}$ on eMo	-15019.22969	-1.03
2SH-$Mo_{16}S_{33}$ on eMo	-15019.21452	-0.62
H_2S-$Ni_1Mo_{15}S_{33}$ on pNi eMo	-14722.75808	0.48
2SH-$Ni_1Mo_{15}S_{32}$ on pNi eMo	-14722.75898	0.46

We study next the HDS reactions of thiophene over MoS_2 clusters. Thiophene can undergo both hydrogenation (HYD) as well as direct desulfurization (DDS) pathway for HDS reaction. We focus on both parallel and perpendicular adsorption modes of thiophene. Thiophene once adsorbed on MoS_2 cluster undergoes successive hydrogenation to form 2-hydrothiophene and 2,5-dihydrothiophene. We obtained the binding energy for each case on pristine MoS_2 cluster (Table 7.3). The HYD mechanism follows S–C bond scission following the formation of 2,5-dihydrothiophene by hydride-shift while DDS follows S–C scission immediately after formation of 2-hydrothiophene. The binding energy of final products are also calculated and presented in Table 7.3. The binding energy of adsorption of reaction intermediates of thiophene HDS are higher for parallel adsorption and increases as the reaction progresses. For perpendicular adsorption mode, Mo–S bond length decreases initially from 2.37 Å to 2.31 Å in case of 2-hydrothiophene but again increases to 2.38 Å. The Mo–S bond length further increases to 2.43 Å during C–S bond scission. However in case of parallel adsorption, Mo–S bond length decreases from 2.48 Å to 2.39 Å on C–S bond scission. In some cases (see Figure 7.9), we observe adsorption of H atoms directly to the Mo-edge. However, since

hydrogen is continuously supplied to the reaction system, other hydrogen atoms can initiate the HDS reactions via HYD or DDS pathway. The role of promoters and nature of catalytic edges in HDS of thiophene has been studied already in great detail; we focus on these effects on HDS of DBT molecules later on in the manuscript.

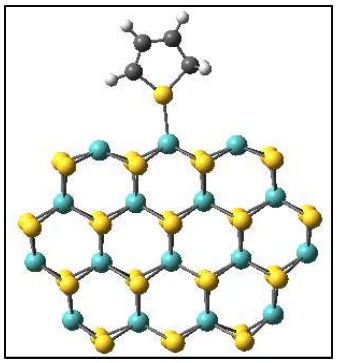

C_4H_5S-$Mo_{16}S_{32}$ on eMo

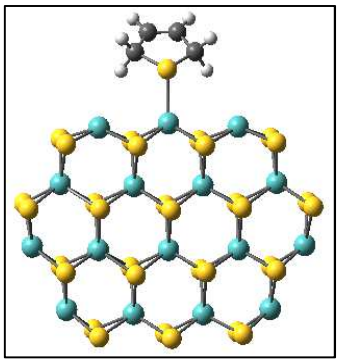

C_4H_6S-$Mo_{16}S_{32}$ on eMo

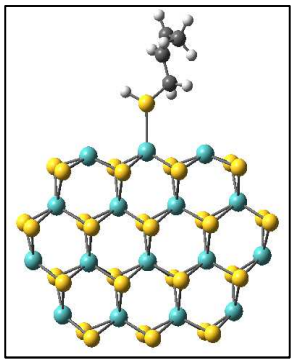

C_4H_7SH-$Mo_{16}S_{32}$ on eMo

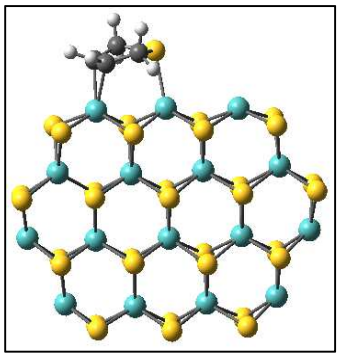

C_4H_6S-$Mo_{16}S_{32}$ on eMo

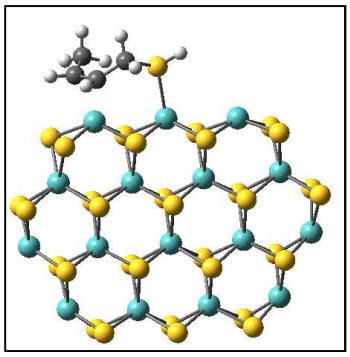

C_4H_7SH-$Mo_{16}S_{32}$ on eMo

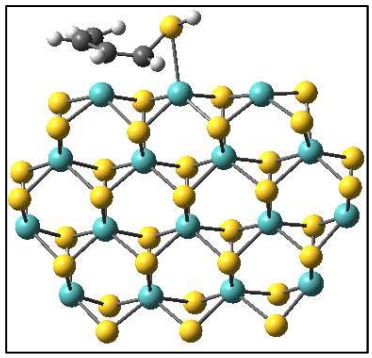

C_4H_5SH-$Mo_{16}S_{32}$ on eMo

Figure 7.9. Reaction intermediates formed during hydrogenation and direct desulfurization pathways of thiophene after adsorption on $Mo_{16}S_{32}$ clusters. Mo(cyan), C(grey), S(yellow), B (pink), Ni(blue), and H(white).

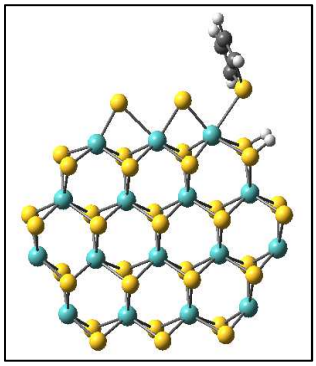

T-$Mo_{16}S_{33}(SH)_2$ on eMo

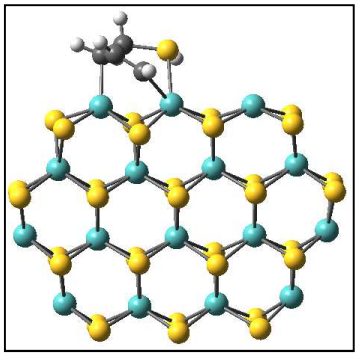

C_4H_5SH-$Mo_{16}S_{32}$ on eMo

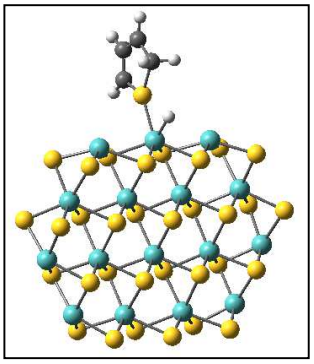

C_4H_5S-$Mo_{16}S_{32}H$ on eMo

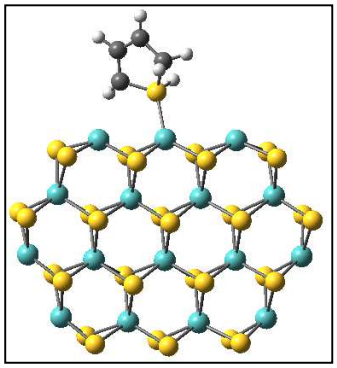

C_4H_5SH-$Mo_{16}S_{32}$ on eMo

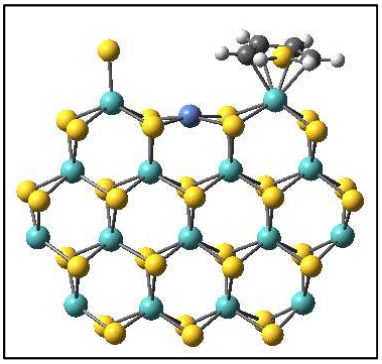

C_4H_6S-$Ni_1Mo_{15}S_{33}$ on pNi eMo

Figure 7.9 Continued.

Table 7.3. Energy (E) and Binding Energy (D) of Reaction Intermediates Formed during HYD/DDS of Thiophene on $Mo_{16}S_{32}$ Clusters at the B3PW91/LANL2DZ/6-31G(*d*,*p*) Level of Theory

Complex	E(Hartree)	D (eV)
C_4H_5S-$Mo_{16}S_{32}$ on eMo	-14376.92649	-2.12
C_4H_6S-$Mo_{16}S_{32}$ on eMo	-14377.54524	-1.66
C_4H_7SH-$Mo_{16}S_{32}$ on eMo	-14378.74467	-1.68
C_4H_6S-$Mo_{16}S_{32}$ on eMo	-14377.59205	-2.94
C_4H_7SH-$Mo_{16}S_{32}$ on eMo	-14378.79312	-3.00
C_4H_5SH-$Mo_{16}S_{32}$ on eMo	-14377.58055	-3.53

Table 7.3 Continued.

Complex	E(Hartree)	D (eV)
T-$Mo_{16}S_{33}(SH)_2$ on eMo	-15173.97291	-1.04[a]
C_4H_5SH-$Mo_{16}S_{32}$ on eMo	-14377.57111	-3.11[a]
C_4H_5S-$Mo_{16}S_{32}H$ on eMo	-14377.49337	-0.99[a]
C_4H_5SH-$Mo_{16}S_{32}$ on eMo	-14377.43415	-1.99[a]
C_4H_6S-$Ni_1Mo_{15}S_{33}$ on pNi eMo	-14877.42608	2.68[a]

[a] The binding energy is the difference between total energy of products and sum of total energy of each reactant molecule in these cases.

In order to reduce costs of desulfurization processes, it is imperative to develop new chemistries to improve efficiency of the catalyst. A favorable effect was observed when MoS_2 and graphene were combined together in the electrocatalytic process for generation of hydrogen in fuel cells.[214] In HDS process, γ-alumina is the most commonly used support material for MoS2 catalysts. The γ-alumina support tends to form Mo–O–Al linkages which then require higher sulfiding temperature which can cause sintering effects leading to loss of catalytic activity. Graphene on the other hand does not form such linkages and the plasmonic properties of graphene can be exploited to improve the selectivity and sensing properties of MoS_2 clusters. Boron nitride (BN) also form hexagonal monolayer like graphite and can be used to tune the electronic properties of the MoS_2 cluster. Hence, we study the effect of graphene and BN on the catalytic activities of MoS_2 cluster by calculating the change in adsorption binding energy of thiophene. The MoS_2/graphene and MoS_2/BN complexes with and without adsorbed thiophene are shown in Figure 7.10. MoS_2 cluster undergo physisorption on both BN and

graphene monolayers. The interaction between MoS_2 cluster and graphene is stronger than that between MoS_2 cluster and BN monolayer as observed from higher binding energy (see Table 7.4) as well as the inter-planar distance (Figure 7.10) between the clusters and individual BN and graphene monolayers. We also calculated the adsorption binding energy of thiophene as a test molecule on MoS_2/graphene and MoS_2/BN complexes. The adsorption binding energy of thiophene changes from -2.77 eV (parallel adsorption) and -1.07 eV (perpendicular adsorption) for pristine MoS2 cluster to -2.41 eV and -1.02 eV respectively in case of MoS_2/graphene complex. The Mo–S bond length also increases from 2.58 Å (parallel adsorption) and 2.37 Å (perpendicular adsorption) for pristine MoS2 cluster to 2.66 Å and 2.39 Å respectively in case of MoS2/graphene complex. On the other hand, BN has no such effect on adsorption energetics of thiophene. The binding energy for perpendicular adsorption of thiophene however increased in case of MoS_2/BN complex, but the Mo–S bond length (2.38Å) remain more or less unchanged.

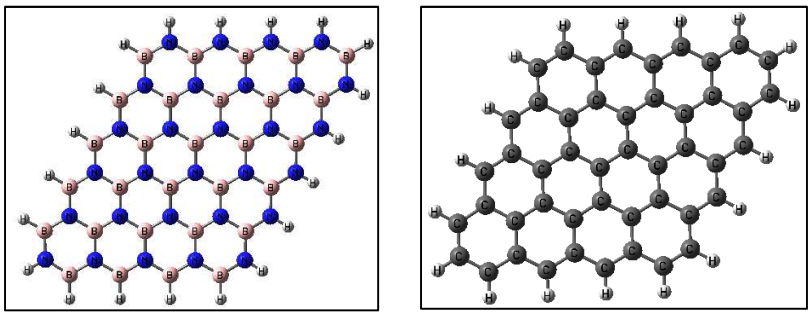

$B_{29}N_{29}H_{29}$ (BN) $C_{58}H_{18}$ (G)

Figure 7.10. Adsorption of thiophene (T) on BN promoted $Mo_{16}S_{32}$ clusters. Mo(cyan), C(grey), S(yellow), B (pink), N(dark blue), and H(white).

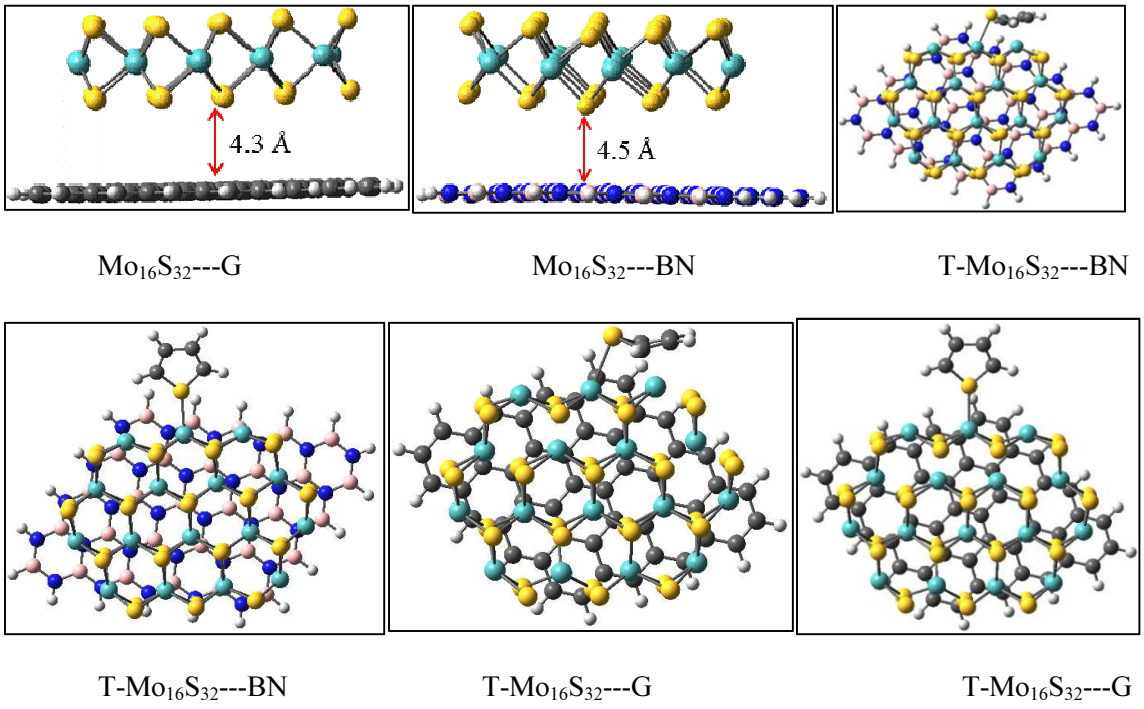

Figure 7.10 Continued.

Table 7.4. Total (E) and Binding (D) Energy of MoS_2 Clusters at the B3PW91/LANL2DZ/6-31G(*d*,*p*)

Complex	E (Hartree)	D (eV)
$B_{29}N_{29}H_{29}$ (BN)	-2322.81462	
$C_{58}H_{18}$ (G)	-1839.49751	
$Mo_{16}S_{32}$---BN	-16146.20110	-0.13
$Mo_{16}S_{32}$---G	-15662.89156	-0.33
T-$Mo_{16}S_{32}$---BN	-16699.20030	-2.76
T-$Mo_{16}S_{32}$---BN	-16699.14020	-1.14
T-$Mo_{16}S_{32}$---G	-16215.87753	-2.41
T-$Mo_{16}S_{32}$---G	-16215.82658	-1.02

We now focus on the the adsorption and HDS mechanism of DBT on both pristine and Ni-promoted MoS_2 clusters. Attempts are also made to represent the reactions occuring under reaction conditions. DBT can adsorb on Mo-edge using both thiophinic ring and phenyl ring depending on available sites as shown in Figure 7.11. The binding energy of adsorption is higher when phenyl ring also interacts with Mo atoms present on the Mo-edge as indicated in Table 7.5. The calculated Mo–S bond length for pristine, sulfur-covered and Ni-promoted MoS_2 clusters are 2.45 Å, 2.63 Å and 2.42 Å respectively. The binding energy is largest in the case of pristine MoS_2 cluster and least when Mo-edge is covered with sulfur atoms.

Table 7.5. Total (*E*) and Binding Energies (*D*) of Dibenzothiophene (DBT) and MoS_2 Clusters at the B3PW91/LANL2DZ/6-31G(*d*,*p*) Level of Theory

Complex	*E* (Hartree)	*D* (eV)
DBT	-860.08575	
$Mo_{16}S_{32}$	-13823.38206	
DBT-$Mo_{16}S_{32}$ (A)	-14683.51890	-1.39
DBT-$Mo_{16}S_{32}$ (B)	-14683.53376	-1.79
DBT-$Mo_{16}S_{34}$	-15479.97198	-0.72
DBT-$Ni_1Mo_{15}S_{33}$	-15183.50790	-1.22

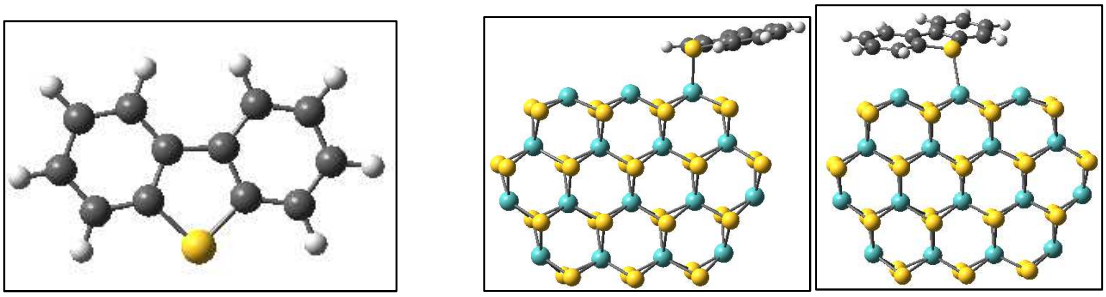

DBT DBT-$Mo_{16}S_{32}$ (A) DBT-$Mo_{16}S_{32}$ (B)

DBT-$Mo_{16}S_{34}$ DBT-$Ni_1Mo_{15}S_{33}$ on pNi eMo

Figure 7.11. Adsorption of dibenzothiophene (DBT) on unpromoted and Ni-promoted $Mo_{16}S_{32}$ clusters. Binding energies with thiophene inside parentheses**:** Mo(cyan), C(grey), S(yellow), Ni(blue), and H(white).

In order to study the two reaction pathways (HYD and DDS), we chose three types of MoS_2 clusters representing different reaction conditions and nature of surface. When S atoms are present on the Mo-edge, we created a single S-vacancy to create coordinately unsaturated sites for adsorption and successive reaction steps of the HDS of DBT. Like thiophene, DBT undergoes hydrogenation to form 2,3-dihydrodibenzothiophene. The Mo–S bond length remains unchanged within ±0.01 Å for pristine and Ni-promoted MoS_2 clusters on hydrogenation. In case of sulfur-covered Mo-edge, Mo–S bond length reduces by 0.03 Å on hydrogenation. Once hydrogenated, DBT

can undergo successive hydrogenation along HYD pathway or undergo S–C scission along DDS pathway. The binding energy increases as the phenyl ring undergoes successive hydrogenation for all three types of clusters. During HYD pathway, DBT can undergo further hydrogenation of phenyl ring or undergo S–C bond scission leading to mixture of products. On the other hand, DDS of DBT leads to biphenyl as final product.[244]

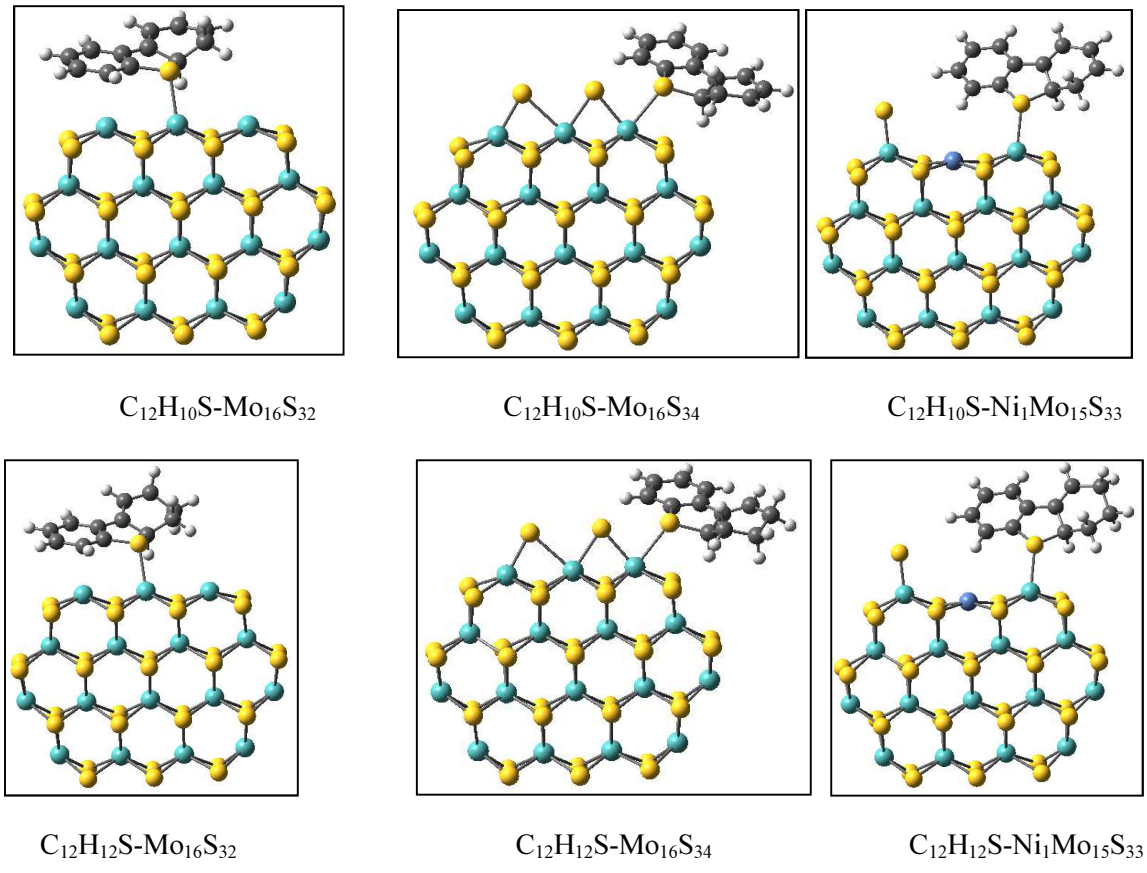

Figure 7.12. Hydrogenation and direct desulfurization pathways of DBT after adsorption on $Mo_{16}S_{32}$ clusters: prehydrogenation of phenyl ring (a-c), second hydrogenation step (d-f), C-S bond scission in HYD (g-i), C–S bond scission in DDS pathway following prehydrogenation step. Mo(cyan), C(grey), S(yellow), B (pink), Ni(blue), and H(white).

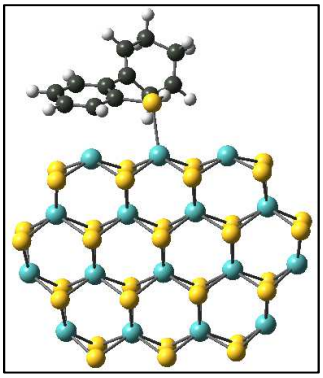

$C_{12}H_{11}SH\text{-}Mo_{16}S_{32}$

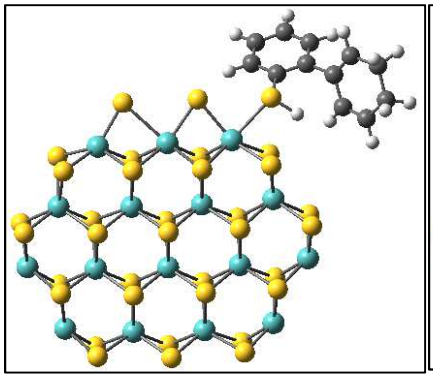

$C_{12}H_{11}SH\text{-}Mo_{16}S_{34}$

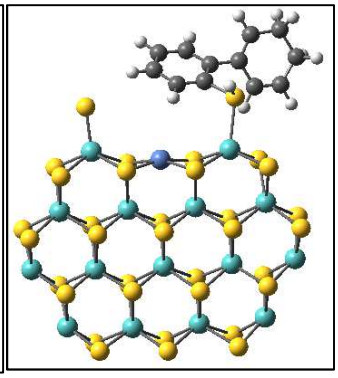

$C_{12}H_{11}SH\text{-}Ni_1Mo_{15}S_{33}$

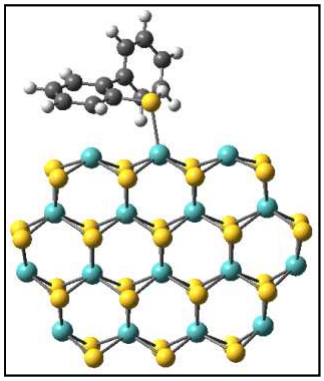

$C_{12}H_9SH\text{-}Mo_{16}S_{32}$

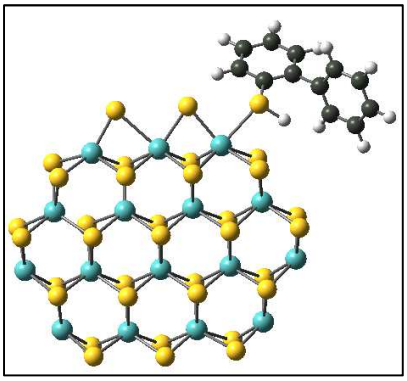

$C_{12}H_9SH\text{-}Mo_{16}S_{34}$

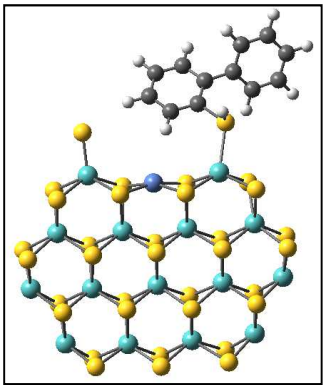

$C_{12}H_9SH\text{-}Ni_1Mo_{15}S_{33}$

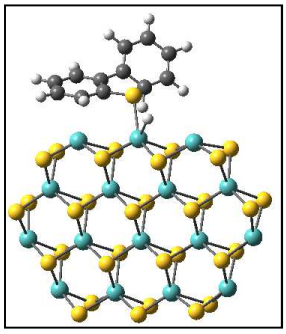

$C_{12}H_9S\text{-}Mo_{16}S_{32}H$

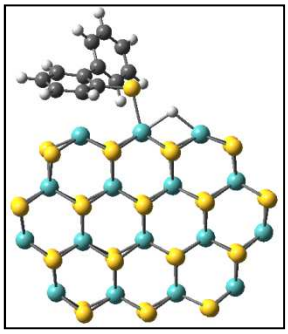

$C_{12}H_9S\text{-}Mo_{16}S_{32}H$

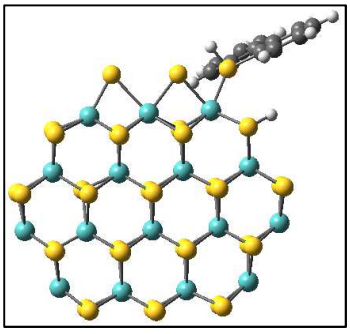

$C_{12}H_8SH\text{-}Mo_{16}S_{34}H$

Figure 7.12 Continued

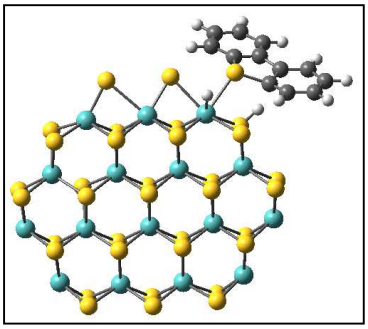

$C_{12}H_8$-$Mo_{16}S_{34}H_2$

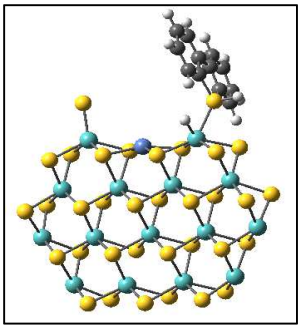

$C_{12}H_8SH$-$Ni_1Mo_{15}S_{33}H$

Figure 7.12 Continued.

Table 7.6. Energy (*E*) and Adsorption Binding Energy (*D*) of Reaction Intermediates Formed During HYD/DDS of DBT on $Mo_{16}S_{32}$ Clusters at the B3PW91/LANL2DZ/6-31G(*d*,*p*) Level of Theory

Complex	*E*(Hartree)	*D*(eV)
$C_{12}H_{10}S$-$Mo_{16}S_{32}$	-14684.71150	-2.07
$C_{12}H_{10}S$-$Mo_{16}S_{34}$	-15481.15141	-1.04
$C_{12}H_{10}S$-$Ni_1Mo_{15}S_{33}$	-15184.68600	-1.51
$C_{12}H_{12}S$-$Mo_{16}S_{32}$	-14685.94496	-2.14
$C_{12}H_{12}S$-$Mo_{16}S_{34}$	-15482.38362	-1.08
$C_{12}H_{12}S$-$Ni_1Mo_{15}S_{33}$	-15185.91935	-1.57
$C_{12}H_{11}SH$-$Mo_{16}S_{32}$	-14685.90314	-2.10
$C_{12}H_{11}SH$-$Mo_{16}S_{34}$	-15482.34015	-0.99
$C_{12}H_{11}SH$-$Ni_1Mo_{15}S_{33}$	-15185.87351	-1.42
$C_{12}H_9SH$-$Mo_{16}S_{32}$	-14684.72455	-2.04
$C_{12}H_9SH$-$Mo_{16}S_{34}$	-15481.16172	-0.94
$C_{12}H_9SH$-$Ni_1Mo_{15}S_{33}$	-15184.68948	-1.22
$C_{12}H_9S$-$Mo_{16}S_{32}H$	-14684.71430	-1.88[a]
$C_{12}H_9S$-$Mo_{16}S_{32}H$	-14684.75806	-3.07[a]
$C_{12}H_8SH$-$Mo_{16}S_{34}H$	-15481.11273	0.28[a]
$C_{12}H_8$-$Mo_{16}S_{34}H_2$	-15481.11577	0.20[a]

Table 7.6 Continued.

Complex	*E*(Hartree)	*D*(eV)
$C_{12}H_8SH\text{-}Ni_1Mo_{15}S_{33}H$	-15184.64031	0.01[a]

[a]The binding energy is the difference between total energy of products and sum of total energy of each reactant molecule in these cases.

7.4 Conclusions

Molecular dynamics performed on hydrocarbon mixture containing thiophenes and dibenzothiophenes show that these sulfur-compunds diffuses from bulk to the MoS_2 catalytic edges. MoS_2/graphene complex shows improvement over pristine MoS_2 cluster for adsorption of thiophene. A comprehensive analysis of HDS reaction mechanism has been presented using $Mo_{16}S_{32}$ cluster model approach starting from activation of hydrogen and adsorption of sulfur compunds. Under typical HDS conditions, Mo-edges are covered with sulfur atoms and therfore vacancies are needed for adsorption of sulfur compounds. Both hydrogenation and direct desulfurization pathways proceed first by hydrogenation step. The adsorption binding energies of thiophene, DBT and the reaction intermediates reduce when the Mo-edges are promoted with nickel atoms.

CHAPTER VIII

SUMMARY AND CONCLUSION

We studied in a great detail solvation of the actinide complex in water using polarizable continuum model.[119] Our results show that Pu(IV) ion has a higher tendency than the Th(IV) ion to form inner sphere complex with counterions[119]. Most of the ab-initio calculations also indicate that the radionuclides have a strong tendency to form complexes with common counter-ions present in nuclear waste water.[2,8,37] We demonstrated that counter-ions if present can replace water molecules in the first coordination shell of U(VI), Pu(IV,VI), Eu(III) and Th(IV) ions and hence they are less likely to exist in the form of completely dissociated cation solvated by water molecules. In a very dilute system, however, these ions can exist in completely solvated forms. Thus, quantum chemistry calculations can help us to understand the mechanism of complexation for these radionuclides with graphene-based materials.

The current-voltage curves were obtained using a combination of Greens function and DFT to test the applicability of graphene-based nanosensor for detection of radionuclides in nuclear waste water. Graphene nanosheets need to be functionalized to act as an effective sensor for U/Pu complexes as indicated by MEPs calculated from ab-initio DFT calculations. Since graphene oxide (GO) has a higher affinity for U and Pu complexes,[25] we used three types of GO: (a) GO with two –OH and one –O– functional groups present (type I), (b) GO containing a carbonyl functional group (type II), and (c) GO containing a carboxylic functional group (type III), to study their interactions with

plutonium complexes. Our calculations show significant reduction in current values for GO containing –CO functional group as compared to a pristine graphene as well as type I and type III GOs in the presence of Pu complex. The plutonium nitrate complex causes localization of HOMO and LUMO which results in $1/6^{th}$ order reduction in average conductance after exposure to the radionuclide complex. Similar trends were observed for Eu(III) and U(VI) aquo-nitrate complexes.

Experiments conducted using a graphene sheet (grown using CVD) on a silicon oxide wafer showed promising results when tested with Eu(III) nitrate solution. A noticeable change in conductance was observed at high gate voltage.[264] The change in the conductance can be explained qualitatively using molecular orbitals (MO) and charge transfer between europium complex and the graphene sheet. Our calculations showed that although the conductance of graphene remained unchanged when exposed to neutral Eu(III) nitrate complex, the conductance of the graphene nanojunction increased when the complex was positively charged. In dilute solutions, the complexes are likely to be present in dissociated form, and therefore, positively charged complexes can directly interact with graphene junctions. We expect the conductance to reduce even more in case of GO(type II) when exposed to charged moieties.

The challenge will then be to regenerate this material for next application. The radionuclide can be recovered however by burning the material or likewise[29]. The challenge however exists in making these sensors target-selective. GO has a higher affinity for heavy metals like Co(II), and Cd(II) ions,[34] which are heavily abundant in nuclear power plants. More sorption experiments are needed to confirm the selectivity of

GO in presence of heavy ions. Another major challenge is in synthesizing this material at large scale with low cost.

Using molecular dynamics study, we showed an application of DNA origami for biosensing applications. The biosensor assembly consisted of two known thrombin binding aptamers TBA26 and TBA29 tethered to a reactangular shaped DNA origami with a specific target to detect thrombin, an enzyme responsible for blood coagulation. We estimated the binding affinities based on relative energy of interaction between nuclic acids and thrombin residues. TBA29 showed a higher binding affinity towrads thrombin than TBA26 since it utilized both its duplex and quadruplex motifs to bind with thrombin. TBA26 on the other hand attached to thrombin through its quadruplex structure only. TBA26 preferred exosite I while TBA29 preferred exosite II present on thrombin. The two aptamers attached to the DNA origami assembly have better binding affinity to thrombin than the corresponding binding of the two aptamers without the origami, meaning that the origami boosted each individual aptamer binding to thrombin.

Molecular dynamics performed on hydrocarbon mixture containing thiophenes and dibenzothiophenes show that these sulfur-compunds diffused from bulk to the MoS_2 edges showing the catalytic nature of the MoS_2 edges. MoS_2/graphene complex showed improvement over pristine MoS_2 cluster for adsorption of thiophene as observed from reduction in binding energy. A comprehensive analysis of HDS reaction mechanism was presented using $Mo_{16}S_{32}$ cluster model approach starting from activation of hydrogen and adsorption of sulfur compunds. Under typical HDS conditions, vacancies were needed for adsorption of sulfur compounds on Mo-edges. Both hydrogenation and direct

desulfurization pathways proceeded first by hydrogenation step. Doping Mo-edges with nickel atoms reduced the adsorption binding energies of thiophene, DBT and the reaction intermediates.

REFERENCES

1. Greathouse, J. A.; O'Brien, R. J.; Bemis, G.; Pabalan, R. T., Molecular Dynamics Study of Aqueous Uranyl Interactions with Quartz (010). *J. Phys. Chem. B* **2002,** *106*, 1646–1655.
2. Craw, J. S.; Vincent, M. A.; Hillier, I. H.; Wallwork, A. L., Ab Initio Quantum Chemical Calculations on Uranyl UO_2^{2+}, Plutonyl PuO_2^{2+}, and Their Nitrates and Sulfates. *J. Phys. Chem.* **1995,** *99*, 10181-10185.
3. Blaudeau, J.-P.; Zygmunt, S. A.; Curtiss, L. A.; Reed, D. T.; Bursten, B. E., Relativistic Density Functional Investigation of $Pu(H_2O)_n^{3+}$ Clusters. *Chem. Phys. Lett.* **1999,** *310*, 347-354.
4. Choppin, G. R.; Morgenstern, A., Distribution and Movement of Environmental Plutonium. In *Radioactivity in the Environment*, Elsevier: 2001; Vol. 1, pp 91-105.
5. Spencer, S.; Gagliardi, L.; Handy, N. C.; Ioannou, A. G.; Skylaris, C.-K.*, et al.*, Hydration of UO_2^{2+} and PuO_2^{2+}. *J. Phys. Chem. A* **1999,** *103*, 1831-1837.
6. Majumdar, D.; Balasubramanian, K., Theoretical Studies on the Nature of Uranyl–Silicate, Uranyl–Phosphate and Uranyl–Arsenate Interactions in the Model $H_2UO_2SiO_4.3H_2O$, $HUO_2PO_4.3H_2O$, and $HUO_2AsO_4.3H_2O$ Molecules. *Chem. Phys. Lett.* **2004,** *397*, 26-33.
7. Cao, Z.; Balasubramanian, K., Theoretical Studies of $UO_2(H_2O)_n^{2+}$,$NpO_2(H_2O)_n^{+}$, and $PuO_2(H_2O)_n^{2+}$ Complexes (N = 4–6) in Aqueous Solution and Gas Phase. *J. Chem. Phys.* **2005,** *123*
8. Chaudhuri, D.; Balasubramanian, K., Electronic Structure and Spectra of Plutonyl Complexes and Their Hydrated Forms: PuO_2CO_3 and $PuO_2CO_3.Nh_2o$ (N = 1,2). *Chem. Phys. Lett.* **2004,** *399*, 67-72.
9. Balasubramanian, K.; Chaudhuri, D., Computational Modeling of Environmental Plutonyl Mono-, Di- and Tricarbonate Complexes with Ca Counterions: Structures and Spectra: , $PuO_2(CO_3)_2Ca$, and $PuO_2(CO_3)_3Ca_3$. *Chem. Phys. Lett.* **2008,** *450*, 196-202.
10. Ismail, N.; Heully, J.-L.; Saue, T.; Daudey, J.-P.; Marsden, C. J., Theoretical Studies of the Actinides: Method Calibration for the UO_2^{2+} and PuO_2^{2+} Ions. *Chem. Phys. Lett.* **1999,** *300*, 296-302.
11. Buz'ko, V.; Chuiko, G.; Kushkhov, K., Dft Study of the Structure and Stability of Pu(III) and Pu(IV) Chloro Complexes. *Russ. J. Inorg. Chem.* **2012,** *57*, 62-67.
12. Allen, P. G.; Bucher, J. J.; Shuh, D. K.; Edelstein, N. M.; Reich, T., Investigation of Aquo and Chloro Complexes of UO_2^{2+}, NpO^{2+}, Np^{4+}, and Pu^{3+} by X-Ray Absorption Fine Structure Spectroscopy. *Inorg. Chem.* **1997,** *36*, 4676-4683.
13. Hennig, C.; Tutschku, J.; Rossberg, A.; Bernhard, G.; Scheinost, A. C., Comparative Exafs Investigation of Uranium(VI) and -(IV) Aquo Chloro Complexes in Solution Using a Newly Developed Spectroelectrochemical Cell. *Inorg. Chem.* **2005,** *44*, 6655-6661.
14. Bühl, M.; Sieffert, N.; Golubnychiy, V.; Wipff, G., Density Functional Theory Study of Uranium(VI) Aquo Chloro Complexes in Aqueous Solution. *J. Phys. Chem. A* **2008,** *112*, 2428-2436.

15. Bühl, M.; Diss, R.; Wipff, G., Coordination Mode of Nitrate in Uranyl(VI) Complexes: A First-Principles Molecular Dynamics Study. *Inorg. Chem.* **2007,** *46*, 5196-5206.
16. Xianggui, Y.; Smith, R. B.; Shengting, C.; De Almeida, V.; Khomami, B., Influence of Nitric Acid on Uranyl Nitrate Association in Aqueous Solutions: A Molecular Dynamics Simulation Study. *Solvent Extr. Ion Exch.* **2010,** *28*, 1-18.
17. Odoh, S. O.; Schreckenbach, G., Theoretical Study of the Structural Properties of Plutonium(IV) and (VI) Complexes. *J. Phys. Chem. A* **2011,** *115*, 14110-14119.
18. Duvail, M.; Martelli, F.; Vitorge, P.; Spezia, R., Polarizable Interaction Potential for Molecular Dynamics Simulations of Actinoids(III) in Liquid Water. *J. Chem. Phys.* **2011,** *135*, 044503-10.
19. Marjolin, A.; Gourlaouen, C.; Clavaguéra, C.; Ren, P.; Wu, J.*, et al.*, Toward Accurate Solvation Dynamics of Lanthanides and Actinides in Water Using Polarizable Force Fields: From Gas-Phase Energetics to Hydration Free Energies. *Theor Chem Acc* **2012,** *131*, 1-14.
20. Yang, T.; Tsushima, S.; Suzuki, A., Quantum Mechanical and Molecular Dynamical Simulations on Thorium(IV) Hydrates in Aqueous Solution. *J. Phys. Chem. A* **2001,** *105*, 10439-10445.
21. Tsushima, S.; Yang, T.; Mochizuki, Y.; Okamoto, Y., Ab Initio Study on the Structures of Th(IV) Hydrate and Its Hydrolysis Products in Aqueous Solution. *Chem. Phys. Lett.* **2003,** *375*, 204-212.
22. R⌈al, F.; Trumm, M.; Vallet, V.; Schimmelpfennig, B.; Masella, M.*, et al.*, Quantum Chemical and Molecular Dynamics Study of the Coordination of Th(IV) in Aqueous Solvent. *J. Phys. Chem. B* **2010,** *114*, 15913-15924.
23. Spezia, R.; Beuchat, C.; Vuilleumier, R.; D'Angelo, P.; Gagliardi, L., Unravelling the Hydration Structure of ThX_4 (X = Br, Cl) Water Solutions by Molecular Dynamics Simulations and X-Ray Absorption Spectroscopy. *J. Phys. Chem. B* **2012,** *116*, 6465-6475.
24. Romanchuk, A. Y.; Slesarev, A. S.; Kalmykov, S. N.; Kosynkin, D. V.; Tour, J. M., Graphene Oxide for Effective Radionuclide Removal. *Phys. Chem. Chem. Phys.* **2013,** *15*, 2321-2327.
25. Romanchuk, A. Y.; Slesarev, A. S.; Kalmykov, S. N.; Kosynkin, D. V.; Tour, J. M., Graphene Oxide for Effective Radionuclide Removal. *Physical Chemistry Chemical Physics* **2013,** *15*, 2321-2327.
26. Lahaye, R. J. W. E.; Jeong, H. K.; Park, C. Y.; Lee, Y. H., Density Functional Theory Study of Graphite Oxide for Different Oxidation Levels. *Phys. Rev. B.* **2009,** *79*, 125435.
27. Sheka, E. F.; Popova, N. A., Molecular Theory of Graphene Oxide. *Phys. Chem. Chem. Phys.* **2013,** *15*, 13304-13322.
28. Wu, Q.-Y.; Lan, J.-H.; Wang, C.-Z.; Xiao, C.-L.; Zhao, Y.-L.*, et al.*, Understanding the Bonding Nature of Uranyl Ion and Functionalized Graphene: A Theoretical Study. *J. Phys. Chem. A* **2014,** *118*, 2149-2158.

29. Wu, Q.-Y.; Lan, J.-H.; Wang, C.-Z.; Zhao, Y.-L.; Chai, Z.-F.*, et al.*, Understanding the Interactions of Neptunium and Plutonium Ions with Graphene Oxide: Scalar-Relativistic Dft Investigations. *J. Phys. Chem. A* **2014,** *118*, 10273-10280.
30. Sun, Y.; Shao, D.; Chen, C.; Yang, S.; Wang, X., Highly Efficient Enrichment of Radionuclides on Graphene Oxide-Supported Polyaniline. *Environ. Sci. Technol.* **2013,** *47*, 9904-9910.
31. Zhu, Y.; Murali, S.; Cai, W.; Li, X.; Suk, J. W.*, et al.*, Graphene and Graphene Oxide: Synthesis, Properties, and Applications. *Adv. Mater.* **2010,** *22*, 3906-3924.
32. Georgakilas, V.; Otyepka, M.; Bourlinos, A. B.; Chandra, V.; Kim, N.*, et al.*, Functionalization of Graphene: Covalent and Non-Covalent Approaches, Derivatives and Applications. *Chem. Rev.* **2012,** *112*, 6156-6214.
33. Wang, Y.; Li, Z.; Wang, J.; Li, J.; Lin, Y., Graphene and Graphene Oxide: Biofunctionalization and Applications in Biotechnology. *Trends Biotechnol.* **2011,** *29*, 205-212.
34. Zhao, G.; Li, J.; Ren, X.; Chen, C.; Wang, X., Few-Layered Graphene Oxide Nanosheets as Superior Sorbents for Heavy Metal Ion Pollution Management. *Environ. Sci. Technol.* **2011,** *45*, 10454-10462.
35. Loh, K. P.; Bao, Q.; Eda, G.; Chhowalla, M., Graphene Oxide as a Chemically Tunable Platform for Optical Applications. *Nat. Chem.* **2010,** *2*, 1015-1024.
36. Rangel, N. L.; Seminario, J. M., Graphene Terahertz Generators for Molecular Circuits and Sensors. *J. Phys. Chem. A* **2008,** *112*, 13699-13705.
37. Kumar, N.; Seminario, J. M., Design of Nanosensors for Fissile Materials in Nuclear Waste Water. *J. Phys. Chem. C* **2013,** *117*, 24033-24041.
38. Kumar, N.; Seminario, J. M., A Quantum Chemistry Approach for the Design and Analysis of Nanosensors for Fissile Materials. In *Design and Applications of Nanomaterials for Sensors*, Springer: 2014; pp 1-29.
39. Derosa, P. A.; Seminario, J. M., Electron Transport through Single Molecules: Scattering Treatment Using Density Functional and Green Function Theories. *J. Phys. Chem. B* **2001,** *105*, 471-481.
40. Seminario, J. M.; Cordova, L. E.; Derosa, P. A., An Ab Initio Approach to the Calculation of Current-Voltage Characteristics of Programmable Molecular Devices. *Proc. IEEE* **2003,** *91*, 1958-1975.
41. Seminario, J. M.; Zacarias, A. G.; Derosa, P. A., Analysis of a Dinitro-Based Molecular Device. *The Journal of Chemical Physics* **2002,** *116*, 1671-1683.
42. Edson, P. B.; Alfredo, D. B.; Norma, L. R.; Hong, Z.; Michael, L. N.*, et al.*, Current–Voltage–Temperature Characteristics of DNA Origami. *Nanotechnology* **2009,** *20*, 175102.
43. Bobadilla, A. D.; Bellido, E. P.; Rangel, N. L.; Zhong, H.; Norton, M. L.*, et al.*, DNA Origami Impedance Measurement at Room Temperature. *J. Chem. Phys.* **2009,** *130*, 171101.
44. Strachan, A., Tutorial 1: Atomistic Material Science - Ab Initio Simulations of Materials. 2011.

45. Seminario, J. M., An Introduction to Density Functional Theory in Chemistry. In *Theoretical and Computational Chemistry*, Seminario, J. M.; Politzer, P., Eds. Elsevier: 1995; Vol. Volume 2, pp 1-27.
46. Ditchfield, R.; Hehre, W. J.; Pople, J. A., Self-Consistent Molecular-Orbital Methods. IX. An Extended Gaussian-Type Basis for Molecular-Orbital Studies of Organic Molecules. *J. Chem. Phys.* **1971,** *54*, 724-728.
47. Datta, S., *Electronic Transport in Mesoscopic Systems*. Cambridge university press: 1997.
48. Datta, S., *Lessons from Nanoelectronics : A New Perspective on Transport*. World Scientific Publishing Co.: Singapore, 2012.
49. Derosa, P. A.; Seminario, J. M., Electron Transport through Single Molecules: Scattering Treatment Using Density Functional and Green Function Theories. *J. Phys. Chem. B* **2000,** *105*, 471-481.
50. Tian, W.; Datta, S.; Hong, S.; Reifenberger, R.; Henderson, J. I.*, et al.*, Conductance Spectra of Molecular Wires. *J. Chem. Phys.* **1998,** *109*, 2874.
51. Sun, Y.; Shao, D.; Chen, C.; Yang, S.; Wang, X., Highly Efficient Enrichment of Radionuclides on Graphene Oxide-Supported Polyaniline. *Environ. Sci. Technol.* **2013,** *47*, 9904-9910.
52. Foxe, M.; Cazalas, E.; Lamm, H.; Majcher, A.; Piotrowski, C.*, et al.* In *Graphene-Based Neutron Detectors*, Nuclear Science Symposium and Medical Imaging Conference (NSS/MIC), 2011 IEEE, 23-29 Oct. 2011; 2011; pp 352-355.
53. Patil, A.; Koybasi, O.; Lopez, G.; Foxe, M.; Childres, I.*, et al.* In *Graphene Field Effect Transistor as Radiation Sensor*, Nuclear Science Symposium and Medical Imaging Conference (NSS/MIC), 2011 IEEE, 23-29 Oct. 2011; 2011; pp 455-459.
54. Geim, A. K.; Novoselov, K. S., The Rise of Graphene. *Nat. Mater.* **2007,** *6*, 183-191.
55. Huang, X.; Yin, Z.; Wu, S.; Qi, X.; He, Q.*, et al.*, Graphene-Based Materials: Synthesis, Characterization, Properties, and Applications. *Small* **2011,** *7*, 1876-1902.
56. Buhl, M.; Diss, R.; Wipff, G., Coordination Mode of Nitrate in Uranyl(VI) Complexes:Â€‰ a First-Principles Molecular Dynamics Study. *Inorg. Chem.* **2007,** *46*, 5196-5206.
57. Buhl, M.; Sieffert, N.; Golubnychiy, V.; Wipff, G., Density Functional Theory Study of Uranium(VI) Aquo Chloro Complexes in Aqueous Solution. *J. Phys. Chem. A* **2008,** *112*, 2428-2436.
58. Spezia, R.; Beuchat, C.; Vuilleumier, R.; D'Angelo, P.; Gagliardi, L., Unravelling the Hydration Structure of ThX_4 (X= Br, Cl) Water Solutions by Molecular Dynamics Simulations and X-Ray Absorption Spectroscopy. *J. Phys. Chem. B* **2012,** *116*, 6465-6475.
59. Hohenberg, P.; Kohn, W., Inhomogeneous Electron Gas. *Phys. Rev. B.* **1964,** *136*, 864-871.
60. Kohn, W.; Sham, L. J., Self-Consistent Equations Including Exchange and Correlation Effects. *Phys. Rev. A* **1965,** *140*, 1133-1138.

61. Becke, A. D., Density-Functional Thermochemistry. III. The Role of Exact Exchange. *J. Chem. Phys.* **1993,** *98*, 5648-5652.
62. Roothaan, C. C. J., New Developments in Molecular Orbital Theory. *Rev. Mod. Phys.* **1951,** *23*, 69-89.
63. Pople, J. A.; Nesbet, R. K., Self-Consistent Orbitals for Radicals. *J. Chem. Phys.* **1954,** *22*, 571-572.
64. McWeeny, R.; Diercksen, G., Self-Consistent Perturbation Theory. II. Extension to Open Shells. *J. Chem. Phys.* **1968,** *49*, 4852-4856.
65. Perdew, J. P.; Chevary, J. A.; Vosko, S. H.; Jackson, K. A.; Pederson, M. R.*, et al.*, Erratum: Atoms, Molecules, Solids, and Surfaces - Applications of the Generalized Gradient Approximation for Exchange and Correlation. *Phys. Rev. B.* **1993,** *48*, 4978-4978.
66. Perdew, J. P.; Chevary, J. A.; Vosko, S. H.; Jackson, K. A.; Pederson, M. R.*, et al.*, Atoms, Molecules, Solids, and Surfaces: Applications of the Generalized Gradient Approximation for Exchange and Correlation. *Phys. Rev. B.* **1992,** *46*, 6671-6687.
67. Perdew, J. P.; Burke, K.; Wang, Y., Generalized Gradient Approximation for the Exchange-Correlation Hole of a Many-Electron System. *Phys. Rev. B.* **1996,** *54*, 16533 - 16539.
68. Perdew, J. P., Unified Theory of Exchange and Correlation Beyond the Local Density Approximation. In *Electronic Structure of Solids*, Ziesche, P.; Eschrig, H., Eds. Akademie Verlag: Berlin, 1991; pp 11-20.
69. Burke, K.; Perdew, J. P.; Wang, Y., In *Electronic Density Functional Theory: Recent Progress and New Directions*, Ed. J. F. Dobson, G. V., and M. P. Das, Ed. Plenum Press: New York, 1998.
70. Seminario, J. M.; Araujo, R. A.; Yan, L., Negative Differential Resistance in Metallic and Semiconducting Clusters. *J. Phys. Chem. B* **2004,** *108*, 6915-6918.
71. Seminario, J. M.; Derosa, P. A.; Cordova, L. E.; Bozard, B. H., A Molecular Device Operating at Terahertz Frequencies. *IEEE Trans. Nanotech.* **2004,** *3*, 215-218.
72. Seminario, J. M., Calculation of Intramolecular Force Fields from Second-Derivative Tensors. *Int. J. Quantum Chem.* **1996,** *60*, 1271-1277.
73. Rangel, N. L.; Sotelo, J. C.; Seminario, J. M., Mechanism of Carbon-Nanotubes Unzipping into Graphene Ribbons. *J. Chem. Phys* **2009,** *131*, 031105:1-4.
74. Balbuena, P. B.; Calvo, S. R.; Lamas, E. J.; Salazar, P. F.; Seminario, J. M., Adsorption and Dissociation of H_2O_2 on Pt and Pt-Alloy Clusters and Surfaces. *J. Phys. Chem. B* **2006,** *110*, 17452-17459.
75. Aguilera-Segura, S. M.; Seminario, J. M., Ab Initio Analysis of Silicon Nano-Clusters. *J. Phys. Chem. C* **2014,** *118*, 1397-1406.
76. Cárdenas-Jirón, G. I.; Leon-Plata, P.; Cortes-Arriagada, D.; Seminario, J. M., Electron Transport Properties through Graphene Oxide—Cobalt Phthalocyanine Complexes. *J. Phys. Chem. C* **2013,** *117*, 23664-23675.
77. Salazar-Salinas, K.; Jauregui, L. A.; Kubli-Garfias, C.; Seminario, J. M., Molecular Biosensor Based on a Coordinated Iron Complex. *J. Chem. Phys.* **2009,** *130*, 105101-1-9.

78. Bobadilla, A. D.; Seminario, J. M., Assembly of a Noncovalent DNA Junction on Graphene Sheets and Electron Transport Characteristics. *J. Phys. Chem. C* **2013,** *117*, 26441-26453.
79. Rangel, N. L.; Seminario, J. M., Vibronics and Plasmonics Based Graphene Sensors. *J. Chem. Phys.* **2010,** *132*, 125102.
80. Sotelo, J. C.; Yan, L.; Wang, M.; Seminario, J. M., Field Induced Conformational Changes in Bimetallic Oligoaniline Junctions. *Phys. Rev. A* **2007,** *75*, 022511 (13 pages).
81. Juaregui, L. A.; Seminario, J. M., A DNA Sensor for Sequencing and Mismatches Based on Electron Transport through Watson-Crick and Non-Watson-Crick Base Pairs. *IEEE Sensors* **2008,** *8*, 803-814.
82. Politzer, P.; Seminario, J. M., Energy Changes Associated with Some Decomposition Steps of 1,3,3-Trinitroazetidine - a Nonlocal Density-Functional Study. *Chem. Phys. Lett.* **1993,** *207*, 27-30.
83. Habibollahzadeh, D.; Grodzicki, M.; Seminario, J. M.; Politzer, P., Computational Study of the Concerted Gas-Phase Triple Dissociations of 1,3,5-Triazacyclohexane and Its 1,3,5-Trinitro Derivative (RDX). *J. Phys. Chem.* **1991,** *95*, 7699-7702.
84. Politzer, P.; Seminario, J. M., Computational Study of the Structure of Dinitraminic Acid, $HN(NO_2)_2$ and the Energetics of Some Possible Decomposition Steps. *Chem. Phys. Lett.* **1993,** *216*, 348-352.
85. Murray, J.; Redfern, P.; Seminario, J.; Politzer, P., Anomalous Energy Effects in Some Aliphatic and Alicyclic Aza Systems and Their Nitro-Derivatives. *J. Phys. Chem.* **1990,** *94*, 2320-2323
86. Cao, X.; Dolg, M.; Stoll, H., Valence Basis Sets for Relativistic Energy-Consistent Small-Core Actinide Pseudopotentials. *J. Chem. Phys.* **2003,** *118*.
87. Cao, X.; Dolg, M., Segmented Contraction Scheme for Small-Core Actinide Pseudopotential Basis Sets. *J Mol Struct (THEOCHEM)* **2004,** *673*, 203-209.
88. Hehre, W. J.; Ditchfield, R.; Pople, J. A., Self-Consistent Moleculer-Orbital Methods. XII. Further Extensions of Gaussian-Type Basis Sets for Use in Molecular-Orbital Studies of Organic-Molecules. *J. Chem. Phys.* **1972,** *56*.
89. Cao, X.; Dolg, M.; Stoll, H., Valence Basis Sets for Relativistic Energy-Consistent Small-Core Actinide Pseudopotentials. *J. Chem. Phys.* **2003,** *118*.
90. Frisch, M. J.; Trucks, G. W.; Schlegel, H. B.; Scuseria, G. E.; Robb, M. A.*, et al. Gaussian 09, Revision B.01*, Gaussian, Inc.: 2009.
91. Peng, C.; Ayala, P. Y.; Schlegel, H. B.; Frisch, M. J., Using Redundant Internal Coordinates to Optimize Equilibrium Geometries and Transition States. *J. Comp. Chem.* **1996,** *17*, 49-56.
92. Li, X.; Frisch, M. J., Energy-Represented Diis within a Hybrid Geometry Optimization Method. *J. Chem. Theory Comput.* **2006,** *2*, 835 - 839.
93. Grimme, S.; Antony, J.; Ehrlich, S.; Krieg, H., A Consistent and Accurate Ab Initio Parametrization of Density Functional Dispersion Correction (Dft-D) for the 94 Elements H-Pu. *J. Chem. Phys* **2010,** *132*.

94. Barone, V.; Cossi, M., Quantum Calculation of Molecular Energies and Energy Gradients in Solution by a Conductor Solvent Model. *J. Phys. Chem. A* **1998,** *102*, 1995-2001.
95. Cossi, M.; Rega, N.; Scalmani, G.; Barone, V., Energies, Structures, and Electronic Properties of Molecules in Solution with the C-PCM Solvation Model. *J. Comput. Chem.* **2003,** *24*, 669-681.
96. Roos, B. O.; Lindh, R.; Malmqvist, P.-Ã. k.; Veryazov, V.; Widmark, P.-O., New Relativistic Ano Basis Sets for Actinide Atoms. *Chem. Phys. Lett.* **2005,** *409*, 295-299.
97. Roos, B. O.; Lindh, R.; Malmqvist, P.-Å.; Veryazov, V.; Widmark, P.-O.*, et al.*, New Relativistic Atomic Natural Orbital Basis Sets for Lanthanide Atoms with Applications to the Ce Diatom and LuF3. *J. Phys. Chem. A* **2008,** *112*, 11431-11435.
98. Cao, X.; Dolg, M., Theoretical Prediction of the Second to Fourth Actinide Ionization Potentials. *Mol. Phys.* **2003,** *101*, 961-969.
99. Johansson, G.; Magini, M.; Ohtaki, H., Coordination around Thorium(IV) in Aqueous Perchlorate, Chloride and Nitrate Solutions. *J. Solution Chem.* **1991,** *20*, 775-792.
100. Moll, H.; Denecke, M. A.; Jalilehvand, F.; Sandström, M.; Grenthe, I., Structure of the Aqua Ions and Fluoride Complexes of Uranium(IV) and Thorium(IV) in Aqueous Solution an Exafs Study. *Inorg. Chem.* **1999,** *38*, 1795-1799.
101. Rothe, J.; Denecke, M. A.; Neck, V.; Müller, R.; Kim, J. I., XAFS Investigation of the Structure of Aqueous Thorium(IV) Species, Colloids, and Solid Thorium(IV) Oxide/Hydroxide. *Inorg. Chem.* **2002,** *41*, 249-258.
102. Spezia, R.; Jeanvoine, Y.; Beuchat, C.; Gagliardi, L.; Vuilleumier, R., Hydration Properties of Cm(III) and Th(IV) Combining Coordination Free Energy Profiles with Electronic Structure Analysis. *Phys. Chem. Chem. Phys.* **2014,** *16*, 5824-5832.
103. Bühl, M.; Kabrede, H.; Diss, R.; Wipff, G., Effect of Hydration on Coordination Properties of Uranyl(VI) Complexes. A First-Principles Molecular Dynamics Study. *J. Am. Chem. Soc.* **2006,** *128*, 6357-6368.
104. Gaunt, A. J.; May, I.; Neu, M. P.; Reilly, S. D.; Scott, B. L., Structural and Spectroscopic Characterization of Plutonyl(VI) Nitrate under Acidic Conditions. *Inorg. Chem.* **2011,** *50*, 4244-4246.
105. Tsushima, S.; Yang, T., Relativistic Density Functional Theory Study on the Structure and Bonding of U(IV) and Np(IV) Hydrates. *Chem. Phys. Lett.* **2005,** *401*, 68-71.
106. Atta-Fynn, R.; Johnson, D. F.; Bylaska, E. J.; Ilton, E. S.; Schenter, G. K.*, et al.*, Structure and Hydrolysis of the U(IV), U(V), and U(VI) Aqua Ions from Ab Initio Molecular Simulations. *Inorg. Chem.* **2012,** *51*, 3016-3024.
107. Hay, P. J.; Wadt, W. R., Ab Initio Effective Core Potentials for Molecular Calculations - Potentials for the Transition-Metal Atoms Sc to Hg *J. Chem. Phys.* **1985,** *82* 270-283.

108. Hay, P. J.; Wadt, W. R., Ab Initio Effective Core Potentials for Molecular Calculations - Potentials for K to Au Including the Outermost Core Orbitals *J. Chem. Phys.* **1985,** *82* 299-310.
109. Wadt, W. R.; Hay, P. J., Ab Initio Effective Core Potentials for Molecular Calculations - Potentials for Main Group Elements Na to Bi *J. Chem. Phys.* **1985,** *82* 284-298.
110. Rios, D.; Michelini, M. C.; Lucena, A. F.; Marçalo, J.; Bray, T. H.*, et al.*, Gas-Phase Uranyl, Neptunyl, and Plutonyl: Hydration and Oxidation Studied by Experiment and Theory. *Inorg. Chem.* **2012**.
111. Seminario, J. M.; Yan, L., Ab Initio Analysis of Electron Currents in Thioalkanes. *Int. J. Quantum Chem.* **2005,** *102*, 711-723.
112. Blaise, J.; Wyart, J. F., *Energy Levels and Atomic Spectra of Actinides, International Tables of Selected Constants* 1992; Vol. 20.
113. Hernández Rosas, J. J.; Ramírez Gutiérrez, R. E.; Escobedo-Morales, A.; Chigo Anota, E., First Principles Calculations of the Electronic and Chemical Properties of Graphene, Graphane, and Graphene Oxide. *J Mol Model* **2011,** *17*, 1133-1139.
114. Dreyer, D. R.; Park, S.; Bielawski, C. W.; Ruoff, R. S., The Chemistry of Graphene Oxide. *Chem. Soc. Rev.* **2010,** *39*, 228-240.
115. Dovesi, R.; Saunders, V. R.; Roetti, C.; Orlando, R.; Zicovich-Wilson, C. M.*, et al.*, *Crystal06 User's Manual* University of Torino: Torino, 2006.
116. O'Boyle, N. M.; Tenderholt, A. L.; Langner, K. M., Cclib: A Library for Package-Independent Computational Chemistry Algorithms. *J. Comput. Chem.* **2008,** *29*, 839-845.
117. Punckt, C.; Muckel, F.; Wolff, S.; Aksay, I. A.; Chavarin, C. A.*, et al.*, The Effect of Degree of Reduction on the Electrical Properties of Functionalized Graphene Sheets. *Appl. Phys. Lett.* **2013,** *102*, 023114-5.
118. Kumar, N.; Seminario, J. M., Design of Nanosensors for Fissile Materials in Nuclear Waste Water. *The Journal of Physical Chemistry C* **2013,** *117*, 24033-24041.
119. Kumar, N.; Seminario, J. M., Solvation of Actinide Salts in Water Using a Polarizable Continuum Model. *J. Phys. Chem. A* **2015**.
120. Duvail, M.; Guilbaud, P., Understanding the Nitrate Coordination to Eu3+ Ions in Solution by Potential of Mean Force Calculations. *Phys. Chem. Chem. Phys.* **2011,** *13*, 5840-5847.
121. Xi, J.; Lan, J.-H.; Lu, G.-W.; Zhao, Y.-L.; Chai, Z.-F.*, et al.*, A Density Functional Theory Study of Complex Species and Reactions of Am(III)/Eu(III) with Nitrate Anions. *Mol. Simulat.* **2013,** *40*, 379-386.
122. Wang, P.; Moorefield, C. N.; Lic, S.; Hwang, S.-H.; Shreiner, C. D.*, et al.*, Terpyridinecuii-Mediated Reversible Nanocomposites of Single-Wall Carbon Nanotubes: Towards Metallo-Nanoscale Architectures *Chem. Commun.* **2006,** *10*, 1091-1093.
123. Gupta, B. K.; Thanikaivelan, P.; Narayanan, T. N.; Song, L.; Gao, W.*, et al.*, Optical Bifunctionality of Europium-Complexed Luminescent Graphene Nanosheets. *Nano Lett.* **2011,** *11*, 5227-5233.

124. Mo, Z.; Zhao, Y.; Guo, R.; Liu, P.; Xie, T., Preparation and Characterization of Graphene/Europium Oxide Composites. *Mater. Manuf. Process.* **2011,** *27*, 494-498.
125. Perdew, J. P.; Chevary, J. A.; Vosko, S. H.; Jackson, K. A.; Pederson, M. R.*, et al.*, Erratum: Atoms, Molecules, Solids, and Surfaces - Applications of the Generalized Gradient Approximation for Exchange and Correlation. *Phys. Rev. B* **1993,** *48*, 4978-4978.
126. Perdew, J. P.; Chevary, J. A.; Vosko, S. H.; Jackson, K. A.; Pederson, M. R.*, et al.*, Atoms, Molecules, Solids, and Surfaces: Applications of the Generalized Gradient Approximation for Exchange and Correlation. *Phys. Rev. B* **1992,** *46*, 6671-6687.
127. Perdew, J. P.; Burke, K.; Wang, Y., Generalized Gradient Approximation for the Exchange-Correlation Hole of a Many-Electron System. *Phys. Rev. B* **1996,** *54*, 16533 - 16539.
128. Perez-Angel, E. C.; Seminario, J. M., Ab Initio Analysis and Harmonic Force Fields of Gallium Nitride Nanoclusters. *J. Phys. Chem. C* **2011,** *115*, 6467-6477.
129. Cárdenas-Jirón, G. I.; Leon-Plata, P.; Cortes-Arriagada, D.; Seminario, J. M., Electrical Characteristics of Cobalt Phthalocyanine Complexes Adsorbed on Graphene. *J. Phys. Chem. C* **2011,** *115*, 16052-16062.
130. Fu, M.-L.; Rangel, N.; Adams, R.; Seminario, J., Synthesis, Crystal Structure, Photophysical Properties, and Dft Calculations of a Bis(Tetrathia-Calix[4]Arene) Tetracadmium Complex. *J. Cluster Sci.* **2010,** *21*, 867-878.
131. Yan, L.; Bautista, E. J.; Seminario, J. M., Ab Initio Analysis of Electron Currents through Benzene, Naphthalene, and Anthracene. *Nanotechnology* **2007,** *18*, 485701--1-8.
132. Seminario, J. M.; Araujo, R. A.; Yan, L., Negative Differential Resistance in Metallic and Semiconducting Clusters. *J. Phys. Chem. B* **2004,** *108*, 6915-6918.
133. Seminario, J. M.; Derosa, P. A.; Cordova, L. E.; Bozard, B. H., A Molecular Device Operating at Terahertz Frequencies. *IEEE Trans. Nanotech.* **2004,** *3*, 215-218.
134. Balbuena, P. B.; Altomare, D.; Agapito, L. A.; Seminario, J. M., Theoretical Analysis of Oxygen Adsorption on Pt-Based Clusters Alloyed with Co, Ni, or Cr Embedded in a Pt Matrix. *J. Phys. Chem. B* **2003,** *107*, 13671-13680.
135. Derosa, P. A.; Seminario, J. M.; Balbuena, P. B., Properties of Small Bimetallic Ni-Cu Clusters. *J. Phys. Chem. A* **2001,** *105*, 7917-7925.
136. Zacarias, A. G.; Castro, M.; Tour, J. M.; Seminario, J. M., Lowest Energy States of Small Pd Clusters Using Density Functional Theory and Standard Ab Initio Methods. A Route to Understanding Metallic Nanoprobes. *J. Phys. Chem. A* **1999,** *103*, 7692-7700.
137. Seminario, J. M.; Zacarias, A. G.; Castro, M., Systematic Study of the Lowest Energy States of Pd, Pd_2, and Pd_3. *Int. J. Quantum Chem.* **1997,** *61*, 515-523.
138. Seminario, J. M.; Agapito, L. A.; Yan, L.; Balbuena, P. B., Density Functional Theory Study of Adsorption of Ooh on Pt-Based Bimetallic Clusters Alloyed with Cr, Co, and Ni. *Chem. Phys. Lett.* **2005,** *410*, 275-281.

139. Seminario, J. M.; Tour, J. M., Systematic Study of the Lowest Energy States of Au_n (N=1-4) Using Dft. *Int. J. Quantum Chem.* **1997,** *65*, 749-758.
140. Seminario, J. M.; Ma, Y.; Agapito, L. A.; Yan, L.; Araujo, R. A.*, et al.*, Clustering Effects on Discontinuous Gold Film Nanocells. *J. Nanoscience Nanotech.* **2004,** *4*, 907-917.
141. Hay, P. J.; Wadt, W. R., Ab Initio Effective Core Potentials for Molecular Calculations - Potentials for the Transition-Metal Atoms Sc to Hg *J. Chem. Phys.* **1985,** *82* 270-283.
142. Hay, P. J.; Wadt, W. R., Ab Initio Effective Core Potentials for Molecular Calculations - Potentials for K to Au Including the Outermost Core Orbitals *J. Chem. Phys.* **1985,** *82* 299-310.
143. Wadt, W. R.; Hay, P. J., Ab Initio Effective Core Potentials for Molecular Calculations - Potentials for Main Group Elements Na to Bi *J. Chem. Phys.* **1985,** *82* 284-298.
144. Cao, X.; Dolg, M., Segmented Contraction Scheme for Small-Core Actinide Pseudopotential Basis Sets. *J Mol Struct (THEOCHEM)* **2004,** *673*, 203-209.
145. Cao, X.; Dolg, M.; Stoll, H., Valence Basis Sets for Relativistic Energy-Consistent Small-Core Actinide Pseudopotentials. *J. Chem. Phys.* **2003,** *118*.
146. Pople, J. A.; Nesbet, R. K., Self-Consistent Orbitals for Radicals. *J. Chem. Phys.* **1954,** *22*, 571-572.
147. Peng, C.; Ayala, P. Y.; Schlegel, H. B.; Frisch, M. J., Using Redundant Internal Coordinates to Optimize Equilibrium Geometries and Transition States. *J. Comp. Chem.* **1996,** *17*, 49-56.
148. Li, X.; Frisch, M. J., Energy-Represented Diis within a Hybrid Geometry Optimization Method. *J. Chem. Theory Comput.* **2006,** *2*, 835 - 839.
149. Köster, A. M.; Leboeuf, M.; Salahub, D. R., Molecular Electrostatic Potentials from Density Functional Theory. *Comp. Theor. Chem.* **1996,** *3*, 105-142.
150. Mishra, P.; Kumar, A., Molecular Electrostatic Potentials and Fields: Hydrogen Bonding, Recognition, Reactivity and Modelling. *Comp. Theor. Chem.* **1996,** *3*, 257-296.
151. Politzer, P.; Laurence, P. R.; Jayasuriya, K., Molecular Electrostatic Potentials: An Effective Tool for the Elucidation of Biochemical Phenomena. *Environ Health Perspect.* **1985,** *61*, 191-202.
152. Weinhold, F.; Landis, C. R., Natural Bond Orbitals and Extensions of Localized Bonding Concepts. *Chem. Educ. Res. Pract.* **2001,** *2*, 91-104.
153. Reed, A. E.; Weinstock, R. B.; Weinhold, F., Natural Population Analysis. *J. Chem. Phys.* **1985,** *83*, 735-746.
154. Cao, X.; Dolg, M., Theoretical Prediction of the Second to Fourth Actinide Ionization Potentials. *Mol. Phys.* **2003,** *101*, 961-969.
155. Ribar, B.; Kapor, A.; Argay, G.; Kalman, A., Tetraaquatrinitratoeuropium(III) Monohydrate. *Acta Cryst.* **1986,** *C42*, 1450-1452.
156. Zhan, B.; Li, C.; Yang, J.; Jenkins, G.; Huang, W.*, et al.*, Graphene Field-Effect Transistor and Its Application for Electronic Sensing. *Small* **2014,** *10*, 4042-4065.

157. Rangel, N. L.; Seminario, J. M., Vibronics and Plasmonics Based Graphene Sensors. *J. Chem. Phys.* **2010,** *132*, -.
158. Rothemund, P. W. K., Folding DNA to Create Nanoscale Shapes and Patterns. *Nature* **2006,** *440*, 297-302.
159. Douglas, S. M.; Dietz, H.; Liedl, T.; Hogberg, B.; Graf, F.*, et al.*, Self-Assembly of DNA into Nanoscale Three-Dimensional Shapes. *Nature* **2009,** *459*, 414-418.
160. Seminario, J. M.; Agapito, L. A.; Figueroa, H. P., Towards the Design of Programmable Self-Assembled DNA-Cnt: An Approach to Nanobiotronics. *Proc. IEEE Nanotech. Conf.* **2002,** *2*, 287-290.
161. Jauregui, L. A.; Seminario, J. M., Transversal Characteristics of DNA Devices. In *Nanotechnology, 2008. Nano-08. 8th IEEE Conference*, 2008; pp 725-728.
162. Bobadilla, A. D.; Bellido, E. P.; Seminario, J. M. In *Transmission of Vibrational Signals through a Cnt-DNA Interface*, Nanoelectronic Devices for Defense and Security Conference, Bahia Mar Beach Resort, Fort Lauderdale, Florida, Bahia Mar Beach Resort, Fort Lauderdale, Florida, 2009.
163. Jauregui, L. A.; Salazar-Salinas, K.; Seminario, J. M., Transverse Electronic Transport in Double-Stranded DNA Nucleotides. *J. Phys. Chem. B* **2009,** *113*, 6230-6239.
164. Bobadilla, A. D.; Seminario, J. M., DNA-Cnt Interactions and Gating Mechanism Using Md and Dft *J. Phys. Chem. C* **2011,** *115*, 3466-3474.
165. Bobadilla, A. D.; Seminario, J. M., Self-Assembly of a Gapped Carbon Nanotube-DNA Molecular Junction *J. Mol. Modeling* **2012,** *18*, 3291-3300.
166. Otero-Navas, I.; Seminario, J. M., Molecular Electrostatic Potentials of DNA Base-Base Pairing and Mispairing. *J. Mol. Modeling* **2012,** *18*, 91-101.
167. Pan, K.; Boulais, E.; Yang, L.; Bathe, M., Structure-Based Model for Light-Harvesting Properties of Nucleic Acid Nanostructures. *Nucleic Acids Res.* **2014,** *42*, 2159-2170.
168. Rangnekar, A.; Zhang, A. M.; Li, S. S.; Bompiani, K. M.; Hansen, M. N.*, et al.*, Increased Anticoagulant Activity of Thrombin-Binding DNA Aptamers by Nanoscale Organization on DNA Nanostructures. *Nanomed. Nanotechnol. Biol. Med. 8*, 673-681.
169. Lancellotti, S.; De Cristofaro, R., Nucleotide-Derived Thrombin Inhibitors: A New Tool for an Old Issue. *Cardiovasc. Hematol. Agents Med. Chem.* **2009,** *7*, 19-28.
170. Musumeci, D.; Montesarchio, D., Polyvalent Nucleic Acid Aptamers and Modulation of Their Activity: A Focus on the Thrombin Binding Aptamer. *Pharmacol. Ther.* **2012,** *136*, 202-215.
171. Cho, H.; Baker, B. R.; Wachsmann-Hogiu, S.; Pagba, C. V.; Laurence, T. A.*, et al.*, Aptamer-Based Serrs Sensor for Thrombin Detection. *Nano Lett.* **2008,** *8*, 4386-4390.
172. Meneghello, A.; Sosic, A.; Antognoli, A.; Cretaio, E.; Gatto, B., Development and Optimization of a Thrombin Sandwich Aptamer Microarray. *Microarrays* **2012,** *1*, 95.

173. Müller, J.; Wulffen, B.; Pötzsch, B.; Mayer, G., Multidomain Targeting Generates a High-Affinity Thrombin-Inhibiting Bivalent Aptamer. *ChemBioChem* **2007,** *8*, 2223-2226.
174. Shiang, Y.-C.; Hsu, C.-L.; Huang, C.-C.; Chang, H.-T., Gold Nanoparticles Presenting Hybridized Self-Assembled Aptamers That Exhibit Enhanced Inhibition of Thrombin. *Angew. Chem. Int. Ed.* **2011,** *50*, 7660-7665.
175. Russo Krauss, I.; Merlino, A.; Randazzo, A.; Novellino, E.; Mazzarella, L.*, et al.*, High-Resolution Structures of Two Complexes between Thrombin and Thrombin-Binding Aptamer Shed Light on the Role of Cations in the Aptamer Inhibitory Activity. *Nucleic Acids Res.* **2012,** *40*, 8119-28.
176. Padmanabhan, K.; Padmanabhan, K. P.; Ferrara, J. D.; Sadler, J. E.; Tulinsky, A., The Structure of Alpha-Thrombin Inhibited by a 15-Mer Single-Stranded DNA Aptamer. *J. Biol. Chem.* **1993,** *268*, 17651-4.
177. Wagner-Whyte, J.; Khuri, S.; Preiss, J.; Kurz, J.; Olson, K.*, et al.*, Discovery of a Potent, Direct Thrombin Inhibiting Aptamer. *J. Thromb. Haemost* **2007,** *5*.
178. Russo Krauss, I.; Pica, A.; Merlino, A.; Mazzarella, L.; Sica, F., Duplex-Quadruplex Motifs in a Peculiar Structural Organization Cooperatively Contribute to Thrombin Binding of a DNA Aptamer. *Acta Crystallogr. D Biol. Crystallogr.* **2013,** *69*, 2403-11.
179. Bock, L. C.; Griffin, L. C.; Latham, J. A.; Vermaas, E. H.; Toole, J. J., Selection of Single-Stranded DNA Molecules That Bind and Inhibit Human Thrombin. *Nature* **1992,** *355*, 564-566.
180. Pagba, C. V.; Lane, S. M.; Cho, H.; Wachsmann-Hogiu, S., Direct Detection of Aptamer-Thrombin Binding Via Surface-Enhanced Raman Spectroscopy. *BIOMEDO* **2010,** *15*, 047006-047006-8.
181. Wang, Y.; Bao, L.; Liu, Z.; Pang, D.-W., Aptamer Biosensor Based on Fluorescence Resonance Energy Transfer from Upconverting Phosphors to Carbon Nanoparticles for Thrombin Detection in Human Plasma. *Anal. Chem.* **2011,** *83*, 8130-8137.
182. Sosic, A.; Meneghello, A.; Cretaio, E.; Gatto, B., Human Thrombin Detection through a Sandwich Aptamer Microarray: Interaction Analysis in Solution and in Solid Phase. *Sensors (Basel, Switzerland)* **2011,** *11*, 9426-9441.
183. Zheng, J.; Lin, L.; Cheng, G.; Wang, A.; Tan, X.*, et al.*, Study on an Electrochemical Biosensor for Thrombin Recognition Based on Aptamers and Nano Particles. *SCI CHINA SER B* **2007,** *50*, 351-357.
184. Yang, H.; Ji, J.; Liu, Y.; Kong, J.; Liu, B., An Aptamer-Based Biosensor for Sensitive Thrombin Detection. *Electrochem. Commun.* **2009,** *11*, 38-40.
185. Bizzarri, A. R.; Cannistraro, S., Sers Detection of Thrombin by Protein Recognition Using Functionalized Gold Nanoparticles. *Nanomed. Nanotechnol. Biol. Med.* **2007,** *3*, 306-310.
186. Wu, Z.; Liu, Y.; Zhou, X.; Shen, A.; Hu, J., A "Turn-Off" Sers-Based Detection Platform for Ultrasensitive Detection of Thrombin Based on Enzymatic Assays. *Biosens. Bioelectron.* **2013,** *44*, 10-15.

187. Bellido, E. P.; Bobadilla, A. D.; Rangel, N. L.; Zhong, H.; Norton, M.*, et al.*, Current-Voltage-Temperature Characteristics of DNA Origami. *Nanotechnology* **2009,** *20*.
188. Hong, S.; Jauregui, L. A.; Rangel, N. L.; Cao, H.; Day, S.*, et al.*, Impedance Measurements on a DNA Junction. *J. Chem. Phys.* **2008,** *128*, 201103 (1-4)
189. Bobadilla, A. D.; Bellido, E. P.; Rangel, N. L.; Zhong, H.; Norton, M.*, et al.*, DNA Origami Impedance Measurement at Room Temperature. *J. Chem. Phys.* **2009,** *130*.
190. Pagano, B.; Martino, L.; Randazzo, A.; Giancola, C., Stability and Binding Properties of a Modified Thrombin Binding Aptamer. *Biophys. J.* **2008,** *94*, 562-569.
191. Yang, C.; Kim, E.; Pak, Y., Potential of Mean Force Simulation by Pulling a DNA Aptamer in Complex with Thrombin. *Bull. Korean Chem. Soc.* **2012,** *33*, 3597-3600.
192. Trapaidze, A.; Bancaud, A.; Brut, M., Binding Modes of Thrombin Binding Aptamers Investigated by Simulations and Experiments. *Appl. Phys. Lett.* **2015,** *106*, 043702.
193. Yoo, J.; Aksimentiev, A., In Situ Structure and Dynamics of DNA Origami Determined through Molecular Dynamics Simulations. *Proc. Natl. Acad. Sci.* **2013,** *110*, 20099-20104.
194. Kim, D.-N.; Kilchherr, F.; Dietz, H.; Bathe, M., Quantitative Prediction of 3d Solution Shape and Flexibility of Nucleic Acid Nanostructures. *Nucleic Acids Res.* **2012,** *40*, 2862-2868.
195. Plimpton, S., Fast Parallel Algorithms for Short-Range Molecular Dynamics. *J. Comput. Phys.* **1995,** *117*, 1-19.
196. MacKerell, A. D.; Bashford, D.; Bellott, M.; Dunbrack, R. L.; Evanseck, J. D.*, et al.*, All-Atom Empirical Potential for Molecular Modeling and Dynamics Studies of Proteins. *J. Phys. Chem. B* **1998,** *102*, 3586-3616.
197. MacKerell, A. D.; Banavali, N.; Foloppe, N., Development and Current Status of the Charmm Force Field for Nucleic Acids. *Biopolymers* **2000,** *56*, 257-265.
198. Douglas, S. M.; Marblestone, A. H.; Teerapittayanon, S.; Vazquez, A.; Church, G. M.*, et al.*, Rapid Prototyping of 3d DNA-Origami Shapes with Cadnano. *Nucleic Acids Res.* **2009,** *37*, 5001-5006.
199. Yoo, J.; Sobh, A. N.; Li, C.-Y.; Aksimentiev, A., Cadnano to Pdb File Converter. 2014.
200. Pettersen, E. F.; Goddard, T. D.; Huang, C. C.; Couch, G. S.; Greenblatt, D. M.*, et al.*, Ucsf Chimera—a Visualization System for Exploratory Research and Analysis. *J. Comput. Chem.* **2004,** *25*, 1605-1612.
201. Humphrey, W.; Dalke, A.; Schulten, K., Vmd: Visual Molecular Dynamics. *J. Mol. Graph.* **1996,** *14*, 33-38.
202. Berendsen, H. J. C.; Postma, J. P. M.; van Gunsteren, W. F.; DiNola, A.; Haak, J. R., Molecular Dynamics with Coupling to an External Bath. *J. Chem. Phys.* **1984,** *81*, 3684-3690.

203. Nagatoishi, S.; Isono, N.; Tsumoto, K.; Sugimoto, N., Hydration Is Required in DNA G-Quadruplex–Protein Binding. *ChemBioChem* **2011,** *12*, 1822-1826.
204. Nagatoishi, S.; Sugimoto, N., Interaction of Water with the G-Quadruplex Loop Contributes to the Binding Energy of G-Quadruplex to Protein. *Mol. Biosyst.* **2012,** *8*, 2766-2770.
205. Stephenson, T.; Li, Z.; Olsen, B.; Mitlin, D., Lithium Ion Battery Applications of Molybdenum Disulfide (Mos_2) Nanocomposites. *Energy Environ. Sci.* **2014,** *7*, 209-231.
206. Wang, Q. H.; Kalantar-Zadeh, K.; Kis, A.; Coleman, J. N.; Strano, M. S., Electronics and Optoelectronics of Two-Dimensional Transition Metal Dichalcogenides. *Nat. Nanotechnol.* **2012,** *7*, 699-712.
207. Chhowalla, M.; Shin, H. S.; Eda, G.; Li, L.-J.; Loh, K. P.*, et al.*, The Chemistry of Two-Dimensional Layered Transition Metal Dichalcogenide Nanosheets. *Nat. Chem.* **2013,** *5*, 263-275.
208. Radisavljevic B; Radenovic A; Brivio J; Giacometti V; Kis A, Single-Layer Mos_2 Transistors. *Nat. Nano.* **2011,** *6*, 147-150.
209. Wilson, J. A.; Yoffe, A. D., The Transition Metal Dichalcogenides Discussion and Interpretation of the Observed Optical, Electrical and Structural Properties. *Adv. Phys.* **1969,** *18*, 193-335.
210. Lauritsen, J. V.; Kibsgaard, J.; Olesen, G. H.; Moses, P. G.; Hinnemann, B.*, et al.*, Location and Coordination of Promoter Atoms in Co-and Ni-Promoted Mos_2-Based Hydrotreating Catalysts. *J. Catal.* **2007,** *249*, 220-233.
211. Greeley, J.; Jaramillo, T. F.; Bonde, J.; Chorkendorff, I.; Norskov, J. K., Computational High-Throughput Screening of Electrocatalytic Materials for Hydrogen Evolution. *Nat. Mater.* **2006,** *5*, 909-913.
212. Kibsgaard, J.; Chen, Z.; Reinecke, B.; Jaramillo, T., Engineering the Surface Structure of Mos_2 To preferentially Expose Active Edge Sites for Electrocatalysis. *Nat. Mater.* **2012,** *11*, 963-969.
213. Laursen, A. B.; Kegnaes, S.; Dahl, S.; Chorkendorff, I., Molybdenum Sulfides - Efficient and Viable Materials for Electro- and Photoelectrocatalytic Hydrogen Evolution. *Energy Environ. Sci.* **2012,** *5*, 5577-5591.
214. Li, Y.; Wang, H.; Xie, L.; Liang, Y.; Hong, G.*, et al.*, Mos_2 Nanoparticles Grown on Graphene: An Advanced Catalyst for the Hydrogen Evolution Reaction. *J. Am. Chem. Soc.* **2011,** *133*, 7296-7299.
215. Chang, K.; Chen, W., In Situ Synthesis of Mos_2/Graphene Nanosheet Composites with Extraordinarily High Electrochemical Performance for Lithium Ion Batteries. *Chem. Commun.* **2011,** *47*, 4252-4254.
216. Li, H.; Yin, Z.; He, Q.; Li, H.; Huang, X.*, et al.*, Fabrication of Single- and Multilayer Mos_2 Film-Based Field-Effect Transistors for Sensing No at Room Temperature. *Small* **2012,** *8*, 63-67.
217. He, Q.; Zeng, Z.; Yin, Z.; Li, H.; Wu, S.*, et al.*, Fabrication of Flexible Mos_2 Thin-Film Transistor Arrays for Practical Gas-Sensing Applications. *Small* **2012,** *8*, 2994-2999.

218. Zhu, C.; Zeng, Z.; Li, H.; Li, F.; Fan, C., *et al.*, Single-Layer Mos_2-Based Nanoprobes for Homogeneous Detection of Biomolecules. *J. Am. Chem. Soc.* **2013,** *135*, 5998-6001.
219. Shembel, E.; Apostolova, R.; Kirsanova, I.; Tysyachny, V., Electrolytic Molybdenum Sulfides for Thin-Layer Lithium Power Sources. *J Solid State Electrochem* **2008,** *12*, 1151-1157.
220. Bhandavat, R.; David, L.; Singh, G., Synthesis of Surface-Functionalized Ws2 Nanosheets and Performance as Li-Ion Battery Anodes. *The Journal of Physical Chemistry Letters* **2012,** *3*, 1523-1530.
221. Julien, C.; Saikh, S. I.; Nazri, G. A., Electrochemical Studies of Disordered Mos_2 as Cathode Material in Lithium Batteries. *Mater. Sci. Eng., B* **1992,** *15*, 73-77.
222. Paul, J.-F.; Cristol, S.; Payen, E., Computational Studies of (Mixed) Sulfide Hydrotreating Catalysts. *Catal. Today* **2008,** *130*, 139-148.
223. Ma, X.; Schobert, H. H., Molecular Simulation on Hydrodesulfurization of Thiophenic Compounds over Mos_2 Using Zindo. *J. Mol. Catal. A: Chem.* **2000,** *160*, 409-427.
224. Wen, X.-D.; Zeng, T.; Li, Y.-W.; Wang, J.; Jiao, H., Surface Structure and Stability of Mos_x Model Clusters. *J. Phys. Chem. B* **2005,** *109*, 18491-18499.
225. Byskov, L. S.; Nørskov, J. K.; Clausen, B. S.; Topsøe, H., Dft Calculations of Unpromoted and Promoted Mos_2-Based Hydrodesulfurization Catalysts. *J. Catal.* **1999,** *187*, 109-122.
226. Raybaud, P.; Hafner, J.; Kresse, G.; Kasztelan, S.; Toulhoat, H., Structure, Energetics, and Electronic Properties of the Surface of a Promoted Mos_2 Catalyst: An Ab Initio Local Density Functional Study. *J. Catal.* **2000,** *190*, 128-143.
227. Paul, J.-F.; Payen, E., Vacancy Formation on Mos_2 Hydrodesulfurization Catalyst: Dft Study of the Mechanism. *J. Phys. Chem. B* **2003,** *107*, 4057-4064.
228. Raybaud, P.; Hafner, J.; Kresse, G.; Kasztelan, S.; Toulhoat, H., Ab Initio Study of the H_2–H_2S/Mos_2 Gas–Solid Interface: The Nature of the Catalytically Active Sites. *J. Catal.* **2000,** *189*, 129-146.
229. Cristol, S.; Paul, J.; Payen, E.; Bougeard, D.; Clémendot, S., *et al.*, Theoretical Study of the Mos_2 (100) Surface: A Chemical Potential Analysis of Sulfur and Hydrogen Coverage. *J. Phys. Chem. B* **2000,** *104*, 11220-11229.
230. Sun, M.; Nelson, A. E.; Adjaye, J., On the Incorporation of Nickel and Cobalt into Mos_2-Edge Structures. *J. Catal.* **2004,** *226*, 32-40.
231. Schweiger, H.; Raybaud, P.; Toulhoat, H., Promoter Sensitive Shapes of Co(Ni)Mos Nanocatalysts in Sulfo-Reductive Conditions. *J. Catal.* **2002,** *212*, 33-38.
232. Egorova, M.; Prins, R., The Role of Ni and Co Promoters in the Simultaneous Hds of Dibenzothiophene and Hdn of Amines over Mo/Γ-Al_2O_3 Catalysts. *J. Catal.* **2006,** *241*, 162-172.
233. Cristol, S.; Paul, J.-F.; Payen, E.; Bougeard, D.; Hutschka, F., *et al.*, Dbt Derivatives Adsorption over Molybdenum Sulfide Catalysts: A Theoretical Study. *J. Catal.* **2004,** *224*, 138-147.

234. Travert, A.; Nakamura, H.; van Santen, R. A.; Cristol, S.; Paul, J.-F., *et al.*, Hydrogen Activation on Mo-Based Sulfide Catalysts, a Periodic Dft Study. *J. Am. Chem. Soc.* **2002,** *124*, 7084-7095.
235. Sun, M.; Nelson, A. E.; Adjaye, J., Ab Initio Dft Study of Hydrogen Dissociation on Mos_2, Nimos, and Comos: Mechanism, Kinetics, and Vibrational Frequencies. *J. Catal.* **2005,** *233*, 411-421.
236. Sun, M.; Nelson, A. E.; Adjaye, J., Adsorption and Dissociation of H_2 and H_2S on Mos_2 and Nimos Catalysts. *Catal. Today* **2005,** *105*, 36-43.
237. Raybaud, P.; Hafner, J.; Kresse, G.; Toulhoat, H., Adsorption of Thiophene on the Catalytically Active Surface of Mos_2: An Ab Initio Local-Density-Functional Study. *Phys. Rev. Lett.* **1998,** *80*, 1481.
238. Orita, H.; Uchida, K.; Itoh, N., Adsorption of Thiophene on an Mos_2 Cluster Model Catalyst: Ab Initio Density Functional Study. *J. Mol. Catal. A: Chem.* **2003,** *193*, 197-205.
239. Faye, P.; Payen, E.; Bougeard, D., Cluster Approach of Active Sites in an Mos_2 Catalyst. *J Mol Model* **1999,** *5*, 63-71.
240. Yang, H.; Fairbridge, C.; Ring, Z., Adsorption of Dibenzothiophene Derivatives over a Mos_2 Nanoclustera Density Functional Theory Study of Structure−Reactivity Relations. *Energy Fuels* **2003,** *17*, 387-398.
241. Borges, I.; Silva, A. M.; Aguiar, A. P.; Borges, L. E.; Santos, J. C. A., *et al.*, Density Functional Theory Molecular Simulation of Thiophene Adsorption on Mos_2 Including Microwave Effects. *J. Mol. Struct. THEOCHEM* **2007,** *822*, 80-88.
242. Moses, P. G.; Hinnemann, B.; Topsøe, H.; Nørskov, J. K., The Hydrogenation and Direct Desulfurization Reaction Pathway in Thiophene Hydrodesulfurization over Mos_2 Catalysts at Realistic Conditions: A Density Functional Study. *J. Catal.* **2007,** *248*, 188-203.
243. Berit, H.; Poul Georg, M.; Jens, K. N., Recent Density Functional Studies of Hydrodesulfurization Catalysts: Insight into Structure and Mechanism. *J. Phys.: Condens. Matter* **2008,** *20*, 064236.
244. Bataille, F.; Lemberton, J.-L.; Michaud, P.; Pérot, G.; Vrinat, M., *et al.*, Alkyldibenzothiophenes Hydrodesulfurization-Promoter Effect, Reactivity, and Reaction Mechanism. *J. Catal.* **2000,** *191*, 409-422.
245. Plimpton, S.; Crozier, P.; Thompson, A., LAMMPS-Large-Scale Atomic/Molecular Massively Parallel Simulator. *Sandia National Laboratories* **2007,** *18*.
246. Martínez, L.; Andrade, R.; Birgin, E. G.; Martínez, J. M., Packmol: A Package for Building Initial Configurations for Molecular Dynamics Simulations. *J. Comput. Chem.* **2009,** *30*, 2157-2164.
247. Rappé, A. K.; Casewit, C. J.; Colwell, K.; Goddard III, W.; Skiff, W., UFF, a Full Periodic Table Force Field for Molecular Mechanics and Molecular Dynamics Simulations. *J. Am. Chem. Soc.* **1992,** *114*, 10024-10035.
248. Rappe, A.; Colwell, K.; Casewit, C., Application of a Universal Force Field to Metal Complexes. *Inorg. Chem.* **1993,** *32*, 3438-3450.

249. Rappe, A. K.; Goddard III, W. A., Charge Equilibration for Molecular Dynamics Simulations. *J. Phys. Chem.* **1991,** *95*, 3358-3363.
250. Berendsen, H. J.; Postma, J. P. M.; van Gunsteren, W. F.; DiNola, A.; Haak, J., Molecular Dynamics with Coupling to an External Bath. *J. Chem. Phys.* **1984,** *81*, 3684-3690.
251. Giorgino, T., Computing 1-D Atomic Densities in Macromolecular Simulations: The Density Profile Tool for Vmd. *Comput. Phys. Commun.* **2014,** *185*, 317-322.
252. Frisch, M.; Trucks, G.; Schlegel, H.; Scuseria, G.; Robb, M.*, et al.*, Gaussian 09, Revision B. 01. *Gaussian Inc., Wallingford, CT* **2010**.
253. Hohenberg, P.; Kohn, W., Inhomogeneous Electron Gas. *Physical review* **1964,** *136*, B864.
254. Kohn, W.; Sham, L. J., Self-Consistent Equations Including Exchange and Correlation Effects. *Physical Review* **1965,** *140*, A1133.
255. Becke, A. D., Density Functional Thermochemistry. III. The Role of Exact Exchange. *J. Chem. Phys.* **1993,** *98*, 5648-5652.
256. Perdew, J. P.; Burke, K.; Wang, Y., Generalized Gradient Approximation for the Exchange-Correlation Hole of a Many-Electron System. *Phys. Rev. B.* **1996,** *54*, 16533.
257. Perdew, J. P.; Chevary, J.; Vosko, S.; Jackson, K. A.; Pederson, M. R.*, et al.*, Atoms, Molecules, Solids, and Surfaces: Applications of the Generalized Gradient Approximation for Exchange and Correlation. *Phys. Rev. B.* **1992,** *46*, 6671.
258. Perdew, J. P.; Chevary, J.; Vosko, S.; Jackson, K. A.; Pederson, M. R.*, et al.*, Erratum: Atoms, Molecules, Solids, and Surfaces: Applications of the Generalized Gradient Approximation for Exchange and Correlation. *Phys. Rev. B.* **1993,** *48*, 4978.
259. Perdew, J. P.; Ziesche, P.; Eschrig, H., *Electronic Structure of Solids' 91*. Akademie Verlag, Berlin: 1991; Vol. 11.
260. Burke, K.; Perdew, J.; Wang, Y.; Dobson, J.; Vignale, G.*, et al.*, Electronic Density Functional Theory: Recent Progress and New Directions. *Dobson, JF* **1998**, 81-112.
261. Hay, P. J.; Wadt, W. R., Ab Initio Effective Core Potentials for Molecular Calculations. Potentials for the Transition Metal Atoms Sc to Hg. *J. Chem. Phys.* **1985,** *82*, 270-283.
262. Hehre, W. J.; Ditchfield, R.; Pople, J. A., Self—Consistent Molecular Orbital Methods. XII. Further Extensions of Gaussian—Type Basis Sets for Use in Molecular Orbital Studies of Organic Molecules. *J. Chem. Phys.* **1972,** *56*, 2257-2261.
263. Francl, M. M.; Pietro, W. J.; Hehre, W. J.; Binkley, J. S.; Gordon, M. S.*, et al.*, Self-Consistent Molecular Orbital Methods. XXIII. A Polarization-Type Basis Set for Second-Row Elements. *J. Chem. Phys.* **1982,** *77*, 3654-3665.
264. Bobadilla, A. D.; Ocola, L. E.; Sumant, A. V.; Kaminski, M.; Kumar, N.*, et al.*, Europium Effect on the Electron Transport in Graphene Ribbons. *J. Phys. Chem. C* **2015,** *119*, 22486-22495.